Mathematical Models of Magnetic Nanoparticles in Hyperthermia and Targeted Delivery

Mangolika Bhattacharya

MSc 2020

Mathematical Models of Magnetic Nanoparticles in Hyperthermia and Targeted Delivery

Mangolika Bhattacharya

School of Engineering
Waterford Institute of Technology

Supervisors: Dr PJ Cregg
Dr Kieran Murphy

Submitted in fulfilment of the requirements
for the degree of MSc in Engineering
at Waterford Institute of Technology.

July 2020

Declaration of Authorship

I, Mangolika Bhattacharya, declare that this thesis titled, "Mathematical Models of Magnetic Nanoparticles in Hyperthermia and Targeted Delivery" and the work presented in it are my own. I confirm that:

- This work was done wholly or mainly while in candidature for a research degree at this Institute.
- Where any part of this thesis has previously been submitted for a degree or any other qualification at this Institute or any other institution, this has been clearly stated.
- Where I have consulted the published work of others, this is always clearly attributed.
- Where I have quoted from the work of others, the source is always given. With the exception of such quotations, this thesis is entirely my own work.
- I have acknowledged all main sources of help.
- Where the thesis is based on work done by myself jointly with others, I have made clear exactly what was done by others and what I have contributed myself

Signed: _____

Date: _____

Acknowledgements

I would like to express my profound gratitude to my supervisors, Dr PJ Cregg and Dr Kieran Murphy, for their patient & perennial guidance, enthusiastic encouragement and constructive critiques for this research work. Without their support, this work would not have been possible. It has truly been an incredible learning experience.

I would like to thank the Waterford Institute of Technology & the School of Engineering for the sponsorship of this work under WIT PhD scholarship award and WIT extension grant. I would like to thank the department of Engineering Technolgy and all the lecturers of electronic engineering for their support throughout my stay in WIT.

I would like to thank Dr Pádraig Kirwan and the School of Science & Computing for facilitating lecturing hours, which have helped me to sustain and complete this work.

To my family

Abstract

Magnetic nanoparticles (MNPs), mainly iron oxide particles, have the advantage of being controllable by magnetic fields. MNPs show promise in biomedical applications, typically as carriers for biological or therapeutic entities or for their hyperthermic properties. Mathematical modelling assists in the design of MNP applications. However, the role of interparticle interactions is frequently ignored due to computational complexity, despite the general acceptance of the importance of interactions. Magnetic hyperthermia and magnetic drug delivery are two important clinical applications of MNPs where magnetic dipole interaction can be expected to have a significant role in the behaviour and thus be important in any potential medical applications. Good design of magnetic hyperthermia treatment approaches a thorough understanding of the complexities of the heating mechanisms. There are typically two mechanisms which lead to heating: Debye and Néel relaxation. Most models of hyperthermia consider only Debye relaxation and typically interparticle interaction is ignored. Targeted drug delivery aims to reduce the undesired side effects of drug usage by directing or capturing the active agents near a desired site within the body. This is particularly beneficial in, for instance, cancer chemotherapy, where the side effects of general drug administration can be severe. Although a number of mathematical models exist in literature, certain differences in the theoretical and experimental results have been noted. This thesis presents mathematical models of magnetic hyperthermia and magnetic delivery along with detailed analysis of three other mathematical models of magnetic interaction available in the literature.

In this thesis, chapter 1 overviews some general information concerning the role of magnetic nanoparticles in biomedicine and the motivation for this work. Chapter 2 presents a mathematical model of hyperthermia which includes interparticle interactions, and offers empirical approximations to estimate the optimum heating for a chain of MNPs. Chapters 3–5 present replications and in some cases corrections of the models published by various authors. Chapter 6 presents a model investigating the aggregation of MNPs in parabolic flow. Here MNPs are considered whose initial positions are always above or below each other along the vertical axis of the vessel. A critical distance is then found between the MNPs within the vessel. If the MNPs begin their motion within this critical distance, then over time aggregation occurs. This critical distance is found to depend upon the initial position along the diameter of the vessel and also the fluid velocity. Analytic expressions for the upper and lower bounds are obtained and validated with the numerical results. Also, an empirical approximation of the critical distance is given, which gives close agreement with the numerical results.

Contents

List of Figures

List of Tables

List of Symbols

Magnetic field properties

- $\mathbf{B}$, magnetic field[1] ..... T
- $\mathbf{H}$, magnetic field strength ..... $\mathrm{A\,m^{-1}}$
- ω, angular frequency of the magnetic field ..... $\mathrm{rad\,s^{-1}}$
- f, frequency of the magnetic field ..... Hz
- $\frac{\partial B_z}{\partial x}$, x-component of the magnetic gradient when $\mathbf{B}$ is along the z-axis ..... $\mathrm{T\,m^{-1}}$
- μ_0, permeability of free space ..... $\mathrm{H\,m^{-1}}$

Magnetic nanoparticle particle (MNP) properties

- M_s, saturation magnetisation ..... $\mathrm{A\,m^{-1}}$
- $\hat{\mathbf{m}}$, unit vector as per the initial alignment of the MNPs ..... dimensionless
- $\mathbf{M} = M_s\hat{\mathbf{m}}$, volume magnetisation vector ..... $\mathrm{A\,m^{-1}}$
- V, volume of an MNP ..... $\mathrm{m^3}$
- $\mathbf{m} = \mathbf{M}V$, magnetic moment of an MNP ..... $\mathrm{A\,m^2}$
- $\mathbf{d}^{(i,j)}$, vector joining the MNP centres, from i^{th} to j^{th} ..... m
- $d^{(i,j)}$, distance between the centres of of i^{th} and j^{th} MNP ..... m
- $\hat{\mathbf{d}}^{(i,j)}$, unit vector along line of MNP centres from i^{th} to j^{th} ..... dimensionless
- R, initial average radius of the MNPs ..... m
- n, number of MNPs ..... dimensionless
- $\mathbf{F}_m$, magnetic force ..... N
- $\mathbf{F}_{\mathrm{int}}$, dipolar interaction force ..... N
- $\mathbf{F}_d$, drag force ..... N
- t, total time of the simulation ..... s
- δt, time stepping ..... s

[1] It is the convention within electronic & electrical engineering to use $\mathbf{H}$ as magnetic field strength, and $\mathbf{B}$ as magnetic flux density or induction whereas within physics it is common to consider only $\mathbf{B}$ and term it the magnetic field, or the magnetic field vector.

- d_R, relative distance in terms of R ..... dimensionless
- τ_B, Brownian relaxation time ..... s
- k_B, Boltzmann constant ..... $\mathrm{J\,K^{-1}}$
- T, temperature ..... °C
- K_a, anisotropy constant ..... $\mathrm{J\,m^{-3}}$
- f_0, frequency pre-factor ..... $\mathrm{s^{-1}}$

Vessel properties

- R_v, radius of the cylindrical vessel ..... m

Fluid properties

- $\mathbf{v}_f$, fluid velocity ..... $\mathrm{m\,s^{-1}}$
- η, viscosity[2] ..... $\mathrm{kg\,m^{-1}\,s^{-1}}$
- $\overline{v}_f$, average fluid velocity ..... $\mathrm{m\,s^{-1}}$

[2]The symbol η is also used for Gilbert's dissipation constant in chapter 2.

Chapter 1

Introduction to Magnetism

1.1 Magnetic nanoparticles and their role in biomedicine

An increase in interest in nanotechnology has led to growth in nanoparticle research. Nanoparticles in particular offer many possibilities as diagnostic and therapeutic agents. They have controllable sizes ranging from a few nanometres up to hundreds of nanometres, which places them at dimensions that are smaller than or comparable to biological entities such as a cell ($10 - 100$ μm), a virus ($20 - 450$ nm), a protein ($5 - 50$ nm) or a gene (2 nm wide and $10 - 100$ nm long). Magnetic nanoparticles can be controlled by a magnetic field and thus can be heated, leading to their use as hyperthermia agents, or can be used to deliver active agents, such as drugs or cells, to a targeted location [1].

1.1.1 Hyperthermia

Magnetic Hyperthermia is the heating of magnetic nanoparticles in an alternating magnetic field. This heating can directly kill cancer cells. Thus after locating the particles in a tumour the heating can act on the tumour. Furthermore in combination with radiotherapy and/or chemotherapy lower levels of heating can be effective. An inadequate understanding of the heating has been conceded by researchers [2, 3]. As better control of the heating requires a better understanding of the heating, progress can be aided by the development of better mathematical models of hyperthermia. Reports suggest that magnetic interactions, known to occur when the particles are closely spaced, can both increase or decrease the heating [4–8]. Figure 1.1 depicts the strategies used in clinical applications, such as the particle size, shape, surface structure, and composition, in order to improve antitumor therapeutic efficacy of MNPs in magnetic hyperthermia therapy as given in Liu *et al.* [9].

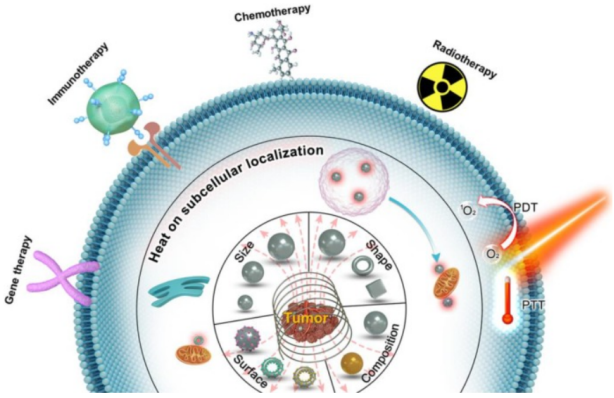

Figure 1.1: Strategies (particle size, shape, surface structure, and composition) used in clinical applications to improve efficacy of MNPs in Magnetic hyperthermia therapy (source [9]).

1.1.2 Cell imaging and delivery

Cell imaging primarily uses light and fluorescence microscopy; however, magnetic labelling of cells, *via* cell uptake of MNPs and subsequent detection *via* MRI, can also be used to image, identify and track cells [10]. Regenerative medicine replaces old and diseased cells with healthy cells, and includes applications in cell delivery and bone marrow transplantation. Magnetic cell delivery (MCD) is an emerging technique in regenerative medicine, where healthy living cells are carried by MNPs to a specific site in the body *via* magnetic fields [11–15]. These fields can be purely external or can be assisted by ferromagnetic implants such as stents [16]. Sanz-Ortega *et al.* [17] showed that the MNPs are used to magnetically guide T cells to a region of interest, *via* both in vitro and in vivo manipulation as illustrated in Figure 1.2. Sanz-Ortega *et al.* showed promising results to favour cell retention that could be implemented to improve cell-based therapy.

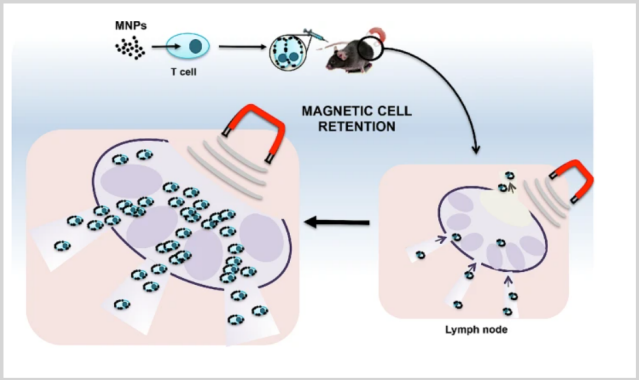

Figure 1.2: Magnetic cell retention in cell-based therapy (source [17]).

1.1.3 Magnetic drug targeting

Targeted drug delivery aims to reduce the undesired side effects of drug usage by directing or capturing the active agents of the drug near a desired site within the body. This is particularly beneficial in, for instance, cancer chemotherapy, where the side effects of the drug administered can be particularly detrimental. The use of MNPs as the carriers of active agents is known as magnetic drug targeting (MDT). In designing such a targeting system, many factors need to be considered such as the size and nature of the carriers and the fields required. Moreover, the range of relevance of these systems in different blood velocities, from capillaries to high velocity arteries, needs to be considered. Dipolar interactions in MNPs cause aggregation which can cause blood clots, leading to life threatening conditions. Mathematical modelling can play a role in the design of such systems by developing our understanding of aggregation. Figure 1.3 depicts MNPs used in clinical applications, visible under MRI scan as given in [18]. These MR-active MNPs enable clear observation of various blood vessels. Thus they can be used for imaging the vasculature, liver and other organs, as well as molecular imaging, cell delivery & tracking and theranostics [18].

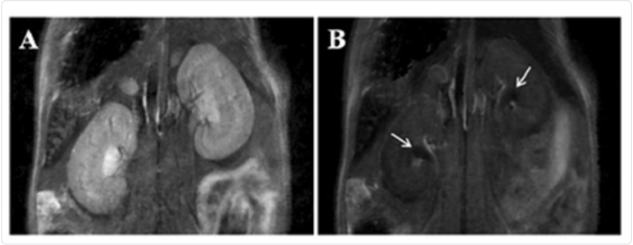

Figure 1.3: Kidneys before and after injection of MNPs where accumulation of MNPs can be observed in the renal pelvis (white arrows) (source [18]).

1.1.3.1 Magnetic microrobots

Magnetic particles are being used to develop microrobots (sized between 10 and 1000 microns) for industrial applications or biomedicine. A magnetic microrobot is a colloidal suspension of superparamagnetic iron oxide (SPIO) particles [19]. Microrobots offer a number of prospective applications in performing precise tasks inside the human body, such as providing a mobile viewing platform enhancing a surgeon's view [20]. Figure 1.4 depicts magnetic microrobots therapy proposed in cancer treatment as given in [8].

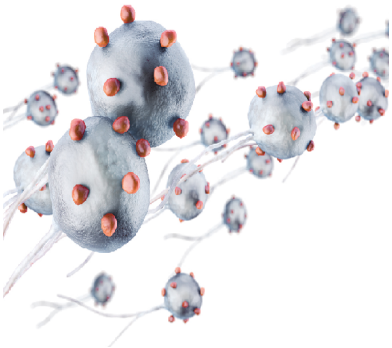

Figure 1.4: Magnetic microrobots (source [8]).

1.2 Role of mathematical modelling in clinical applications

In experiments, the typical path to study the behaviour of MNPs is through *in vitro* and later *in vivo* experiments. Computer simulations can play a key role in the design and interpretation of these experiments. Any description of the behaviour of MNPs in the body must account for fluid dynamics of blood flow as well as the magnetic effects on MNPs due to any external magnetic field. Furthermore MNP interactions are also often critical in assessing the expected performance of MNP interventions. These interactions can lead to particle aggregation, significantly altering the behaviour. A number of authors have cited the importance of studying interparticle interactions [3–6, 21]. Specifically, Wu *et al.* [7] use hyperthermia with antibiotics to treat infections and note that use of MNPs beyond a certain size increases aggregation probabilities, thereby altering the behaviour. Gutiérrez *et. al.* [22] have mentioned similar observation and specifies the importance of agglomeration/aggregation on the alteration of the properties of MNPs. Figure 1.5 shows the difference between different MNPs in colloidal suspension. It is mentioned in [22], that the MNPs aggregation process in colloidal solution is irreversible and needs to be included while studying the properties of the MNPs.

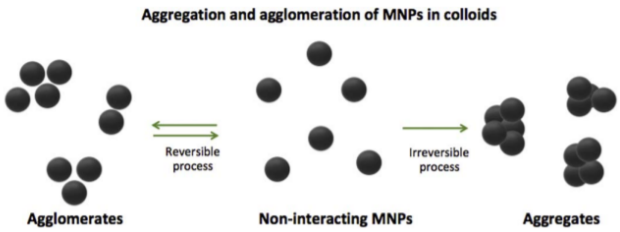

Figure 1.5: Schematic representation of the formation of the aggregation and agglomeration processes of MNPs in colloidal suspensions (source [22]).

Riegler *et al.* [11] have produced results in MCD which differ from their own theoretical predictions. Riegler *et al.* specifically mention that the disagreement between the theoretical and experimental results is due to the neglect of interparticle interactions in their model. This disagreement with their existing model persists and has been addressed in this thesis. The mathematical models by Sharma *et al.* [23] and Mellal *et al.* [19] have been replicated in subsequent chapters. In chapter 2, a mathematical model of hyperthermia is presented, examining the effects of interparticle interactions and propose empirical approximations to estimate the optimum heating in a chain arrangement of MNPs. In chapter 6, a mathematical model of aggregation of MNPs is presented, including dipolar interactions for a range of fluid velocities.

1.3 Primary quantities in magnetism, **H**, **B** *and* **M**

A significant aspect of this thesis involves computing and predicting the behaviour of magnetic nanoparticles in a magnetic field. To understand these calculations, it is useful to discuss some basic magnetic quantities.

The magnetic field strength created by an electric current can be calculated from the Biot-Savart law or from Ampère's law [24, 25]. In the SI unit system the strength of magnetic field, **H** is measured in amperes per metre $\mathrm{A\,m^{-1}}$ which indicates the relation of this quantity to the electric current. The alternate names of **H** are magnetic field intensity and magnetising field.

On the other hand, magnetic flux density or magnetic induction, **B**, is the response of the medium to the magnetic field strength. It can be understood as the density of magnetic lines of force, or magnetic flux lines, passing through a particular area. The movement of a compass needle (a magnetic dipole) is clearly due to the applied torque on the compass needle. The strength of this torque is in turn determined by the strength of the magnetic induction, **B**. Thus it is noted that **B**, not **H**, plays the role of the physical observable in magnetism, in the same way that the electric field strength, does in electrostatics. In the SI unit system **B** is measured in $\mathrm{Wb\,m^{-2}}$ and is defined as the tesla, T.
The volume magnetisation, **M**, is defined as the sum of the magnetic dipole moment per unit volume of a material *via*,

$$\mathbf{M} = \frac{\mathbf{m}}{V} \tag{1.1}$$

where **m** is the magnetic moment and V is the volume. The quantity **M** is measured in ampere per metre ($\mathrm{A\,m^{-1}}$). The interrelation between **B**, **H** and **M** is given by

$$\mathbf{B} = \mu_0(\mathbf{H} + \mathbf{M}) \tag{1.2}$$

where μ_0 is the permeability of vacuum.
In absence of any material properties *i.e.* in the vacuum, $\mathbf{M} = 0$ and $\mathbf{B} = \mu_0\mathbf{H}$. The units of **H** and **M** are $\mathrm{A\,m^{-1}}$ whilst the unit of **B** is T and μ_0 is $\mathrm{H\,m^{-1}}$.
However they can still be related in terms of the permeability of the medium, μ, through,

$$\mathbf{B} = \mu\mathbf{H} \tag{1.3}$$

where μ is in general not a constant and furthermore can be multivalued, as is the case with hysteresis [26].

1.3.1 Magnetic permeability, μ

Magnetic permeability, μ [1] is the measure of the ability of any material to support a magnetic field. The permeability of the vacuum is generally considered to be $\mu_0 = 4\pi \times 10^{-7}\ \mathrm{H\,m^{-1}}$. However, since 20^{th} May 2019, a revision of the SI system has been effected, which states that the μ_0 is no longer a defined constant but rather a measured constant, to be determined experimentally [28]. In general, permeability is not a constant, as it varies within and around the material and with the frequency of the applied magnetic field strength, humidity, temperature, and other parameters.

A related concept, the dimensionless relative permeability, denoted by μ_r, is also used in the SI unit system, defined as

$$\mu_r = \frac{\mu}{\mu_0} \tag{1.4}$$

Magnetic susceptibility, denoted by χ, is closely related to the relative permeability through,

$$\chi = \mu_r - 1 \tag{1.5}$$

1.3.2 Magnetic susceptibility, χ

Magnetic susceptibility is a dimensionless proportionality constant that refers to the extent of magnetisation of a material in response to an applied magnetic field. It is related to **M** and **H** as,

$$\mathbf{M} = \chi\mathbf{H} \tag{1.6}$$

Diamagnetic materials have small and negative susceptibilities because **M**, is in the opposing direction of **H**. Paramagnetic materials have positive susceptibilities as **M** is along the same direction as **H**.

1.3.3 Magnetic gradient

The variation of magnetic field, **B**, with respect to position, $\nabla\mathbf{B}$, is the magnetic gradient.

1.3.4 Magnetic domains and single domain particles

Ferromagnets are composed of domains. Each domain's magnetisation reaches saturation but the direction of magnetisation differs from domain to domain. In an unmagnetised sample, all of these

[1] It is to be noted that the symbol $\boldsymbol{\mu}$ is used to symbolise magnetic moment in chapter 2. In rest of the chapters it is termed as **m**. This is done to comply with the conventions of Châtel *et al.* [27].

domains produce a net total magnetisation vector which is close to zero. In this model, the applied magnetic field can either alter the domain direction or through domain wall motion can increase the size of the domains in the direction of applied field. Both of these tend to increase the magnetisation. The magnetic behaviour of ferromagnets can be broadly divided on the basis of particle size into two types as:

1. multi domain
2. single domain

A multi domain particle contains many domains. The reason is that it reduces the magnetostatic energy associated with the surface charges. However, the domains must be separated by domain walls, that is small regions in which the moments have different directions. To be maintained, these walls also require energy, determined by the exchange and magnetocrystalline energies [29]. Thus, for given sample size, a number of domains is reached. If the size of the sample is reduced, a critical point is reached beyond which it can no longer provide a wall. It then contains a single domain that is uniformly magnetised. The critical size for particles varies depending on the saturation magnetisation and the shape of particle (for magnetite, the critical size is about 80 nm) [26]. The magnetisation of a single domain particle can only be changed by rotating the magnetisation, which can be an energetically difficult process [29, 30]. On the other hand, changing the magnetisation of a multi domain particle can be done by translating the domain wall, which requires a lower field.

1.3.4.1 Superparamagnetism

The magnetic relaxation time is defined as the measure of the time time taken by the magnetisation vector to align itself with the magnetic field. The magnetic relaxation of the MNPs is a convolution of two different processes, namely Brownian and Néel [31]. The Brownian relaxation, τ_B, is given as

$$\tau_B = \frac{3V\eta}{k_B T} \tag{1.7}$$

where V is the volume, η is the viscosity of the fluid. The term k_B and T denote the Boltzmann constant and temperature. In sufficiently small single domain magnetic nanoparticles, the magnetisation can flip direction under the influence of thermal energy. The typical time between two flips is called the Néel relaxation time, τ_N, given as

$$\tau_N = f_0 \exp\left(\frac{K_a V}{k_B T}\right) \tag{1.8}$$

where f_0 is the frequency pre-factor (typically 10^9 s^{-1}) and K_a is the anisotropy constant. Rosensweig [32] suggested that the Néel and Brownian relaxations occur in parallel, with an effective relaxation angular frequency, which is an inverse of this effective relaxation time, τ_{eff}, given by

$$\frac{1}{\tau_{eff}} = \frac{1}{\tau_B} + \frac{1}{\tau_N} \tag{1.9}$$

In the absence of an external magnetic field, when the time used to measure the magnetisation of magnetic nanoparticles is much longer than the Néel relaxation time, the average magnetisation appears zero and the nanoparticles are said to be in the super-paramagnetic state. In this state, an external magnetic field can magnetise the nanoparticles, similar to paramagnets but with higher value of

magnetisation because superparamagnetic particles have higher susceptibility. Equally an ensemble of single domain particles in a ferrofluid can be considered superparamagnetic, even if the Néel relaxation time is larger than the measurement time, provided the time of the Brownian relaxation in the fluid is less than that of measurement.

1.3.5 Magnetic Anisotropy

The term 'anisotropy' is used to describe situations where properties are dependent on direction. A magnetically anisotropic material's moment tends to align with an easy axis which refers to the energetically favourable direction of the moment in the material. Magnetic anisotropy affects the shape of hysteresis loops and changes the values of coercivity and remanence. Hence, magnetic anisotropy is an important practical property in designing a magnetic material. There are different types of anisotropy depending on the crystal structure, shape of grains and applied or residual stresses. The likely effects of anisotropy are mentioned in chapter 2, magnetic hyperthermia, but in the rest of the chapters, the magnetic properties are considered isotropic.

1.3.6 Magnetic Resonance Imaging, MRI

Magnetic resonance imaging (MRI) is a medical imaging technique used to view the anatomy and the physiological processes of the body. MRI scanners use strong magnetic fields and magnetic field gradients to generate images of the organs in the body. Hydrogen atoms exist in abundance within humans and other biological organisms, especially inside water and fats. Thus, most MRI scans locate water and fats in the body. Radio wave pulses stimulate the energy transition of nuclear spin, and magnetic field gradients adjust the resonant frequency in space to create spatially measurable changes in signal. By varying the parameters of the pulse sequence, different contrasts can be produced between the tissues in accordance with the relaxation properties of the hydrogen atoms [33].

Chapter 2

Magnetic Hyperthermia

Magnetic Hyperthermia is the heating of magnetic nanoparticles using an alternating magnetic field. In this chapter, existing models of magnetic hyperthermia are reviewed and a mathematical model is presented, incorporating the interparticle interactions. Along with numerical results, analytical and empirical approximations for regenerating the numerical results are presented, to obtain optimum heating for MNPs in a chain arrangement.

2.1 Additional list of symbols

- $\boldsymbol{\mu}$, magnetic moment[1] ..... $\mathrm{A\,m^2}$
- $\mathbf{m}^{(i)}$, volume magnetisation vector of the i^{th} MNP ..... $\mathrm{A\,m^{-1}}$
- $\mathbf{H}_{\mathrm{int}}^{(i)}$, magnetic interaction field experienced by the i^{th} MNP ..... $\mathrm{A\,m^{-1}}$
- H, magnitude of $\mathbf{H}$ ..... $\mathrm{A\,m^{-1}}$
- θ, polar angle ..... radians
- ϕ, azimuth angle ..... radians
- γ_0, gyromagnetic ratio ..... $\mathrm{A\,m^2\,J^{-1}\,s^{-1}}$
- η, Gilbert's dissipation constant[2] ..... s
- $\alpha = \mu_0\gamma_0\eta M_s$, the damping factor ..... dimensionless
- $\mathbf{M} = (\sin\theta\cos\phi, \sin\theta\sin\phi, \cos\theta)$,
  unit vector indicating the direction of the volume magnetisation vector ... dimensionless
- M_x, x component of $\mathbf{M}$ ..... dimensionless
- M_y, y component of $\mathbf{M}$ ..... dimensionless
- M_z, z component of $\mathbf{M}$ ..... dimensionless
- ζ, angle between the external field and the line joining the centres of the MNPs ..... radians
- $\dot{\mathbf{M}}$, velocity of the unit volume magnetisation vector $\mathbf{M}$ ..... $\mathrm{A\,m^{-1}\,s^{-1}}$
- c_t, coating thickness ratio ..... dimensionless
- E, average energy per cycle per unit volume ..... $\mathrm{J\,m^{-3}}$

[1] To comply with the conventions of Châtel *et al.* [27], the magnetic moment is symbolised as $\boldsymbol{\mu}$ in this chapter. In rest of the chapters it is termed as $\mathbf{m}$.

[2] The symbol η is used for viscosity from chapter 3 onwards.

- d_0, distance between the MNPs relative to R, where
  the value of E is same as one non-interacting MNP ..... m
- $d_{\min}$ distance between the MNPs relative to R, where the value of E is minimum ..... m

Table 2.1: List of parameters values for chapter 2.

Parmeter	Description	Value
M_s	saturation magnetisation	0.5×10^6 A m^{-1}
H	magnetic field strength	10^4 A m^{-1}
γ_0	gyromagnetic ratio when $H = 1$	1.76×10^{11} A m^2 J^{-1} s^{-1}
α	damping constant	1
ϕ	initial value of azimuth angle	0 radians
θ	initial value of polar angle	$\pi/2$ radians

2.2 Introduction

Magnetic nanoparticles (MNPs) offer many possibilities as diagnostic and therapeutic agents. One important therapeutic application of MNPs is magnetic hyperthermia treatment (MHT). In MHT, MNPs are first focussed on a tumour; then, on application of radio frequency magnetic fields the MNPs can be heated. The heating of cells above 47°C generally leads to cell death. Heating within the range 41-46°C damages cells and significantly assists in cancer cell death when used in combination with radiotherapy and/or chemotherapy [34, 35].

In 2011, Carrey *et al.* [3] presented a review of magnetic hyperthermia models where attention was drawn to the neglect of interparticle interactions in the models. Since then many authors on MHT have drawn attention to the likely role of dipole-dipole interactions between the MNPs [3–5, 36–40]. Theoretical and experimental studies appear to indicate that the effects lead to reduced heating in the majority of physical arrangements. Consequently, any random arrangement is likely to exhibit reduced heating [4, 5, 21]. However, any cases in which the dipole-dipole interactions might increase heating are of particular interest as these might allow the administering of less MNPs with potentially the same heating. Haase and Nowak have undertaken a comprehensive computational study for a random distribution of MNPs and have found reduced heating except for the case of elongated MNPs [21]. Their results showed decreasing hysteresis areas for (strongly) increased particle concentrations. Within a fixed sample volume, however, the increased concentration also led to more particles that produced heat. For small concentrations an almost linear increase of the volume specific absorbtion rate (VSAR) was seen since dipole-dipole interactions were weak. At higher concentrations a maximum heating was found with a further increase of particle density, which led to a reduced VSAR. This suggested that an upper limit existed for the number of particles that should be injected into a fixed tumor volume, defined by the dipole-dipole interactions.

Ruta *et al.* [6] have presented a Monte Carlo model which showed both enhancement and suppression of the expected heating resulting from dipolar interactions. They mentioned the dependance of maximum heating and the optimal particle size as a function of the packing fraction. With enhanced heating in mind a chain of MNPs is considered aligned at right angles to the applied alternating magnetic

heating field. Beginning with two particle interactions it is showed that heating per particle has the potential to be increased by up to 18%. It is observed that longer chains show additional but diminishing enhancement. It is noted that the dipole-dipole interactions scale with $\mathbf{d}^3$, where $\mathbf{d}$ is vector along the line joining the centres of the MNPs and that as the volume scales with particle radius, R, cubed (R^3), the overall behaviour described by the model effectively scales with particle radius. This applies provided the particle is superparamagnetic and anisotropy effects can be ignored. The former condition is satisfied for MNPs below a critical size. The likely effects of anisotropy are mentioned in the conclusion but have not been addressed in this work.

2.3 Mathematical models of MHT

In general, there are two mechanisms which can lead to heating: Brownian (Debye) and Néel relaxation. The former refers to the rotation of MNPs. The latter is the internal rotation of the magnetic moment within the MNPs. For MNPs below a critical size the MNPs are superparamagnetic and the magnetic moment can move relative to the particle in response to an external field. The size differs for different materials but is of the order of tens of nanometres [26]. Here situations are considered where the particle rotation is blocked, leaving only the Néel relaxation, which might occur for MNPs fixed in a tumour. This occurrence has been reported in [27, 41, 42]. Experiments have been carried out in [43] to restrict the heat dissipation through Brownian relaxation to determine the relative contribution of Néel relaxation to dissipate heat and its potential for *in vivo* application, in magnetite nanoparticles. Hergt *et al.* [44] mention that generally, the faster of both relaxation mechanisms governs the absorption of the particle system. As outlined by Hergt *et al.* [44] due to the very different size dependence given by equations (2.1) and (2.2) for the two relaxation regimes, there is a separation of the spectral regions of Brown (τ_B)and Néel (τ_N) relaxation given by

$$\tau_B = \frac{3V\eta}{k_B T} \tag{2.1}$$

$$\tau_N = f_0 \exp\left(\frac{K_a V}{k_B T}\right) \tag{2.2}$$

where V is the volume, η is the viscosity of the fluid. The terms k_B and T denote the Boltzmann constant and temperature. The term, f_0 is the frequency pre-factor (typically 10^9 s^{-1}) and K_a is the anisotropy constant. The boundary between both regions is defined by $\tau_N = \tau_B$. In general, Néel relaxation occurs at higher frequency combined with smaller particle size and Brownian relaxation occurs at lower frequencies with larger particle size. The boundary frequency, f_c, and the corresponding particle diameter, d_c, varies for different ferrofluid systems as listed in Hergt *et al.* [44]. Thus, it can be said that for certain frequencies regimes the MNPs are essentially fixed and Debye heating effect is effectively blocked. It is noted that the Debye heating mechanism is restricted in the two cases when the MNPs are physically fixed in a tumour and when the MNPs are being excited within certain frequency regimes.

The Landau-Lifshitz-Gilbert (LLG) equation is a phenomenological equation, which describes the specific behaviour of the magnetisation of an individual single domain ferromagnetic particle [21]. The approach taken here is to model the heating through the LLG equation and calculate heating through the work done by the Gilbert 'damping force' of the magnetic moment acting over a distance. The

approach is shown to be equivalent to that of Châtel *et al.* [27]. This model is extended to treat two or more MNPs interacting *via* dipole-dipole interactions in a linear chain structure. The approach can also be seen as a reduced case of the model of Haase & Nowak, where those authors also treated uniaxial anisotropy and particle size distribution, and modelled the stochastic nature of the problem through Langevin dynamics [21, 24, 25, 45]. Here, the results are presented in terms of energy per cycle per unit volume, E, which can be related to the specific absorption rate (SAR) by

$$SAR = Ef$$

where f is the frequency of the applied field.

2.4 The Landau-Lifshitz-Gilbert (LLG) equation

The LLG equation [46] is a phenomenological equation for the average damped precessional motion of the magnetic moment, $\boldsymbol{\mu}$ (expressed as the normalised volume magnetisation vector, $\mathbf{m}$, where $\boldsymbol{\mu} = V\mathbf{m}$ and $\mathbf{m} = \mathbf{M}M_s$), of an MNP in a magnetic field $\mathbf{H}$ [21, 24, 27, 47–49].

$$\dot{\mathbf{M}} = \left(\frac{\mu_0\gamma_0}{1+\alpha^2}\right)[\mathbf{M}\times\mathbf{H} + \alpha(\mathbf{M}\times\mathbf{H})\times\mathbf{M}], \tag{2.3}$$

where V is the volume of an MNP, and $\mathbf{M} = (\sin\theta\cos\phi, \sin\theta\sin\phi, \cos\theta)$ is the unit vector indicating the direction of $\mathbf{m}$, M_s is (volume) saturation magnetisation, μ_0 is the magnetic permeability of free space and α is the dimensionless damping parameter, defined by $\alpha = \mu_0\eta\gamma_0 M_s$, where η is the Gilbert dissipation constant and γ_0 is the gyromagnetic ratio. In this work, the MNPs are considered to be spherical.
The alternating, cosinusoidal field, $\mathbf{H}$, is assumed to be applied in the z direction, so that

$$\mathbf{H} = H(0, 0, \cos\omega t) \tag{2.4}$$

where ω is the angular frequency of the field and H is the magnitude of the field.

2.4.1 Numerical techniques to solve the LLG equation

Equation (2.3) is a nonlinear equation and needs to be solved using numerical techniques. The following properties, however, need to be maintained while solving the LLG equation using any numerical technique [50].

- The magnitude of the magnetisation vector, $\mathbf{m}$, must be kept constant at all discrete time points. It is a fundamental constraint on the LLG time evolution that must be maintained in the time discretised version of LLG equation.
- In the limit $\alpha \to 0$, the numerical integration must always preserve energy.
- For a DC external field, the LLG evolution has a Lyapunov structure which means the total energy of the system is a decreasing function of time along the trajectories of LLG equation [50].

2.4.1.1 *Problems in the low frequency region*

The medical applications of magnetic hyperthermia are carried out at frequencies around 100 kHz. However, because of the computational difficulties in the lower range of frequencies, numerical modelling of LLG equations has mostly been carried out at a higher frequency from 10 MHz to 100 MHz. This problem has been noted by Hasse & Nowak [21]. Thus to model the experimental results, most of which have been carried out between 10 kHz and 100 kHz, the various numerical techniques are investigated which have been used to solve the LLG equation at both high and low frequencies.

2.4.1.2 *Semianalytical techniques*

When the effective magnetic field, **H**, is constant in time, the LLG equation generates a simple analytical expression in spherical coordinates [27, 51] or by the application of projection methods [50]. This analytical solution can then be used to improve an existing numerical scheme. The resulting semianalytical scheme can then be used to fulfil the required conditions to solve the LLG equation. In this section the different analytical expressions are examined that are presented in the literature and show that some forms of analytical expression are unable to conserve the properties, as given in section 2.4.1, which need to be maintained while solving the LLG equation.

For $\omega = 0$, the analytical solution of the LLG equation as given in Châtel *et al.* is

$$M_x(t+\delta t) = \frac{\tanh(\alpha_N \delta t) + M_x(t)}{1 + M_x(t)\tanh(\alpha_N \delta t)} \tag{2.5}$$

$$M_y(t+\delta t) = \sqrt{1 - M_x^2(t+\delta t)}\,\sin\left(\sin\left(\omega_L t + \delta_0\right) + \delta_0\right) \tag{2.6}$$

$$M_z(t+\delta t) = \sqrt{1 - M_x^2(t+\delta t)}\,\cos\left(\sin\left(\omega_L t + \delta_0\right) + \delta_0\right) \tag{2.7}$$

where

- M_x, M_y and M_z are the components of **M** along the x, y and z axes, respectively,
- $\omega_L = \mu_0\gamma_0 H/(1+\alpha^2)$,
- $\alpha_N = \alpha\omega_L$,
- $\delta_0 = \frac{M_y(t)}{M_z(t)}$ are determined by the initial conditions,
- $M_x(t) = M_x(0)$, where $M_x(0)$ is the initial value of the x component of **M**.

In Wiele *et al.*[51], a different expression was obtained for the analytical solution,

$$M_x(t+\delta t) = \frac{\exp(q\alpha\delta t)(1+M_x(t)) - \exp(-q\alpha\delta t)(1-M_x(t))}{\exp(q\alpha\delta t)(1+M_x(t)) + \exp(-q\alpha\delta t)(1-M_x(t))} \tag{2.8}$$

Equation (2.8) can be written as the following

$$M_x(t+\delta t) = \frac{\sinh(q\alpha\delta t) + M_x(t)\cosh(q\alpha\delta t)}{\cosh(q\alpha\delta t) + M_x(t)\sinh(q\alpha\delta t)} \tag{2.9}$$

where $q = \gamma_G H/(1+\alpha^2)$, and[3] $\gamma_G = \mu_0\gamma_0$. Equation (2.9) is analytically equivalent to equation (2.5). When the magnetic field is constant, *i.e.* $\omega = 0$, equations (2.5), (2.8) and (2.9) conserve the properties

[3] In Wiele *et al.* [51] γ_G is defined as the gyromagnetic ratio. Consistency with Châtel *et al.* [27] can be achieved by equating $\gamma_G = \mu_0\gamma_0$.

which need to be maintained while solving the LLG equation.
The value of M_x per cycle, as calculated in equations (2.8) and (2.9), agree when $\omega > 2\pi 10^{-3}$ rad s^{-1}. For $\omega \leq 2\pi 10^{-3}$ rad s^{-1}, the flipping of the direction of M_x is not captured in equation (2.9). This could be resolved using smaller time steps which significantly increases the computation time. Using equation (2.9), in order to obtain the correct nature of $\mathbf{M}$, there is a trade-off between the value of ω and computation time. As long as, $\omega > 2\pi 10^{-3}$, using either equations (equation (2.8) or equation (2.9)), a given value of analytical expression can be computed using the default precision. When all the constants, α, μ_0 and γ, are normalised and $\omega = 2\pi 10^{-3}$ rad s^{-1}, Figure 2.1 plots the values of M_x as equation (2.8) (form 1) and equation (2.9) (form 2). To generate Figure 2.1, the parameters given in table 2.2 are used,

ω	t	H	θ	M_x	M_y	M_z	α	μ_0	γ
$2\pi 10^{-3}$	$(0, 2\pi/\omega)$	$\lvert(\cos\omega t, 0, 0)\rvert$	$\pi/4$	$\sin\theta$	0	$\cos\theta$	1	1	1

Table 2.2: Table of constants for comparison between numerical methods.

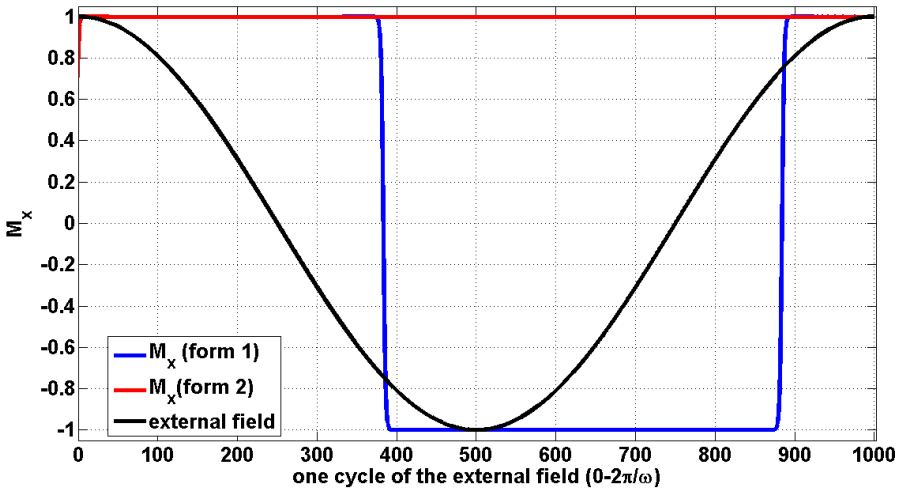

Figure 2.1: The values of M_x calculated as per equation (2.8) (blue line) and equation (2.9) (red line) when the time stepping is 10^{-3} s.

Figure 2.1 shows that when $\omega = 2\pi 10^{-3}$, equation (2.9) does not capture the true nature of the LLG equation. Therefore, it can be stated that certain forms of analytical expressions fail to capture the correct nature of the LLG equation in the lower range of frequencies, $f \leq 10^{-3}$ Hz.

2.4.1.3 Adaptive Runge-Kutta (RK) method

The techniques used to solve the LLG equation are adaptive RK (ode45), 4^{th} order RK (ode4), 5^{th} order RK (ode5), Euler's and midpoint methods. The following table is obtained when all the constants, α, μ_0 and γ, are normalised and $f = 10^{-3}$ Hz, *i.e.* $\omega = 2\pi 10^{-3}$ rad s^{-1}, *i.e.* the external field is effectively close to a static field. The absolute errors between the obtained numerical value of M_x and its approximated analytical value (as given in equation (2.5)) w.r.t. all the above mentioned methods are calculated. Here, error denotes the maximum absolute error over the total time, t. Adaptive RK gives the lowest error among these methods. Consequently, in the model (described in section 2.5 onwards) adaptive RK has been used.

Table 2.3: Table of errors obtained in RK (error_{RK}), Euler's (error_E) and midpoint (error_M) methods w.r.t. time step at $f = 10^{-3}$ Hz.

time step	**error$_{RK}$(ode45)**	**error$_{RK}$(ode4)**	**error$_E$**	**error$_M$**	**error(ode5)**
2.0004e−1	1.6904e−6	4.2266e−5	1.7357e0	4.7017e−2	1.6925e−6
1.0001e−1	5.2704e−8	1.3215e−6	9.9783e−1	6.1231e−3	5.2493e−8
2.0000e−2	1.0521e−8	1.0521e−8	1.1894e0	7.9875e−5	1.0520e−8
1.2500e−2	1.0504e−8	1.0521e−8	7.6876e−1	2.6032e−5	1.0521e−8
1.0000e−2	1.0504e−8	1.0521e−8	6.1921e−1	1.5599e−5	1.0521e−8

2.5 Model of the single particle

The total energy per unit volume, generated by a single MNP can be calculated from the product of the damping force and the distance covered by the unit magnetisation vector, $\mathbf{M}$, where the damping force can be defined as $\frac{\alpha}{\gamma_0} M_s|\dot{\mathbf{M}}|$ and the distance as $d\mathbf{M}$. The energy can be expressed as, $\frac{\alpha}{\gamma_0} M_s|\dot{\mathbf{M}}| \times d\mathbf{M} = \frac{\alpha}{\gamma_0} M_s|\dot{\mathbf{M}}|^2 dt$ and the energy dissipated in a single cycle can be calculated as

$$E = \frac{\alpha}{\gamma_0} M_s \int_0^{2\pi/\omega} |\dot{\mathbf{M}}|^2 dt \tag{2.10}$$

The energy in Châtel *et al.* is given by

$$E = \mu_0 \alpha_N M_s H \int_0^{2\pi/\omega} \cos^2 \omega t (1 - M_z^2) dt \tag{2.11}$$

E, from equation (2.11) is equivalent to the energy equation of Châtel *et al.* [27] as shown in section 2.6, that follows.

2.6 Equivalence of the energy equations, equations (2.10) and (2.11)

From the LLG equation

$$\dot{\mathbf{M}} = \mu_0 \gamma_0 g'(\mathbf{M} \times \mathbf{H}) + \mu_0 \gamma_0 \alpha g'(\mathbf{M} \times \mathbf{H}) \times \mathbf{M} \tag{2.12}$$

where $g' = \frac{1}{1+\alpha^2}$, $\mathbf{M} = \begin{pmatrix} M_x \\ M_y \\ M_z \end{pmatrix}$ and $\mathbf{H} = \begin{pmatrix} 0 \\ 0 \\ H_z \end{pmatrix}$

So,

$$\dot{\mathbf{M}} = \mu_0 \gamma_0 g' H_z \begin{pmatrix} M_y \\ -M_x \\ 0 \end{pmatrix} + \mu_0 \gamma_0 \alpha g' H_z \begin{pmatrix} -M_x M_z \\ -M_y M_z \\ M_x^2 + M_y^2 \end{pmatrix} \tag{2.13}$$

$$\implies \dot{\mathbf{M}} = \mu_0\gamma_0 g' H_z \begin{pmatrix} M_y - \alpha M_x M_z \\ -M_x - \alpha M_y M_z \\ \alpha(M_x^2 + M_y^2) \end{pmatrix} \tag{2.14}$$

$$\implies |\dot{\mathbf{M}}|^2 = (\mu_0\gamma_0 g' H_z)^2 \Big((M_y - \alpha M_x M_z)^2 + (-M_x - \alpha M_y M_z)^2 + \alpha^2 (M_x^2 + M_y^2)^2 \Big) \tag{2.15}$$

$$= (\mu_0\gamma_0 g' H_z)^2 [(M_x^2 + M_y^2) + \alpha^2 M_z^2 (M_x^2 + M_y^2) + \alpha^2 (M_x^2 + M_y^2)^2] \tag{2.16}$$

$$= (\mu_0\gamma_0 g' H_z)^2 (M_x^2 + M_y^2)[1 + \alpha^2 M_z^2 + \alpha^2 (M_x^2 + M_y^2)] \tag{2.17}$$

$$= (\mu_0\gamma_0 g' H_z)^2 (1 - M_z^2)[1 + \alpha^2 M_z^2 + \alpha^2 (1 - M_z^2)] \tag{2.18}$$

$$= (\mu_0\gamma_0 g' H_z)^2 (1 - M_z^2)[1 + \alpha^2] \tag{2.19}$$

$$= (\frac{\mu_0\gamma_0}{1 + \alpha^2} H_z)^2 (1 - M_z^2)[1 + \alpha^2] \tag{2.20}$$

Hence,

$$\implies |\dot{\mathbf{M}}|^2 = \frac{\mu_0^2\gamma_0^2 H_z^2 (1 - M_z^2)}{1 + \alpha^2} \tag{2.21}$$

The z component of $\mathbf{H}$ is, $H_z = H\cos\omega t$. Thus, the energy dissipation in a single cycle can be written as

$$\int_0^{2\pi/\omega} |\dot{\mathbf{M}}|^2 dt = \frac{\mu_0^2\gamma_0^2 H^2}{1 + \alpha^2} \int_0^{2\pi/\omega} \cos^2\omega t (1 - M_z^2) dt \tag{2.22}$$

$$\alpha \int_0^{2\pi/\omega} |\dot{\mathbf{M}}|^2 dt = \mu_0\gamma_0 H \left(\frac{\alpha\mu_0\gamma_0 H}{1 + \alpha^2}\right) \int_0^{2\pi/\omega} \cos^2\omega t (1 - M_z^2) dt \tag{2.23}$$

$$\frac{\alpha}{\gamma_0} \int_0^{2\pi/\omega} |\dot{\mathbf{M}}|^2 dt = \mu_0\alpha_N H \int_0^{2\pi/\omega} \cos^2\omega t (1 - M_z^2) dt \tag{2.24}$$

where $\alpha_N = \frac{\alpha\mu_0\gamma_0 H}{1+\alpha^2}$. Thus

$$\frac{\alpha}{\gamma_0} M_s \int_0^{2\pi/\omega} |\dot{\mathbf{M}}|^2 dt = \mu_0 \alpha_N M_s H \int_0^{2\pi/\omega} \cos^2 \omega t (1 - M_z^2) dt \tag{2.25}$$

Thus, the left hand side (our method) is equivalent to the energy expression in Châtel *et al.* as given in the right hand side. Therefore, equation (2.10) can be written as

$$E = \mu_0 \alpha_N M_s H \int_0^{2\pi/\omega} \cos^2 \omega t (1 - M_z^2) dt \tag{2.26}$$

The energy, E, from the one particle model has the low and high frequency asymptotes, $4\mu_0 M_s H$ and $\mu_0 \pi M_s H \frac{\alpha_N}{\omega}$ respectively. Good agreement with the numerical data (within 4%) is obtained from the following empirical formula, which is proposed by one of my supervisors Dr PJ Cregg.

$$E(\omega) = \frac{4\mu_0 M_s H}{\sqrt{1 + (\frac{\omega}{\omega_c})^2}} \tag{2.27}$$

This formula is based on the form of a first order low pass filter frequency response where choosing a cut-off frequency given by,

$$\omega_c = \frac{\alpha_N \pi}{4} \tag{2.28}$$

aligned the formula well with the data.

Figure 2.2 plots the energy E as given by equation (2.26), its empirical approximation given by equation (2.27), the high and low frequency asymptotes when $\alpha = 1$ and the initial value of $\theta = 0$.

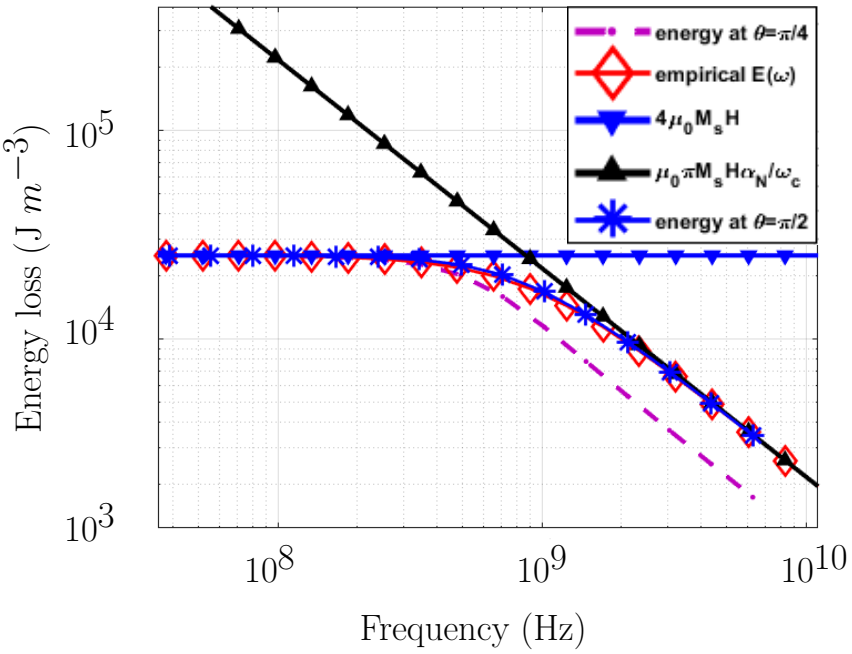

Figure 2.2: Plot of the energy as given in equation (2.26) when the initial polar angle $\theta = 0$ and $\theta = \pi/4$, empirical approximation of the energy, the low and high frequency asymptotes.

As shown in Figure 2.2, below $f = 10^8$ Hz, the value of E is well described by the low frequency

asymptote. The cut-off frequency varies with the initial value of θ, with the highest cut-off observed for $\theta = \pi/2$. For frequencies higher than the cut-off, E is well described by the high frequency asymptote, valid for $\theta = \pi/2$. The empirical formula (equation (2.27)) closely approximates the calculated E (equation (2.26)) throughout the frequency range, valid for $\theta = \pi/2$, thereby saving time and computational resources.

2.7 Model of n interacting MNPs

Given n particles, the total interaction field experienced by the i^{th} MNP as a result of the remaining $n-1$ MNPs, is given as

$$\mathbf{H}_{\text{int}}^{(i)} = M_s \sum_{j=1, j\neq i}^{n} \left(\frac{R}{|d^{(i,j)}|}\right)^3 \left[\left(\mathbf{M}^{(j)} \cdot \frac{\mathbf{d}^{(i,j)}}{|d^{(i,j)}|}\right) \frac{\mathbf{d}^{(i,j)}}{|d^{(i,j)}|} - \frac{1}{3}\mathbf{M}^{(j)}\right] \tag{2.29}$$

where $\mathbf{M}^{(j)}$ denotes the unit magnetisation vector of the j^{th} MNP, $\mathbf{d}^{(i,j)}$ is the difference between the locations of the centres of the i^{th} and the j^{th} MNPs, $\mathbf{d}^{(i,j)} = |\mathbf{d}^{(i,j)}|$ and R is the radius of each MNP. In our model, the MNPs are identical in terms of size and material properties.

2.8 Interpretation of Results

Dipole-dipole interaction introduces a new energy into the system. This energy is determined by the relative positions of the MNPs and also by the magnitude of the magnetic moments of each MNP.
If the arrangement of MNPs is as in Figure 2.3, the unit magnetisation vector, $\mathbf{M}$, of each of the MNPs is along the direction of the applied AC field, $\mathbf{H}$, resulting in zero precession, under the assumptions of no perturbations. It is noted that the LLG equation denotes the average precessional motion of an MNP in a magnetic field. In this thesis, stochastic dynamics have not been considered, but have been treated by García-Palacios *et al.* [52] and Ruta *et al.* [6].
For the touching MNPs, the unit magnetisation vectors, $\mathbf{M}$, are aligned head to tail causing the interaction field energy to be at its lowest energy state. Therefore Figure 2.3 indicates a state from which no heat is generated.

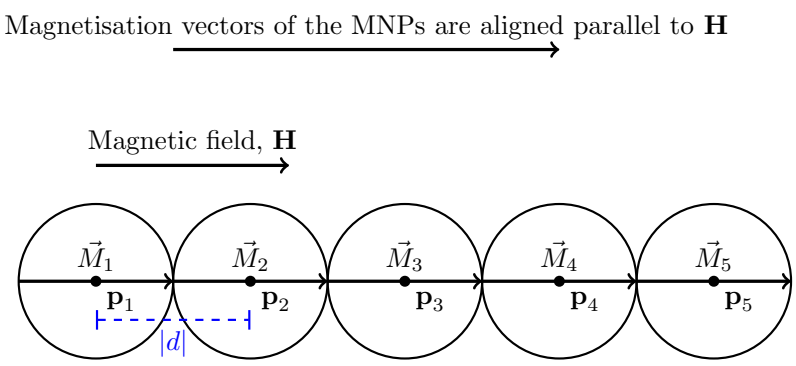

Figure 2.3: Arrangement of MNPs when the individual magnetic moments are head to tail and parallel to the field.

As depicted in Figure 2.4, a perpendicular $\mathbf{H}$ can move the vectors from their initial states of alignment, dissipating energy. This energy dissipation however can be less than would occur in the non-interacting case where the vectors would be free to fully align with the external field. Here, as

the vectors precess to align with the external field, the 'interaction field' changes direction with time. This can allow the interaction field to change from being additive to subtractive w.r.t. the AC field inhibiting further alignment. However, as the applied AC field reduces to zero, the interaction field then acts to realign the vector, thus dissipating extra 'interaction' energy. This is the mechanism of additional heating. The closer the MNPs, the stronger the interaction field; but additionally the closer the MNPs the less the applied field can move the vectors.

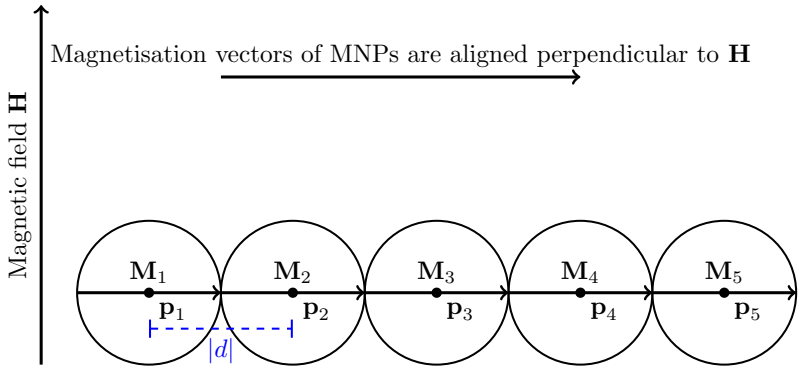

Figure 2.4: Arrangement of MNPs in the model, when the individual magnetic moments are head to tail and perpendicular to the field

Figure 2.4 describes a state from which maximum heating is generated by the MNPs. Similar obeservations with chain-like aggregates have been reported by [53].

2.8.1 Factors affecting SAR in multiple MNPs

The factors which affect the SAR in multiple MNPs are:

2.8.1.1 The initial angle, ζ, between the line joining the centres of the MNPs and the direction of the applied magnetic field, H

The initial value of the angle between the line joining the centres of the MNPs and the direction of **H**, ζ, affects the overall SAR. Figure 2.5 shows the change in heating with respect to ζ. It is found that at $\zeta = \pi/2$, as shown in Figure 2.4, maximum heating is generated.

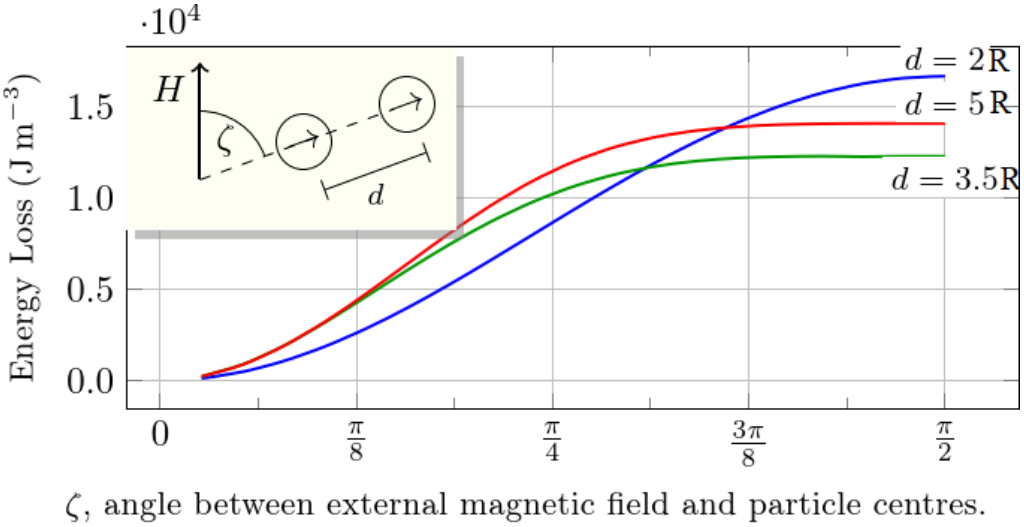

Figure 2.5: Effect of alignment of **M** with **H** on average energy.

From Figure 2.5 it can be concluded that initially as the value of ζ increases the overall SAR increases. At $\zeta = \pi/2$, the heating reaches its maximum value. Following the same pattern, futher increase in ζ, *i.e.* when $\pi/2 < \zeta \leq \pi$, should result in the decrease of the heating. The d in the legend of Figure 2.5 refers to the interparticle distance in terms of the radius of the MNPs, the effect of which is further explained in section 2.8.1.2.

2.8.1.2 The distance between the centres of the MNPs, d

The distance between the centres of the MNPs affects the strength of the interaction field. However, depending on the alignment of the magnetic moments of the MNPs, the direction of the interaction field can either be additive or subtractive w.r.t. the AC field, which in turn affects the precession of the magnetisation vector. It is found that when the MNPs are touching as depicted in Figure 2.4, the overall heating is the highest.

In Figure 2.6, when the centres of the MNPs are $2R$ apart *i.e.* the MNPs are touching, the average energy for two interacting MNPs is increased relative to the energy of one non-interacting MNP (the dotted line). Further away, the interaction field heating reduces until it is reaches d_0, where d_0 denotes the crossing point where the average energy of two interacting MNPs crosses the reference line of energy of a single MNP. At further separation, the interaction field energy contribution is seen to change sign and the dominating effect is the inhibition of the response to the applied field. Finally, at infinite separation when interaction effects are negligible, the average energy approaches the reference value. As given in Figure 2.6, the maximum average energy obtained for two interacting MNPs is 1.73342×10^4 J m^{-3}.

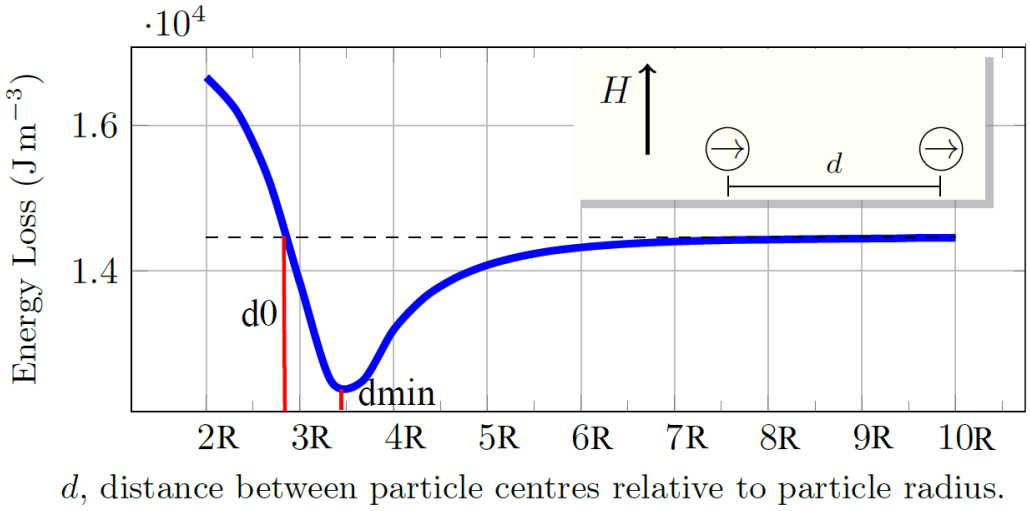

Figure 2.6: Effect of interparticle distance on average energy when $\zeta = \pi/2$

2.8.1.3 The M_s/H ratio

The M_s/H ratio influences the ease of alignment of **M** with the applied field. A high value of M_s/H decreases the alignment of the magnetisation vectors of the MNPs with **H**. In an alternating field, as **H** reduces to zero within each cycle, the interaction field realigns **M**, dissipating the extra energy. Therefore, the lower the initial alignment of **M** with respect to **H**, the higher is the value of the dissipated energy.

In Figure 2.7 the behaviour for the two particle chain is presented with a fixed value of $H = 10$ kA/m,

and a range of M_s values beginning with a reference magnetisation value of $M_s = 0.5$ MA/m with a ratio of $M_s/H = 50$. The heating/energy ratio is calculated in terms of energy per cycle per particle and divided by the energy of a single non-interacting particle, as a function of (centre to centre) interparticle distance over particle radius. The normalised behaviour shows considerable regularity with variation in M_s/H; the energy ratio saturates at 1.18. From Figure 2.7 it can be said that the M_s/H ratio has a significant impact on heating generated by the MNPs. As the ratio increases, the maximum value of heating is achieved even with increased interparticle distance.
As evidenced in table 2.4, both d_0 and the position of minimum energy of two interacting MNPs, $d_{\min}$, exhibit a $\sqrt[3]{\frac{M_s}{H}}$ dependence with good agreement observed with the following empirical formulae;

$$d_0 = \frac{\pi}{4}\sqrt[3]{\frac{M_s}{H}} \tag{2.30}$$

and

$$d_{\min} = 0.95\sqrt[3]{\frac{M_s}{H}} \tag{2.31}$$

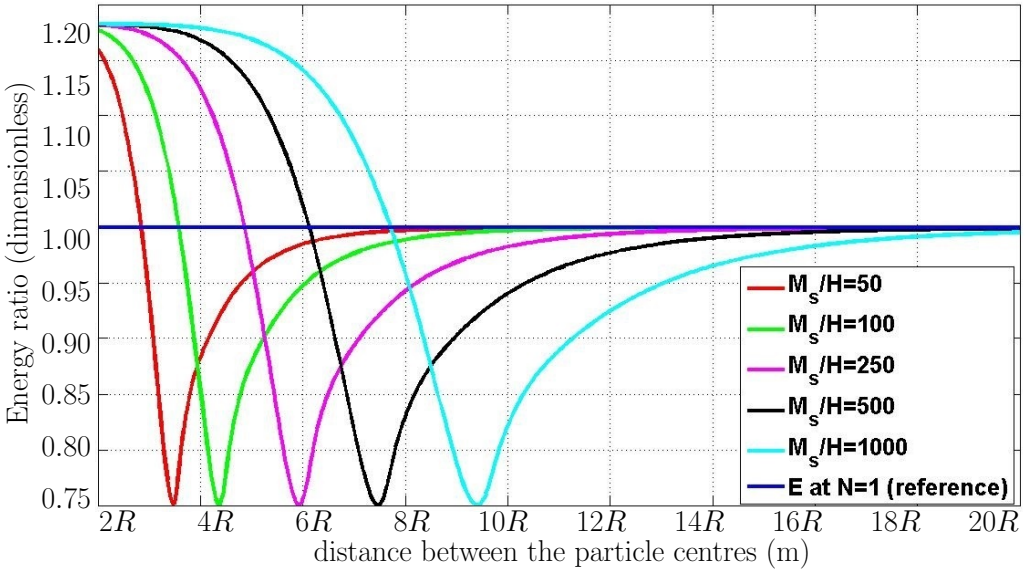

Figure 2.7: Effect of increasing M_s/H ratio on average energy per cycle for two MNPs, $N = 2$.

Table 2.4: Table generating the empirical and simulated values of d_0 and $d_{\min}$ for $N = 2$.

M_s/H	d_0	d_0 (empirical)	Relative % error	d_{min}	d_{min} (empirical)	Relative % error
50	2.909	2.849	2.063	3.489	3.4998	0.3095
100	3.636	3.645	0.2475	4.392	4.4095	0.3985
500	6.232	6.234	0.0321	7.504	7.540	0.4797
1000	7.818	7.854	0.0460	9.498	9.5	0.0211

2.9 Heating generated by multiple MNPs

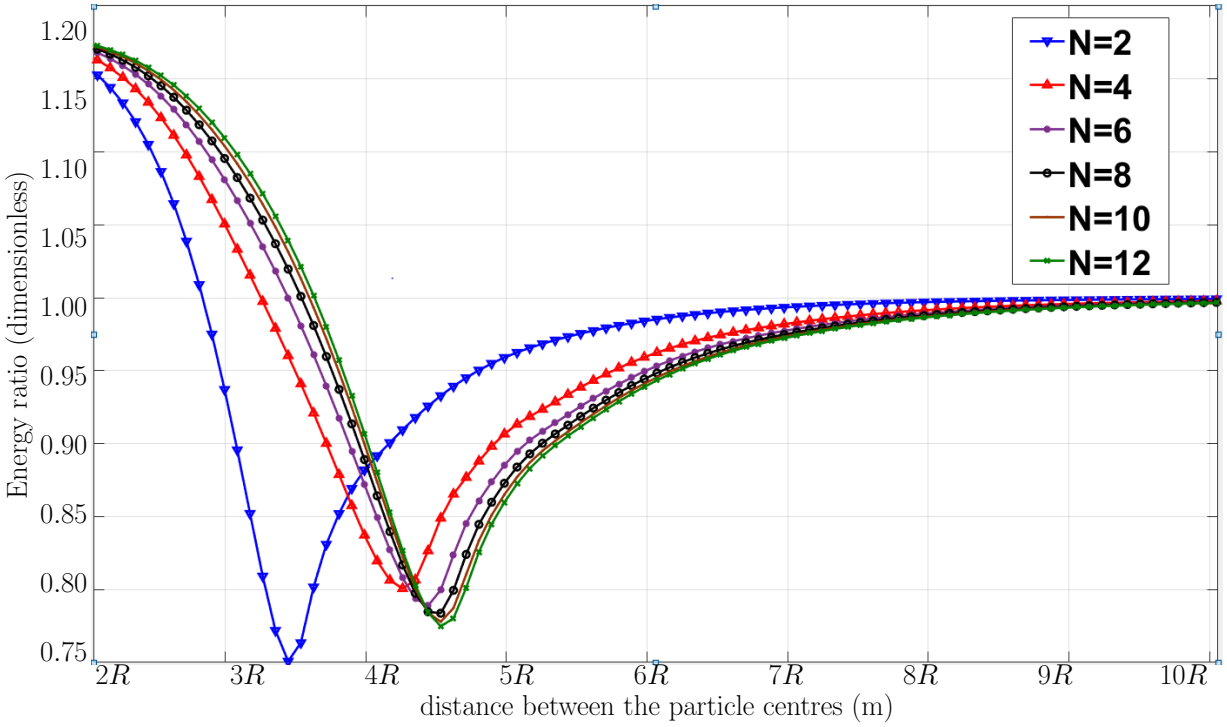

Figure 2.8: The effect of increasing the number of MNPs on the average energy per cycle.

As seen in Figure 2.8 the maximum additional heating in multiple MNPs almost reaches saturation when $N \geq 8$. This indicates that increasing the number of MNPs does not necessarily increase the generated heating. This phenomenon has been noted in [4]. The available computational power set a limit of $N = 12$ in this simulation. Future work might investigate the effect of further increasing the value of N.

2.10 Coating thickness for manufacturing MNPs

Maximum heating is obtained when the MNPs are touching, *i.e.* when the MNPs do not have any coating. However, in the cases where the MNPs need to be coated, in order to increase heating, a coating size, c_t, can be tailored so that for touching particles, the heating is enhanced. Thus a condition for enhanced heating can be given by

$$c_t < \frac{d_0}{2} - 1 \tag{2.32}$$

For example, in Figure 2.7, when $M_s/H = 50$, $d_0 \approx 2.8R$. Thus, from equation (2.32), for two interacting MNPs, in order to get enhanced heating, $c_t < 0.4R$.

The expression given by equation (2.32) can be beneficial during the aggregation of MNPs occurring due to dipolar interactions. To prevent aggregation and therefore to get a specific value of heating, authors such as Wu *et al.* [7] have only considered MNPs of a certain size which is 22 nm or less. Irrespective of the sizes of the MNPs, equation (2.32) can be used to adjust the heating in an aggregation of MNPs by adjusting their coating thickness.

2.11 Conclusion

In the single particle model, the energy has the low and high frequency asymptotes, $4\mu_0 M_s H$ and $\mu_0 \pi M_s H \frac{\alpha_N}{\omega}$ respectively. An empirical formula for energy has been developed which is based on the form of a first order low pass filter frequency response where choosing a cut-off frequency given by $\omega_c = \frac{\alpha_N \pi}{4}$ aligned the formula well with the data. For multiple particles, the transverse chain arrangement is found to be the most favourable observed. In practice, this tranverse chain arrangement could be achieved by aligning the MNPs with a static magnetic field prior to the application of the perpendicular alternating magnetic field. When the magnetic field is perpendicular to the magnetic moment of the MNPs and the MNPs are aligned head to tail, it is observed that interparticle interactions aid the heating, given the interparticle distance, $d_0 \leq \sqrt[3]{\frac{M_s}{H}}$. In all other cases the interparticle interactions hinder the heating mechanism. Therefore, it can be concluded that as a result of dipole-dipole interactions, the M_s/H ratio plays a significant role in the heating of MNPs. Equations (2.30) and (2.32), could be used to predict the coating thickness required for optimum heating in the manufacturing of MNPs in MHT. The empirical approximates as given in section 2.8, should allow designers to determine the limit on the coating thickness which might still allow enhanced heating. It is noted that anisotropy is likely to enhance the inhibition of the applied field response. Therefore, the inclusion of anisotropy can be expected to inhibit the MNPs delivering this enhanced heating. In this work the effects of anisotropy are not explored but might be included in the future.

As seen in Figure 2.8 the maximum additional heating in multiple MNPs almost reaches saturation when $N \geq 8$. This indicates that increasing the number of MNPs does not necessarily increase the generated heating. The available computational power set a limit of $N = 12$ in this simulation. Future work might investigate the effect of further increasing the value of N.

In this work, the MNPs are considered to be spherical for the ease of modelling. The amount of heating is expected to change if the shapes of the MNPs are altered. Future work might investigate the effect of the shapes of the MNPs on the overall heating.

Chapter 3

Magnetic cell delivery

Magnetic Cell Delivery (MCD) is the delivery of healthy cells to diseased targets using MNPs as carriers guided by magnetic fields. Existing theoretical models differ significantly from experimental results, which according to researchers, specifically Riegler et al., is most likely due to neglect of magnetic interactions. To model interparticle interactions in parabolic flow later in the thesis, in this chapter two papers and a thesis of Riegler et al. have been replicated and verified.

3.1 Additional list of symbols

- D_c, duty cycle for steering gradients ..... dimensionless
- R_c, cell radius ..... m
- $\frac{\partial B_z}{\partial x}$, external gradient ..... $\mathrm{T\,m^{-1}}$
- W, initial distribution of cells ..... m
- v_c, cell velocity ..... $\mathrm{m\,s^{-1}}$
- T_e, Targeting efficiency ..... dimensionless
- e, eccentricity of an ellipse ..... dimensionless
- a, major axis of an ellipse ..... m
- c, minor axis of an ellipse ..... m
- K_n, Stokes correction factor using the surface equivalent diameter for non-spherical objects ..... dimensionless
- K, Stokes correction factor using the volume equivalent diameter for non-spherical objects ..... dimensionless
- $l_r = c/a$, aspect ratio of ellipse/spheroid ..... dimensionless
- d_n, diameter of a sphere with the same projected area as that of the area of the spheroid projected normal to its direction of motion ..... m
- d_s, diameter of a sphere with the same total surface area as the spheroid ..... m
- $f_\perp$, volume equivalent Stokes correction factor for the drag perpendicular to the axis of symmetry ..... dimensionless
- $f_{||}$, volume equivalent Stokes correction factor for the drag parallel to the axis of symmetry ..... dimensionless

Table 3.1: List of parameters values for chapter 3.

Parmeter	Description	Value
η	viscosity	1.6×10^{-3} kg m^{-1} s^{-1}
$\frac{\partial B_z}{\partial x}$	magnetic gradient	0.5 T m^{-1}
D_c	duty cycle for steering gradients	2/7
R_v	circular tube radius	0.4×10^{-3} m
n	number of super paramagnetic iron oxide(SPIO) particles per cell as given in Riegler *et al.*	455×10^3(Endorem)
M_s	saturation magnetisation	314×10^3 A m^{-1}
R_c	cell radius	5×10^{-6} m
R	radius of the MNP	10×10^{-9} m(Endorem)
$\overline{v}_f$	average fluid velocity	0.001 to 0.07 m s^{-1}

3.2 Introduction

Magnetic particle imaging (MPI) is a new tomographic imaging method potentially capable of rapid 3D dynamic imaging of magnetic tracer materials [54]. Magnetic resonance imaging (MRI) can provide detailed images of the structure and functioning of the body. MRI produces images of all organs and this is useful in analysis and during the course of therapy [26]. MPI and MRI can be used in conjunction with magnetic drug targeting (MDT) where real time imaging can monitor the *in vivo* distribution of the MNPs. The use of MRI systems to steer magnetic objects deep inside the body has gained attention recently [55–60]. This is particularly appealing due to the high magnetic field strength, and the precise spatial and temporal control over magnetic field gradients provided by an MRI system. Combining this functionality with the conventional MRI used to generate high contrast soft tissue images may allow for interactive real time feedback for the spatial position of the cells, and/or immediate confirmation of targeting success, as cells labelled with MNPs appear hypointense or dark on MR images. Regenerative medicine replaces old, diseased cells with healthy cells, and includes applications in cell delivery and bone marrow transplantation. Magnetic Cell Delivery (MCD) is an emerging technique in regenerative medicine for the delivery of healthy cells to the diseased targets using MNPs as carriers guided by magnetic fields. In MCD for stem cell transplantation, Moysidis *et al.* [15] have reported a magnetic field guided cell delivery system employing MNPs to treat the human eye and have presented promising results. Gonzalez-Molina *et al.* [13] have presented results for MCD in tubular constructs which resemble the natural lumens of biological systems such as circulatory and respiratory systems. The importance of the modelling of interactions in the targeting efficiency has been higlighted in the literature [14, 61] but not thoroughly investigated. Riegler *et al.* [11] have produced experimental results in MCD which differ widely from their own theoretical predictions. This disagreement persists from 2010 and to the best of my knowledge this problem has not yet been resolved. This disagreement was attributed to aggregation of MNPs and these authors specifically mentioned that the disagreement between the theoretical and experimental results is mainly due to the neglect of interparticle interactions in their model. The absence of modelling dipolar interactions in the literature is most likely due to the fact that including dipolar interactions between the MNPs is a considerable modelling task requiring substantial knowledge of physics, and computational expertise.

In this chapter, the numerical models in Riegler *et al.* [11, 12, 62] have been replicated. Disagreements encountered while replicating the models have been outlined along with the attempts to reconcile the discrepancies.

3.3 Physical setup

The physical setup given in Riegler *et al.* [11] is depicted in Figure 3.1. The mathematical model described in [11] investigates the ability of MRI scanners to deflect cells filled with MNPs to a chosen outlet of a bifurcation phantom.

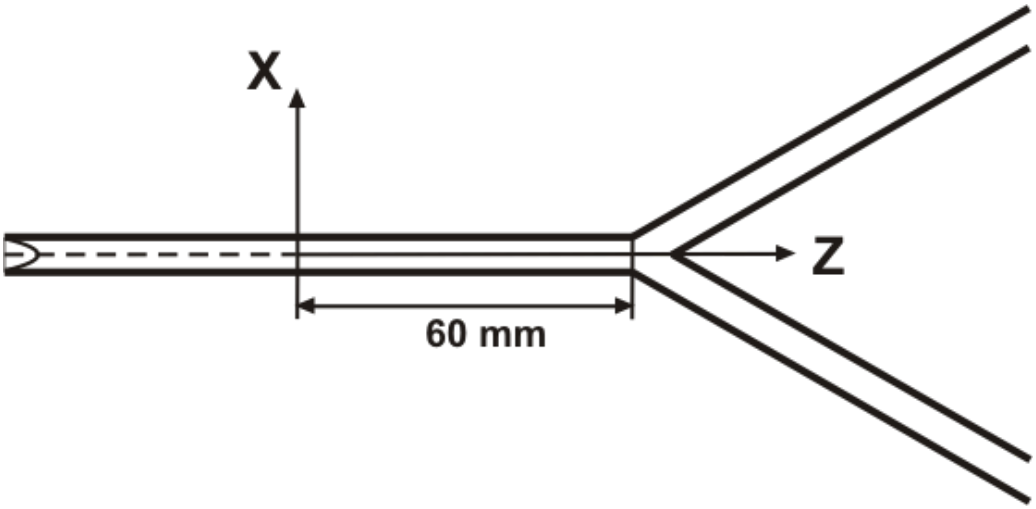

Figure 3.1: Schematic drawing of the bifurcation phantom.

Figure 3.1 refer to bifurcation phantom used in [11].

3.4 Model of Riegler et al.

The force experienced by an MNP in a magnetic field, is given by

$$\mathbf{F}_m = \nabla(\mathbf{m} \cdot \mathbf{B}) = (\mathbf{m} \cdot \nabla)\mathbf{B} = nV(\mathbf{M} \cdot \nabla)\mathbf{B} \tag{3.1}$$

where n is the number of MNPs inside one cell ($n \in \mathbb{N}$), V is the volume of the MNPs, $\mathbf{B}$ is the magnetic flux density. The mathematical model described is two dimensional with the applied gradient only along the x-axis. Thus, equation (3.1) can be written as

$$F_{m,x} = nV D_c M_s \frac{\delta B_z}{\delta x} = F_m \tag{3.2}$$

V is the volume of each particle, $\frac{\delta B_z}{\delta x}$ is the external gradient, D_c is the duty cycle for the gradient and M_s is the saturation magnetisation.
The main force which needs to be overcome by the magnetic force is the drag force of the fluid, given as

$$F_d = -6\pi\eta R_c(v_c - v_f) \tag{3.3}$$

where η is the viscosity, R_c is the radius of the cells, v_c is the velocity of the cells and v_f is the fluid velocity. A laminar flow is assumed in the tube with the flow profile as

$$v_f(x) = 2\overline{v}_f \left[1 - \left(\frac{x}{R_v}\right)^2\right] \tag{3.4}$$

where R_v is the radius of the tube and $\overline{v}_f$ is the average fluid velocity in the tube. The trajectory of cells can be calculated by equating the magnetic and the drag force (see Figure 3.2).

$$F_m = F_d \tag{3.5}$$

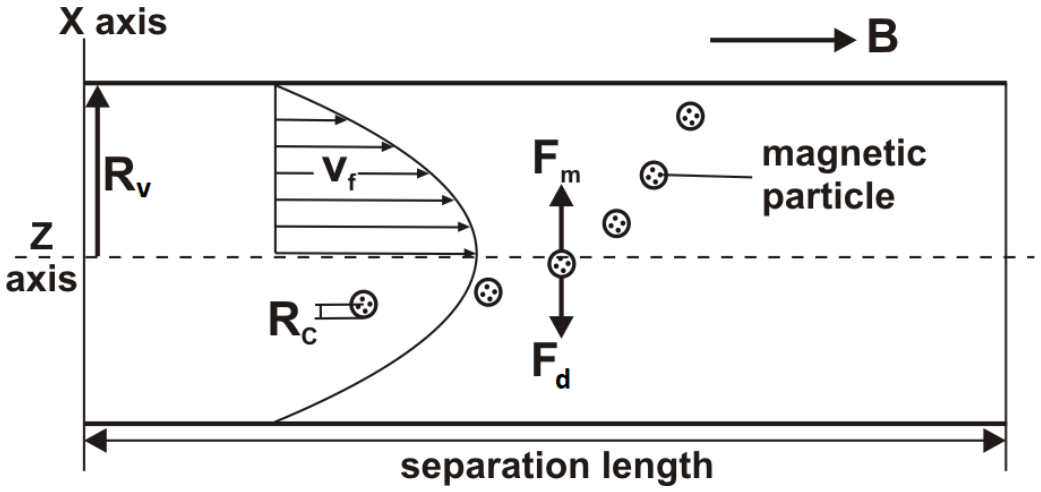

Figure 3.2: Schematic drawing for the direction of the forces for a positive x gradient taken directly from [11].

The cell trajectory along the x-axis is given as

$$\frac{dx}{dt} = \frac{nVD_cM_s\frac{\delta B_z}{\delta x}}{6\pi\eta R_c} \tag{3.6}$$

The cell velocity in the z-axis is determined solely by the fluid velocity, as there is no magnetic force acting along the z-axis.

$$\frac{dz}{dt} = 2\overline{v}_f \left[1 - \left(\frac{x}{R_v}\right)^2\right] \tag{3.7}$$

The cell position along the x-axis is

$$x(t) = x_0 + v_c t \tag{3.8}$$

where v_c denotes the cell velocity due to the magnetic force.
Integrating equation (3.7) yields

$$z(t) = 2t\overline{v}_f \left(1 - \frac{t^2 v_c^2}{3R_v^2} - \frac{tv_c x_0}{R_v^2} - \frac{x_0^2}{R_v^2}\right) \tag{3.9}$$

For the calculation of targeting efficiency, it is assumed that initially the cells are randomly distributed

over the circular tube cross-section. The projection of the initial distribution into the plane is given as [12]

$$W(x) = 2R_v \sin\left(\cos^{-1}\left(\frac{x}{R_v}\right)\right) \tag{3.10}$$

The trajectories for cells can be calculated using equations (3.8) and (3.9). If this is weighted with equation (3.10), the distribution at the start and end of the separation distance can also be calculated. It is assumed that cells which are above or below the axis, $x = 0$, at the end of the separation length, ($z = 60$ mm), will end up in their corresponding exit tubes. The targeting efficiency can hence be defined at that point as

$$T_e = 2\left(\frac{n_{\text{target\_tube}}}{n_{\text{total}}} - 0.5\right) \tag{3.11}$$

where $n_{\text{target\_tube}}$ is the number of cells at the end of the tube to which the cells were targeted and n_{total} is the total number of cells.

3.5 Materials: Endorem & BioMag

Endorem is a suspension of superparamagnetic iron oxide particles used as a contrast agent in MRI. The contrast agent consists of dextran-coated iron oxide particles with a general size distribution between $120 - 180$ nm and an iron concentration of 7.1 mg ml^{-1}. Before Endorem received approval as a contrast agent in Germany and other European countries, clinical trials were performed in Japan, the USA, and Europe [63, 64]. In Riegler *et al.* Endorem has suspension iron concentration of 11.2 g l^{-1} and was manufactured by Guerbet Laboratories Ltd, UK.

BioMag is composed of magnetic particles with affinity binding proteins may be coated with the primary antibody or biotinylated molecule of interest through a straightforward incubation [65]. They are also suitable for off-the-shelf use in applications, such as immunoprecipitation or PCR product clean-up. In [11], it has been mentioned that the nominal radius for BioMag particles is around 0.75 µm and their iron concentration is 0.8 mg/ml iron. In Reigler *et al.* BioMag particles were manufactured by Bangs Laboratories Inc, Indiana, USA.

3.6 Trajectory of Endorem labelled cells

The data for the Endorem particles are given in table 3.1, corresponding to the appendix of Riegler *et al.* [11]. Figures 3.3a to 3.3c display the trajectories of the cells obtained at two different flow rates.

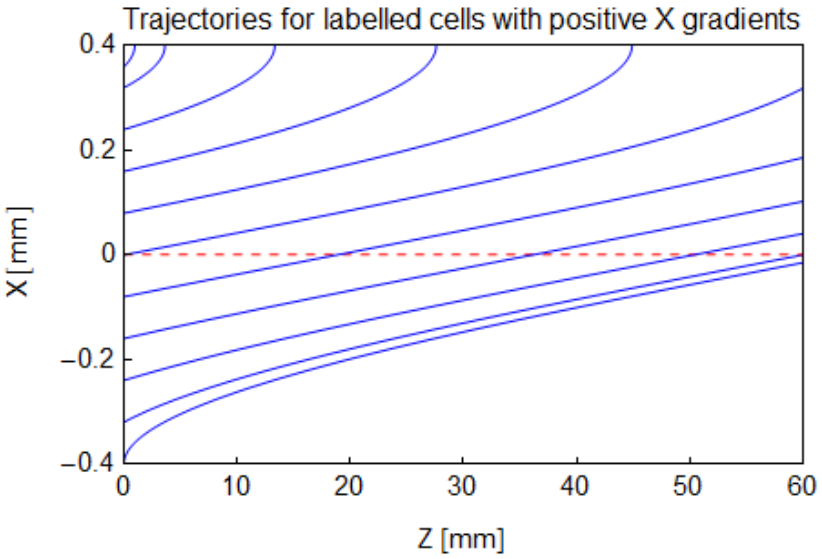

(a) Trajectory taken directly Riegler *et al.* Figure 3.3a, when v_f is 10^{-4} m s^{-1}.

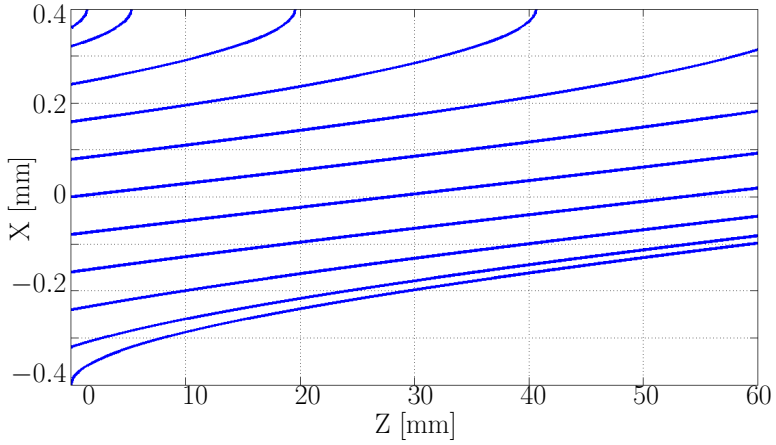

(b) Trajectory obtained when v_f is 10^{-4} m s^{-1}.

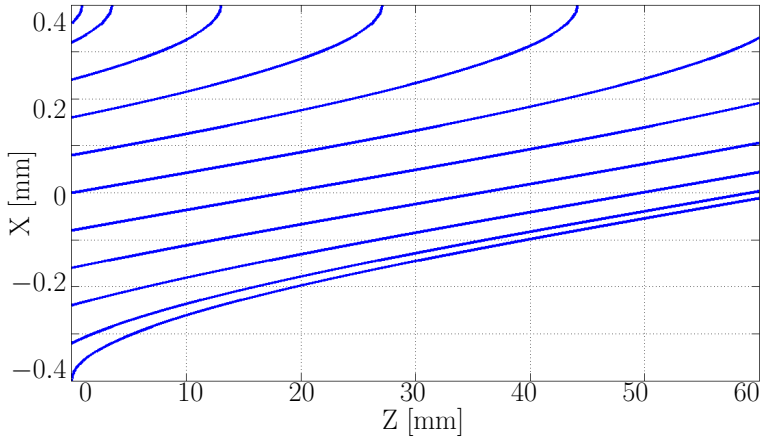

(c) Trajectory obtained when v_f is $\frac{1}{1.5} \times 10^{-4}$ m s^{-1}.

Figure 3.3: Plot of trajectory of Endorem cells.

Using the parameters given in Riegler *et al.* (table 3.1), Figure 3.3b was obtained. However, close agreement is obtained with Figure 3.3a in Figure 3.3c, applying either of the following conditions.

1. increase the magnetic steering gradient, $\frac{\partial B_z}{\partial x}$, by a factor of 1.5.

2. decrease the fluid velocity, v_f, by a factor of 1.5.

If $a = 1.5$, then

$$\frac{v_{f,old}}{a} = v_{f,new} \tag{3.12}$$

$$aB_{z,old} = B_{z,new} \tag{3.13}$$

Figure 3.3a displays the trajectories of Endorem cells presented in Riegler *et al.*. Figure 3.3b displays the replicated result. In order to make the the simulation results comparable to the published ones, the parameters v_f and B_z are decreased and increased respectively by using the factor, a as dispalyed in Figure 3.3c. It would appear likely that this discrepancy is due to a typographical or numerical error.

3.7 Targeting efficiency of Endorem labelled cells

In the model of Riegler *et al.*, the cells are filled with n particles. The two types of particles used in [11], are Endorem and BioMag. Endorem particles have a nominal diameter of $80 - 150$ nm and a suspension iron concentration of 11.2 $\mathrm{mg\,ml^{-1}}$. The nominal diameter for BioMag particles is 1.5 µm and their suspension iron concentration is approximately 0.8 $\mathrm{mg\,ml^{-1}}$. Each cell is labelled with Endorem particles where $n = 455 \times 10^3$. Figures 3.4a to 3.4c display the targeting efficiency of Endorem labelled particles with respect to v_f.

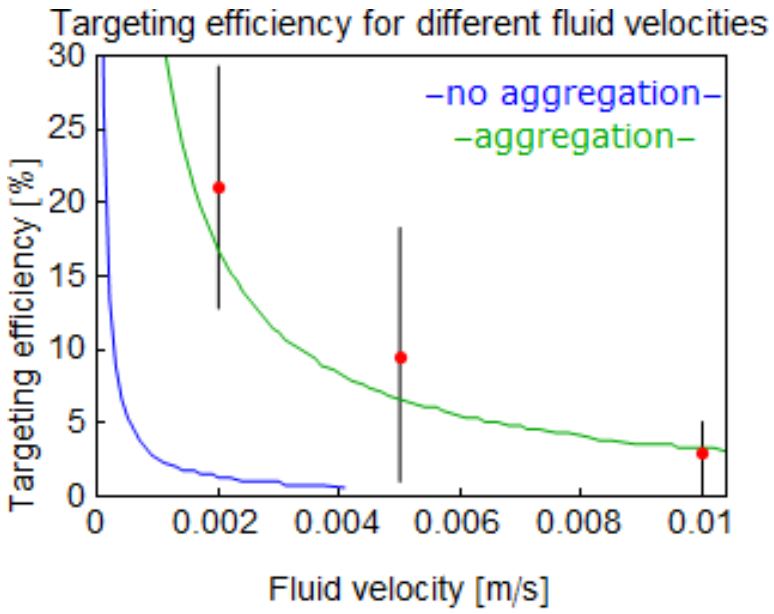

(a) Targeting efficiency with respect to v_f taken directly from Riegler *et al* [11].

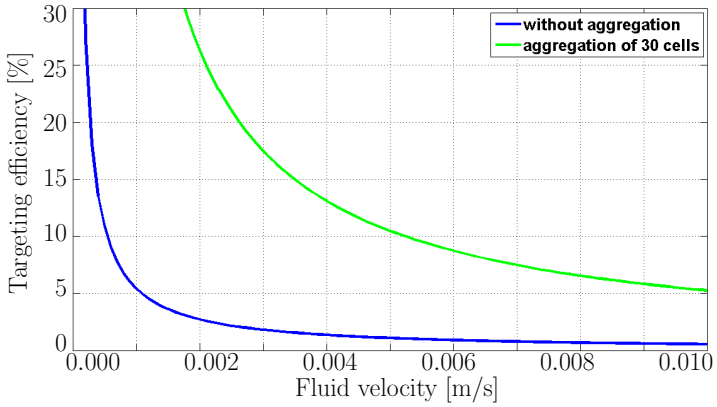

(b) Targeting efficiency with respect to v_f obtained in this work.

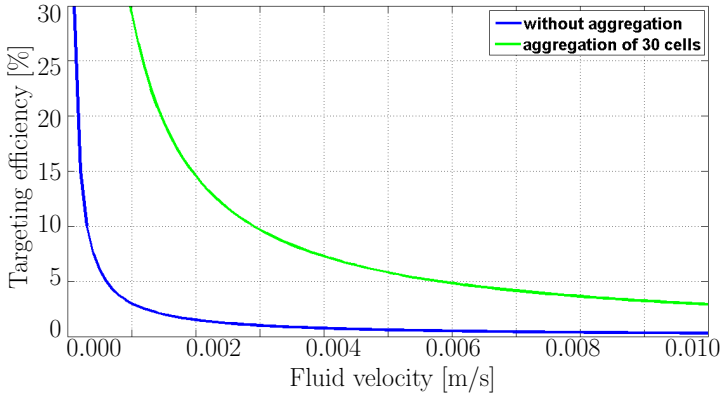

(c) Targeting efficiency with respect to obtained when $\frac{\partial B_z}{\partial x} = \frac{1}{1.8137} \times 0.5\,\mathrm{T\,m^{-1}}$

Figure 3.4: Plot of targeting efficiency of Endorem cells with respect to fluid velocity, v_f.

Figure 3.4a is the graph (4A) in the appendix of Riegler *et al.* [11] for Endorem labelled cells. Figure 3.4b is the graph obtained for Endorem labelled cells with the values R and n as given in table 3.1. Figure 3.4c more closely agrees with to Figure 3.4a, generated by applying either of the following conditions:

1. decrease the magnetic steering gradient, $\frac{\partial B_z}{\partial x}$, to 1.8137 times of its original value,

2. increase the fluid velocity, v_f, by 1.8137 times of its original value,

If $b = 1.8137$,

$$bv_{f,old} = v_{f,new} \tag{3.14}$$

$$\frac{B_{z,old}}{b} = B_{z,new} \tag{3.15}$$

In both cases, increasing B_z or decreasing v_f has the same effect on the targeting efficiency. This can be understood as the magnetic force depends on $\frac{\partial B_z}{\partial x}$ and the drag force depends on v_f respectively. Thus $\frac{\partial B_z}{\partial x} v_f$ is a constant for a resulting targeting efficiency.

3.8 Targeting efficiency of BioMag labelled cells

Figure 3.5a plots the targeting efficiency of the combination of 40 cells into a spherical mega-cell. This increases the magnetic force more than the drag force as the former scales with volume and the latter with surface area.

In [11], it has been mentioned that the nominal radius for BioMag particles is around 0.75 µm and their iron concentration is 0.8 mg/ml iron. Since the number of BioMag particles per cell, n, is not given in [11], it has been calculated by the following expression.

$$R = \sqrt[3]{\frac{Fe_c}{\rho_{Fe} n}} R_c \tag{3.16}$$

$$\Leftrightarrow n = \frac{Fe_c}{\rho_{Fe} R^3} {R_c}^3 \tag{3.17}$$

where Fe_c is the concentration of iron and ρ_{Fe} is the relative density of iron with respect to water. Using equation (3.17), I get $n \approx 29$. If this value of n is used as the number of BioMag particles per cell, a huge deviation is obtained from the published graph. The deviation can be observed by comparing the published graph (Figure 3.5a) and the obtained graph using $n = 29$ (Figure 3.5b). The BioMag particles are micron sized, *i.e.* bigger than the Endorem particles and $n = 29$ increases the magnetic force, F_m, 29 times. Thus, a higher targeting efficiency is to be expected.

However, another article by Riegler *et al.* [12], states the iron concentration for micron sized particles (supposedly BioMag) to be 0.5 mg/ml iron and, $n = 250$. Using $Fe_c = 0.5$ mg/ml and $n = 250$ in equation (3.16), the radius of the particle, $R \approx 0.3 \times 10^{-6}$ m. Using this value of R instead of 0.75×10^{-6} m, Figure 3.5c plots the targeting efficiency with respect to v_f. Figure 3.5c is qualitatively closer to Figure 3.5a than Figure 3.5b.

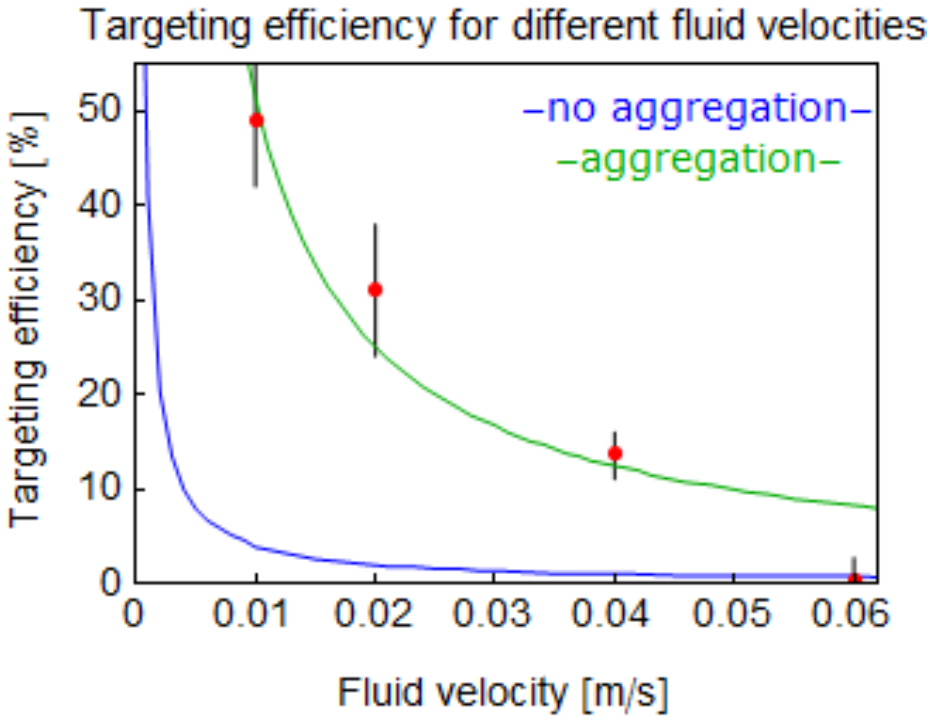

(a) Targeting efficiency with respect to v_f for BioMag particles (aggregation of 40 cells), taken directly from Riegler *et al.* [11].

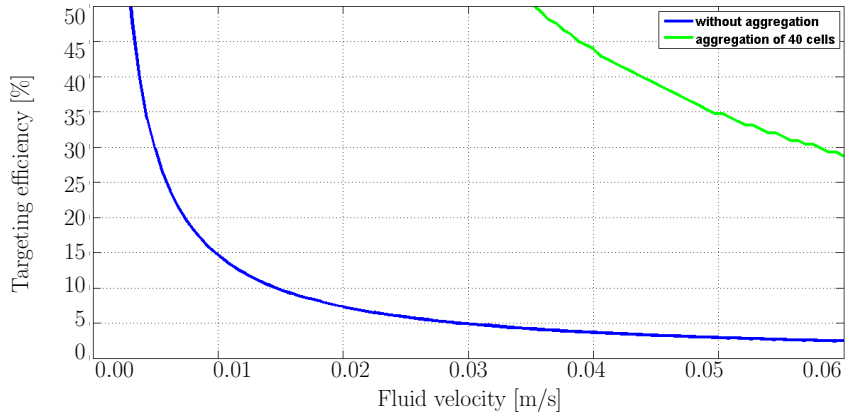

(b) Targeting efficiency with respect to v_f obtained when $R = 0.75\mu m$ and $n = 29$.

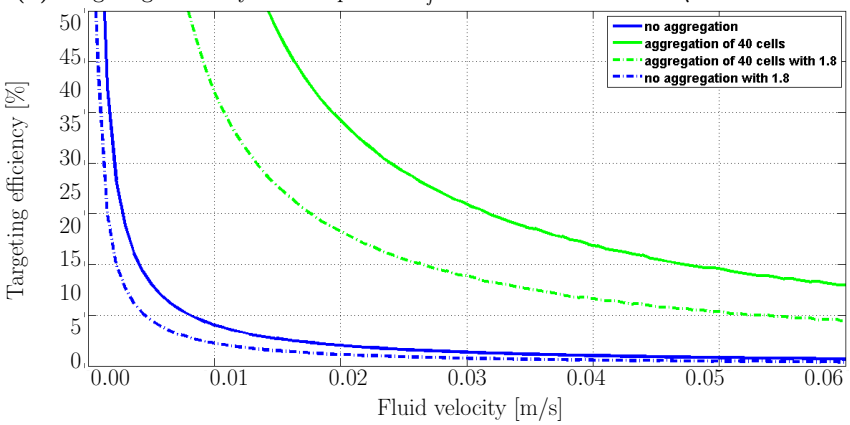

(c) Targeting efficiency with respect to v_f obtained when $\frac{\partial B_z}{\partial x} = \frac{1}{1.8137} \times 0.5\,\mathrm{T\,m^{-1}}$, $R = 0.3$ µm and $n = 8$.

Figure 3.5: Plot of obtained targeting efficiency of BioMag labelled cells with respect to v_f.

Figure 3.5a displays the published graph in [11], Figure 3.5b displays the obtained graph and

Figure 3.5c displays the revised graph. As discussed earlier, BioMag particles being bigger than Endorem particles are expected to have a higher targeting efficiency and therefore the targeting efficiencies displayed in Figures 3.5b and 3.5c are expected. The discrepancies with the published result may be accounted to numerical and/or typographical errors.

3.9 Stokes correction factor

An ellipsoid is a 'squashed' or 'stretched' sphere, technically known as an oblate or prolate spheroid, respectively. The Stokes drag is different in both the prolate and oblate spheroid and this difference can be expressed by a Stokes correction factor. The Stokes correction factor can be defined as the coefficient by which the drag of a sphere of the same volume is multiplied, in order to compensate for the fact that the object is not spherical. The drag of a spheroid will depend on both the degree of non-sphericity and its orientation to the flow.

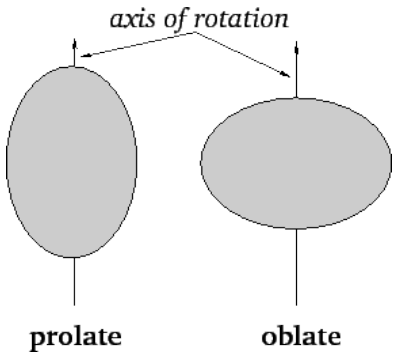

Figure 3.6: Prolate and oblate spheroid.

Riegler *et al.* [12], presented results for the targeting efficiency where the cells aggregate in the form of a spheroid instead of a sphere. Because of the following discrepancies, a review on the different expressions of Stokes correction factors is presented in section 3.9.1 and efforts have been made to correlate these.

1. Qualitative and quantitative agreement with the results from Riegler *et al.* [12] could not be obtained.

2. Various authors have used different formulations for the Stokes correction factor involving volume, surface and perimeter equivalence. [66, 67].

3. Riegler *et al.* [12] referenced Leith [67] to calculate the form factor, K_n. However, derivation of K_n from Leith, as given in section 3.9.1, concludes that the value of K_n used in Riegler *et al.* [12], is incorrect.

3.9.1 Comparison of the form factors

3.9.1.1 Form factor in Leith

The form factor in Leith [67] is given as

$$K_n = \left[\frac{1}{3} + \frac{2d_s}{3d_n}\right] \tag{3.18}$$

where d_n is the diameter of a sphere with the same projected area as the area of the object projected normal to its direction of motion while d_s is the diameter of a sphere with the same total surface area as the object.

The form factor, for a prolate spheroid, in Riegler *et al* [12] is given as

$$K_n = \left[\frac{1}{3} + \frac{2}{3}\frac{a^2 + \frac{ac}{e}\sin^{-1} e}{2ac}\right] \tag{3.19}$$

where a is the minor axis, c is the major axis and $e = \sqrt{1 - \frac{a^2}{c^2}}$. However, reducing equation (3.18) (as given in section 3.9.1.2) for a prolate spheroid, when projected perpendicular to its axis of rotation I get

$$K_n = \left[\frac{1}{3} + \frac{2}{3}\sqrt{\frac{a^2 + \frac{ac}{e}\sin^{-1} e}{2ac}}\right] \tag{3.20}$$

3.9.1.2 Reduction of equation (3.18)

Prolate spheroid

To calculate the diameter of a sphere, d_s, with the same total surface area as a prolate spheroid, the surface area of a sphere and a prolate spheroid are equated. Thus

$$4\pi\left(\frac{d_s}{2}\right)^2 = 2\pi a^2\left(1 + \frac{c}{ae}\sin^{-1} e\right) \tag{3.21}$$

$$\Rightarrow d_s = \sqrt{2\left(a^2 + ac\frac{\sin^{-1} e}{e}\right)} \tag{3.22}$$

- The prolate spheroid can be projected mainly in two directions, *i.e.* along its minor and major axis. If the prolate spheroid is projected, perpendicular to its axis of rotation, the projection resembles an ellipse of major and minor axis c and a. Thus, to calculate the diameter of a sphere with the same projected area (a circle) as the area of the prolate spheroid projected normal to its direction of motion (an ellipse), the area of the circle and the ellipse are equated, yielding

$$\pi\left(\frac{d_n}{2}\right)^2 = \pi ac \tag{3.23}$$

$$d_n = 2\sqrt{ac} \tag{3.24}$$

  Using equations (3.22) and (3.24)), equation (3.18) can be written as

$$\left[\frac{1}{3} + \frac{2}{3}\frac{d_s}{d_n}\right] = \left[\frac{1}{3} + \frac{2}{3}\sqrt{\frac{a^2 + \frac{ac}{e}\sin^{-1} e}{2ac}}\right] \tag{3.25}$$

  Equation (3.25) is equivalent to equation (3.20).

- If the prolate spheroid is projected in the direction along its axis of rotation, the projection

resembles a circle of radius a, so that

$$\pi\left(\frac{d_n}{2}\right)^2 = \pi a^2 \tag{3.26}$$

$$d_n = 2a \tag{3.27}$$

Using equations (3.22) and (3.27), equation (3.18) can be written as

$$\left[\frac{1}{3} + \frac{2}{3}\frac{d_s}{d_n}\right] = \frac{1}{3} + \frac{2}{3}\sqrt{\frac{2(a^2 + \frac{ac\sin^{-1}e}{e})}{4a^2}} \tag{3.28}$$

$$= \frac{1}{3} + \frac{2}{3}\sqrt{\frac{(1 + \frac{c\sin^{-1}e}{ae})}{2}} \tag{3.29}$$

Therefore,

$$K_n = \frac{1}{3} + \frac{2}{3}\sqrt{\frac{(1 + \frac{l_r\sin^{-1}e}{e})}{2}} \tag{3.30}$$

where $\frac{c}{a} = l_r > 1$.

Oblate spheroid

To calculate the diameter of a sphere, d_s, with the same total surface area as an oblate spheroid, the surface area of a sphere and an oblate spheroid are equated. This yields

$$4\pi\left(\frac{d_s}{2}\right)^2 = 2\pi a^2(1 + \frac{1-e^2}{e}\tanh^{-1}e) \tag{3.31}$$

$$\Rightarrow d_s = \sqrt{2a^2(1 + \frac{1-e^2}{e}\tanh^{-1}e)} \tag{3.32}$$

- When the oblate spheroid is projected perpendicular to its axis of rotation, the projection resembles an ellipse of major and minor axis, a and c. The value of d_n is the same as equation (3.24). The form factor is

$$K_n = \left[\frac{1}{3} + \frac{2d_s}{3d_n}\right] = \left[\frac{1}{3} + \frac{2\sqrt{2a^2(1 + \frac{1-e^2}{e}\tanh^{-1}e)}}{3\sqrt{4ac}}\right] \tag{3.33}$$

$$= \left[\frac{1}{3} + \frac{2}{3}\sqrt{\frac{a(1 + \frac{1-e^2}{e}\tanh^{-1}e)}{2c}}\right] \tag{3.34}$$

$$= \left[\frac{1}{3} + \frac{2}{3}\sqrt{\frac{(1 + \frac{1-e^2}{e}\tanh^{-1}e)}{2l_r}}\right] \text{where } \frac{c}{a} = l_r < 1 \tag{3.35}$$

- When the oblate spheroid is projected along its axis of rotation, the projection resembles a circle of radius a. The value of d_n is the same as equation (3.27). The form factor is

$$K_n = \left[\frac{1}{3} + \frac{2d_s}{3d_n}\right] = \left[\frac{1}{3} + \frac{2\sqrt{2a^2(1 + \frac{1-e^2}{e}\tanh^{-1}e)}}{3\sqrt{4a^2}}\right] \tag{3.36}$$

$$= \left[\frac{1}{3} + \frac{2}{3}\sqrt{\frac{(1 + \frac{1-e^2}{e}\tanh^{-1}e)}{2}}\right] \tag{3.37}$$

3.9.1.3 *Form factor in Loth*

Prolate spheroid

The form factors denoted by equations (3.38) and (3.39)), both of which are considered in Loth [66], are available since Oberbeck (1876) and Gans (1911) and have been cited in Kasper (1985) [68].
In the case of a prolate spheroid, the aspect ratio is given as $l_r = c/a > 1$ where a is the minor axis and c is the major axis. Here, $f_{||}$ and $f_{\perp}$ indicate the drag experienced by a spheroid while moving parallel or perpendicular to the flow. The values of $f_{||}$ and $f_{\perp}$ from Loth [66] are,

$$f_{||} \text{ exact } (l_r > 1) = \frac{(4/3) l_r^{-1/3}(1 - l_r^2)}{l_r - \frac{(2l_r^2-1)\log(l_r+\sqrt{l_r^2-1})}{\sqrt{l_r^2-1}}} \tag{3.38}$$

$$f_{\perp} \text{ exact } (l_r > 1) = \frac{(8/3) l_r^{-1/3}(l_r^2 - 1)}{l_r + \frac{(2l_r^2-3)\log(l_r+\sqrt{l_r^2-1})}{\sqrt{l_r^2-1}}} \tag{3.39}$$

$$f_{||} \text{ approx } (6 > l_r > 1) = \left(\frac{4}{5} + \frac{l_r}{5}\right) l_r^{-1/3} \tag{3.40}$$

$$f_{\perp} \text{ approx } (6 > l_r > 1) = \left(\frac{3}{5} + \frac{2l_r}{5}\right) l_r^{-1/3} \tag{3.41}$$

Oblate spheroid

In the case of an oblate spheroid, the aspect ratio can be given as $l_r = c/a < 1$. The values of $f_{||}$ and $f_{\perp}$ from Loth [66] are,

$$f_{||} \text{ exact } (l_r < 1) = \frac{(4/3) l_r^{-1/3}(1 - l_r^2)}{l_r + \frac{(1-2l_r^2)\cos^{-1} l_r}{\sqrt{1-l_r^2}}} \tag{3.42}$$

$$f_{\perp} \text{ exact } (l_r < 1) = \frac{(8/3) l_r^{-1/3}(l_r^2 - 1)}{l_r - \frac{(3-2l_r^2)\cos^{-1} l_r}{\sqrt{1-l_r^2}}} \tag{3.43}$$

For an oblate spheroid, when $(6 < l_r < 1)$, the expressions for $f_{||}$ approx and $f_{\perp}$ approx are the same as that of the prolate spheroid, denoted in equations (3.40) and (3.41) respectively.

3.9.1.4 *Agreement of the K_n with $f_{\perp}$*

In the prolate spheroid, the value of K_n in equation (3.30) does not match with $f_{\perp}$ in equation (3.39). However, if a factor of $l_r^{1/6}$ is included in equation (3.39), agreement is achieved for small values of l_r. Similarly, agreement is obtained, if a factor of $l_r^{-1/6}$ is included in equation (3.30), as shown in Figure 3.7a. In Figures 3.7a and 3.7b agreement between the various expressions is obtained only in the small values of l_r *i.e.* when the value of l_r is near unity. Thus

$$f_{\perp} = l_r^{-1/6} K_n \tag{3.44}$$

Figure 3.7b shows that agreement is obtained in the case of oblate spheroid, when the value of l_r is near unity. As expected, Figures 3.7a and 3.7b show that all form factors converge to unity as the

aspect ratio approaches unity. This is expected as $l_r = 1$ is the value of circle.

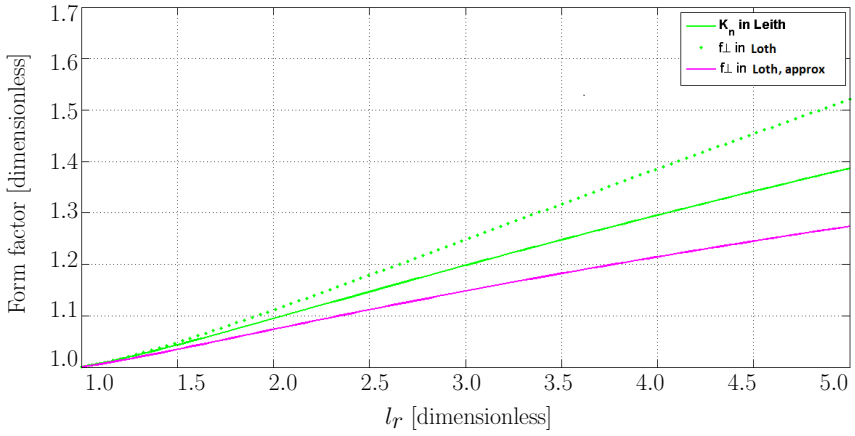

(a) Plot of $f_\perp$ exact, $f_\perp$ approx and $K_n l_r^{(-1/6)}$ as in equations (3.30), (3.39) and (3.41).

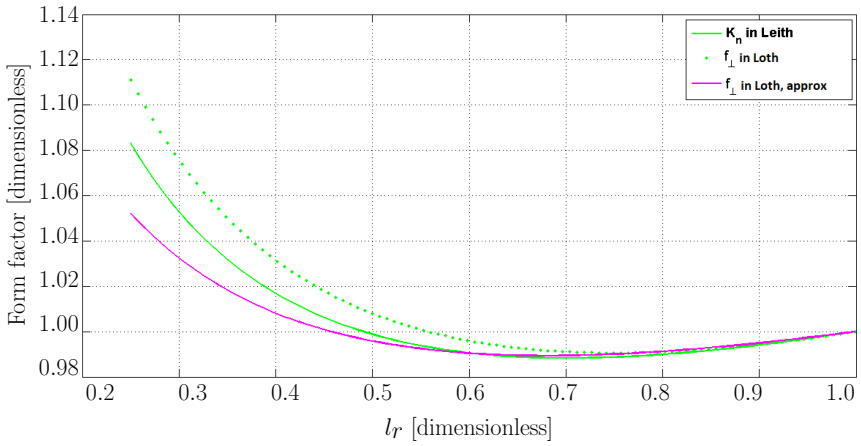

(b) Plot of $f_\perp$ exact, $f_\perp$ approx and $K_n l_r^{(-1/6)}$ as in equations (3.37), (3.41) and (3.43).

Figure 3.7: Plot of $K_n l_r^{(-1/6)}$ with respect to l_r.

When the value of l_r is near unity, agreement is obtained between $f_{||}$ and K_n for both prolate and oblate spheroids. This is because in Leith [67]

$$K = K_n \frac{d_n}{d_V} \tag{3.45}$$

where K is the Stokes correction factor using the volume equivalent diameter, d_V, and K_n is the Stokes correction factor based on the surface equivalent diameter. The term d_V can be defined as the diameter of a sphere with the same volume as that of the prolate/oblate spheroid. The term, d_n gives the projection equivalence, in terms of the area. In both oblate and prolate spheroid, $l_r = c/a$ and thus d_n can be expressed as

$$d_n^2 = 4ac = 4a^2 l_r \tag{3.46}$$

Here d_V denotes the volume conservation equivalence

$$d_V^3 = 8a^2 c = 8a^3 l_r \tag{3.47}$$

$$\frac{d_n}{d_V} = \frac{l_r^{1/2}}{l_r^{1/3}} = l_r^{1/6} \tag{3.48}$$

From equation (3.45), it can be concluded that the agreement should be obtained when $K = K_n l_r^{1/6}$. Therefore, the correct form of Stokes correction factor with the correct form of volume equivalent radius is

$$F_d = 3\pi\mu V d_V K \tag{3.49}$$

$$\Leftrightarrow F_d = 3\pi\mu V d_n K_n \tag{3.50}$$

3.9.2 Comparison with the graphs of Riegler et al.

Figure 3.8a indicates the effect of change of l_r on targeting efficiency. As the number of cells aggregated was not given, in order to match the obtained results with the plot when $l_r = 1$, different values of aggregates are considered in Figure 3.8b. Aggregation of 80 cells, including the factor b, appears to be the closest approximation of Figure 3.8a, when $l_r = 1$.

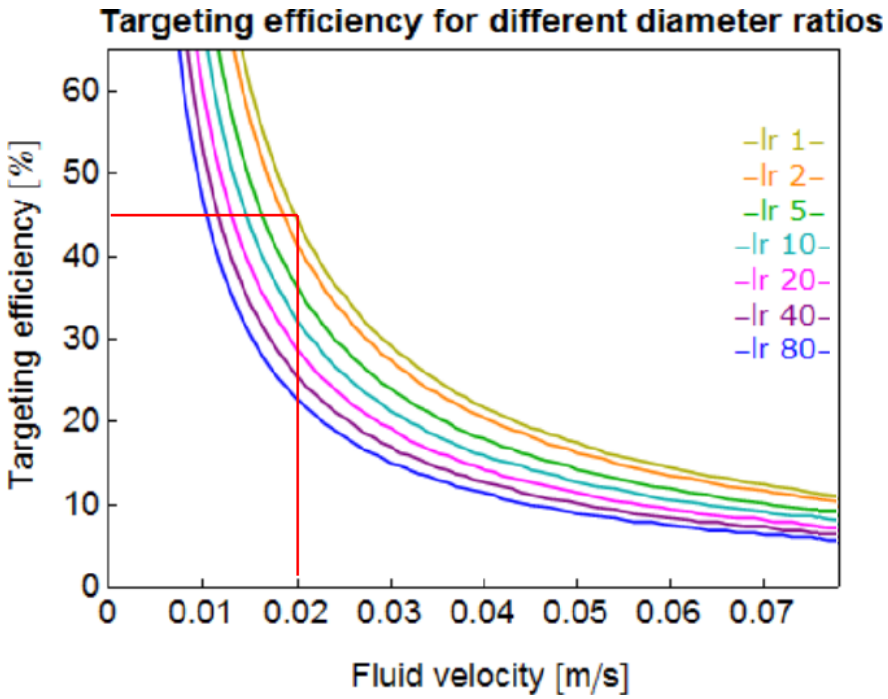

(a) Targeting efficiency with respect to v_f taken directly from Riegler *et al.* [11] for different values of l_r.

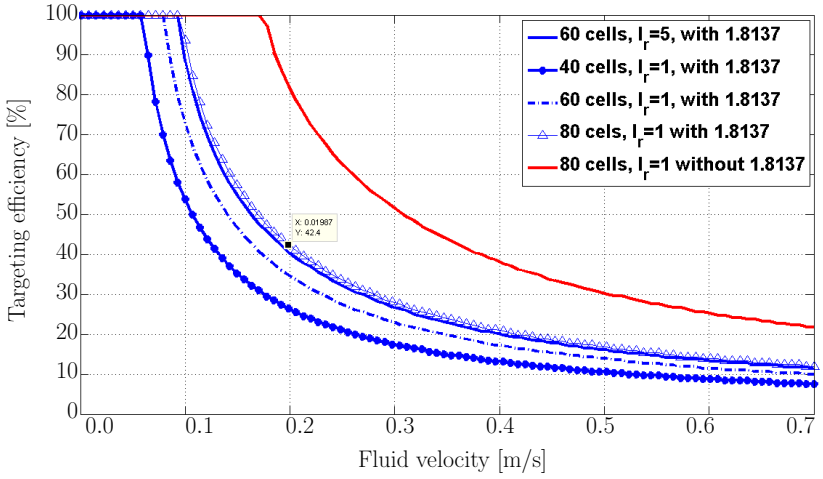

(b) Targeting efficiency with respect to v_f obtained by our calculations when $l_r = 1$.

Figure 3.8: Targeting efficiency with respect to fluid velocity.

3.10 Targeting efficiency for prolate and oblate spheroids

3.10.1 Prolate spheroid

- The drag experienced by a prolate spheroid while moving along its major axis will be less than the drag experienced by an equivalent sphere. Hence, the targeting efficiency of a prolate spheroid should increase. The green line in Figure 3.9 uses $f_{||}$ in equation (3.38) to calculate the targeting efficiency.

- The drag experienced by a prolate spheroid while moving along its minor axis will be more than that of an equivalent sphere. Hence, the targeting efficiency of a prolate spheroid should decrease. The black and red lines in Figure 3.9 represent the targeting efficiency, calculated by using $f_{\perp}$ as mentioned in equations (3.20) and (3.39) respectively.

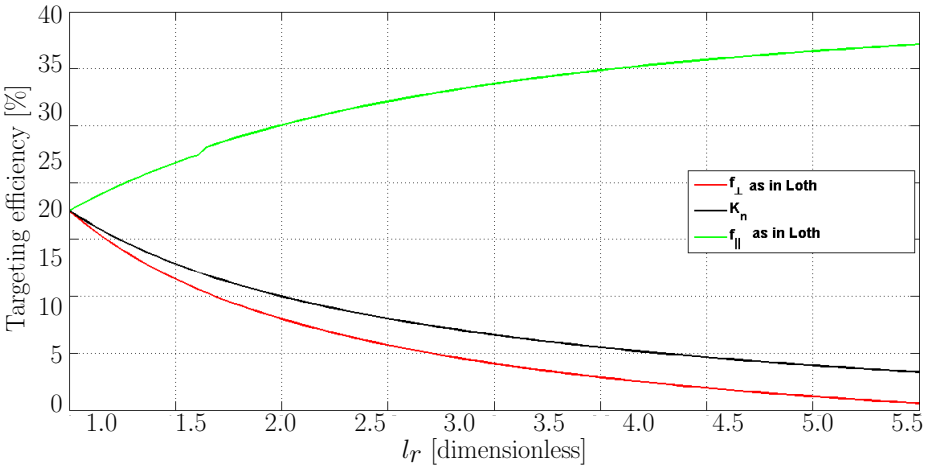

Figure 3.9: Targeting efficiency with respect to l_r when $v_f = 5 \times 10^{-2}$ m/s in different values of form factors as given by equations (3.20), (3.38) and (3.39).

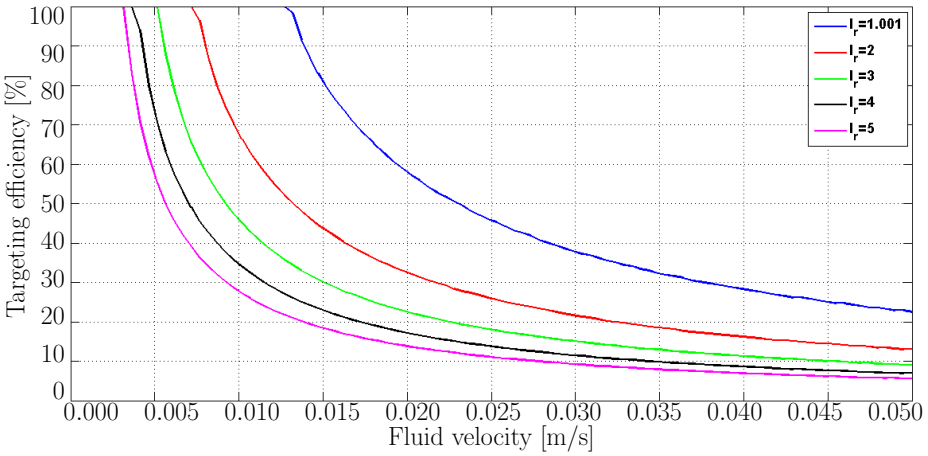

Figure 3.10: Targeting efficiency with respect to v_f in different values of l_r when the form factor is taken as $f_{\perp}$ from equation (3.39).

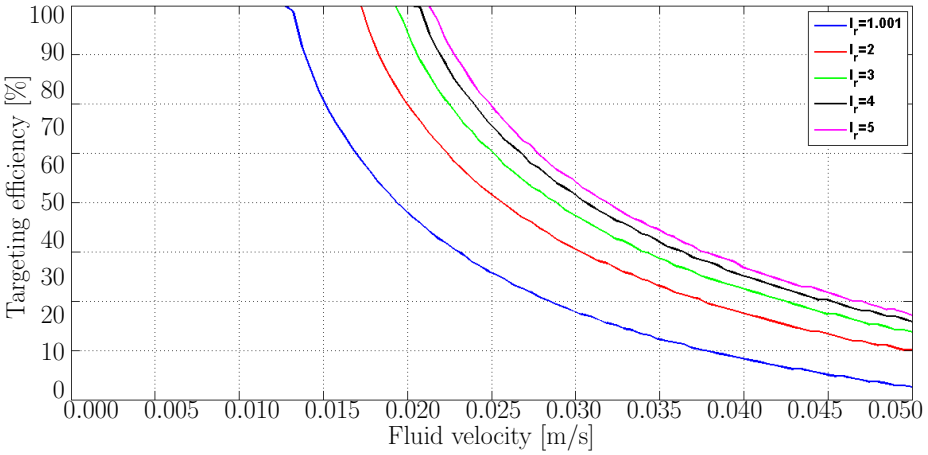

Figure 3.11: Targeting efficiency with respect to v_f in different values of l_r when the form factor is considered to be $f_{||}$ in equation (3.38).

3.10.2 Oblate spheroid

- The drag experienced by an oblate spheroid, while moving along the minor axis, is more than that of a sphere. Thus its targeting efficiency is less than a sphere.

- When an oblate spheroid moves along the major axis, the drag experienced is less than that of a sphere. The targeting efficiency increases monotonically.
  Zhou *et al.* [69], mention that oblate particles experience less drag than a volume equivalent sphere while moving along minor axis while prolate particles experience less drag while moving along their major axis. This increases the targeting efficiency of prolate and oblate spheroids as l_r changes with respect to a sphere of $l_r = 1$, as shown in Figures 3.11 and 3.13b.

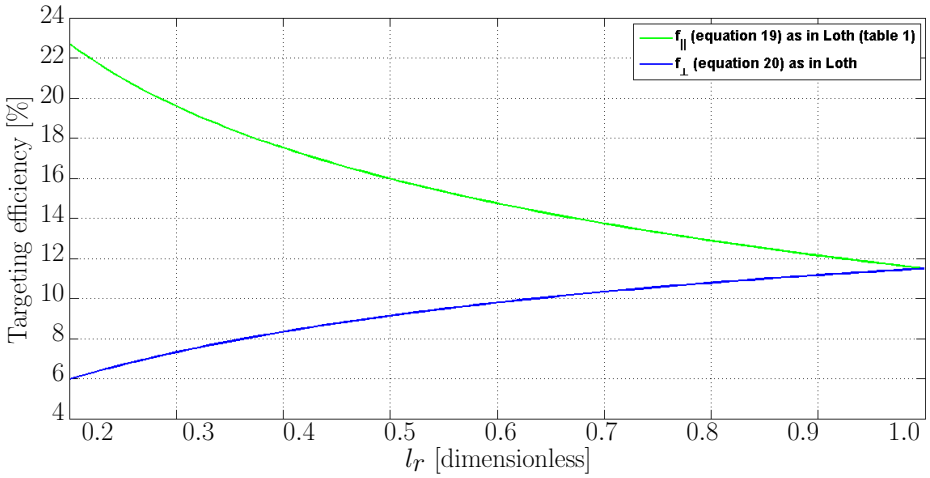

Figure 3.12: Targeting efficiency with respect to l_r in oblate spheroid for different values of form factors as denoted by equations (3.42) and (3.43).

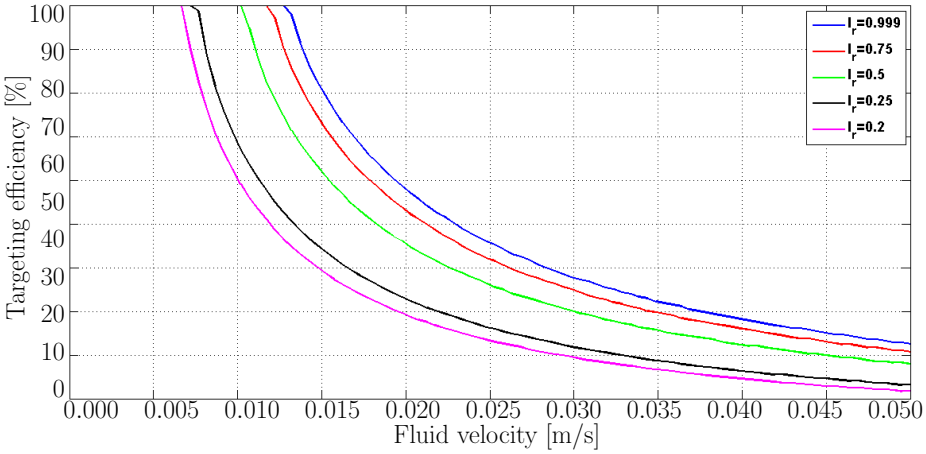

(a) Targeting efficiency with respect to v_f for different values of l_r when the form factor is considered to be $f_{\perp}$ as in equation (3.43).

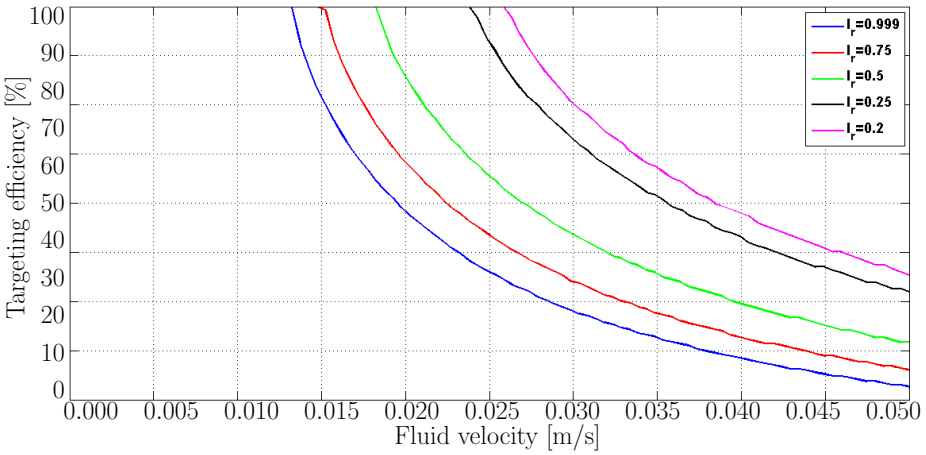

(b) Targeting efficiency with respect to v_f for different values of l_r when the form factor is considered to be $f_{||}$ as in equation (3.42).

Figure 3.13: Targeting efficiency of an oblate spheroid

From Figures 3.10, 3.11, 3.13a and 3.13b it can be concluded that, for a given range of fluid velocities, $\mathbf{v}_f$, the targeting efficiency of non spherical particles, both prolate and oblate spheroids, can be greatly increased given the optimum value of aspect ratio, l_r. As mentioned in [70], the non-spherical particles are advantageous to improve drug delivery efficiency compared with spherical ones, because of the increased drug loading efficiency and larger surface area which leads to enhanced attachment to a vascular wall.

3.11 Conclusion

Riegler *et al.* have mentioned the importance of magnetic interaction multiple times and attributed their experimental and theoretical discrepancies to the neglect of magnetic interaction in their model. The models of Riegler *et al.* [11, 12] have been referred to by multiple authors, resulting in over 150 citations. Therefore, it was assumed to be a good starting point to build modelling skills in order to model multi-particle interactions as presented in chapter 6.

In this chapter, numerical models of three research articles of Riegler *et al.* are presented. While replicating their models and validating the results, different modelling errors were found and corrected. In order to identify the source of errors, a thorough literature review of the derivation of form factors

for various shapes is presented. It is found that along with the fluid velocity, the shape of MNPs plays a vital role in determining the targeting efficiency.

Chapter 4

Mathematical modelling for trajectories of magnetic nanoparticles

Sharma et al. presented a mathematical model for a cluster of MNPs inside a blood vessel under the influence of an external permanent magnet. Buoyancy was included in their model but it was not explored. In this chapter, the numerical model of Sharma et al. is investigated and replicated. Our results show that the effect of buoyancy can be neglected.

4.1 Additional list of symbols

- $\mathbf{H}$, magnetic field ..... T[1]
- H_x, component of magnetic field along the x-axis ..... T
- H_z, component of magnetic field along the z-axis ..... T
- R_m, radius of the external magnet ..... m
- ρ_f, density of blood ..... $\mathrm{kg\,m^{-3}}$
- ρ_p, density of the MNP ..... $\mathrm{kg\,m^{-3}}$
- g, acceleration due to gravity ..... $\mathrm{m\,s^{-2}}$
- d_m, distance of the MNP from the centre of the magnet ..... cm
- χ, magnetic susceptibility of the MNP ..... dimensionless
- $F_{m,x}$, component of magnetic force along the x-axis ..... N
- $F_{m,z}$, component of magnetic force along the z-axis ..... N
- $v_{p,x}$, component of velocity of the MNP along the x-axis ..... $\mathrm{m\,s^{-1}}$
- $v_{p,z}$, component of velocity of the MNP along the z-axis ..... $\mathrm{m\,s^{-1}}$

[1]Following Sharma *et al.*, only in this chapter the symbol for magnetic field is taken as $\mathbf{H}$ and not $\mathbf{B}$. Alternative unit of magnetic field used in this chapter is Gauss (the CGS unit of magnetic field). One Gauss is equivalent to 1×10^{-4} Tesla. This was done in order to keep the analytic expressions consistent to trace the errors.

Table 4.1: List of parameters values for chapter 4.

Parmeter	Description	Value
R	radius of the particle	300×10^{-9} m
M_s	magnetisation of the external magnet	$10^6 \mathrm{A\,m^{-1}}$
R_v	radius of the blood vessel	75×10^{-6} m
R_m	radius of the external magnet	2×10^{-2} m
η	blood viscosity	$3.2 \times 10^{-3} \mathrm{kg\,m^{-1}\,s^{-1}}$
ρ_f	density of blood	$1060\ \mathrm{kg\,m^{-3}}$
ρ_p	density of the MNP	$5000\ \mathrm{kg\,m^{-3}}$
$\overline{v}_f$	average velocity of blood	$10 \times 10^{-3}\ \mathrm{m\,s^{-1}}$
g	acceleration due to gravity	$9.8\ \mathrm{m\,s^{-2}}$

4.2 Introduction

Sharma *et al.* [23] present a 2 dimensional mathematical model to describe the trajectories of MNPs in a blood vessel. The MNPs are injected into a blood vessel and captured at a particular site using a magnetic field, produced by a magnet positioned outside the vessel. The forces affecting the transport of MNPs in the model are the magnetic force, the drag force and the buoyancy force. The results show that when distance between the magnet and the vessel, $d_m \leq 2.5$ cm, the MNPs are captured before or at the centre of the magnet. However, as d_m increases, *i.e.* $d_m > 2.5$ cm, the MNPs flow down the vessel. Although buoyancy is included in the model of Sharma *et al.*, it was not explored. While implementing the model it was found that the effect of buoyancy is negligible and can be neglected. Some typographical and presentational errors were also found and corrected.

4.3 Physical geometry

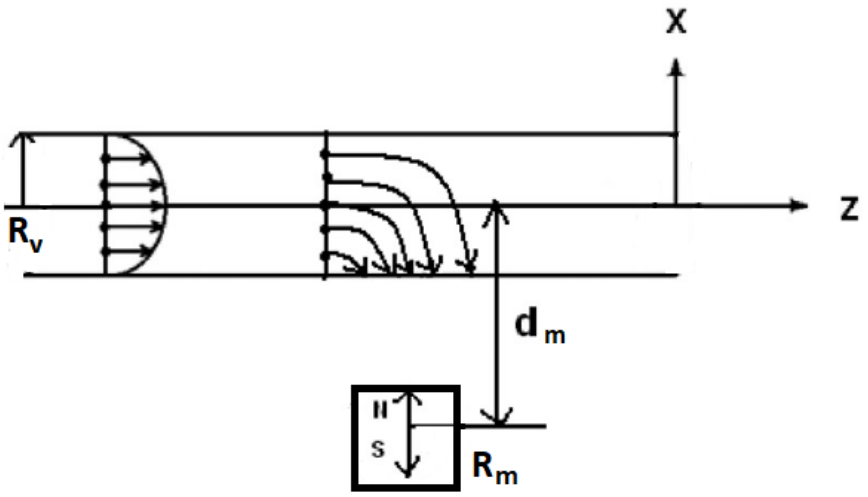

Figure 4.1: Diagram of MNPs in a blood vessel similar to as shown from Sharma *et al.* [23]. The magnet is positioned outside the vessel.

4.4 Equations and respective figures

4.4.1 Generating the components of the magnetic field, H

The components of magnetic field for an infinite magnet, magnetised perpendicular to its axis, can be represented inside the blood vessel as,

$$H_x(x,z) = \frac{M_s R_m^2}{2} \frac{[(x+d_m)^2 - z^2]}{[(x+d_m)^2 + z^2]^2} \tag{4.1}$$

and

$$H_z(x,z) = \frac{M_s R_m^2}{2} \frac{2(x+d_m)z}{[(x+d_m)^2 + z^2]^2} \tag{4.2}$$

where, M_s is magnetisation of the magnet, R_m is radius of the external magnet, H_x and H_z are the components of **H**. In generating Figure 4.2b, the values given in Sharma *et al.* are $d_m = 2.5$ cm and $-3R_m \leq z \leq 3R_m$. The x-component is said to be along the axis of the blood vessel, so $x = 0$. In Figure 4.2c, the z values are changed to $-3d_m \leq z \leq 3d_m$.

Figure 4.2a is the published graph of Sharma *et al.* Using the parameters in Sharma *et al.*, Figure 4.2b is produced. However, if instead of z/R_m, z/d_m is used in the x-axis, the result (Figure 4.2c) is closer to that of Figure 4.2a. This is most likely a typographical/presentational error in Sharma *et al.*, where instead of z/d_m, z/R_m is published.

From Figure 4.2c it can be said that the maximum value obtained by the vertical component $H_x = 4000$ G is at the centre of the magnet, where $z/R_m = 0$. The horizontal component, H_z, oscillates around the central axis of the blood vessel and peaks towards the edges of magnet, where $z/R_m \pm 1$. It is to be noted that the horizontal axis of Figure 4.2c is different from Figures 4.2a and 4.2b. This is done in an effort to match the obtained graphs with the published result.

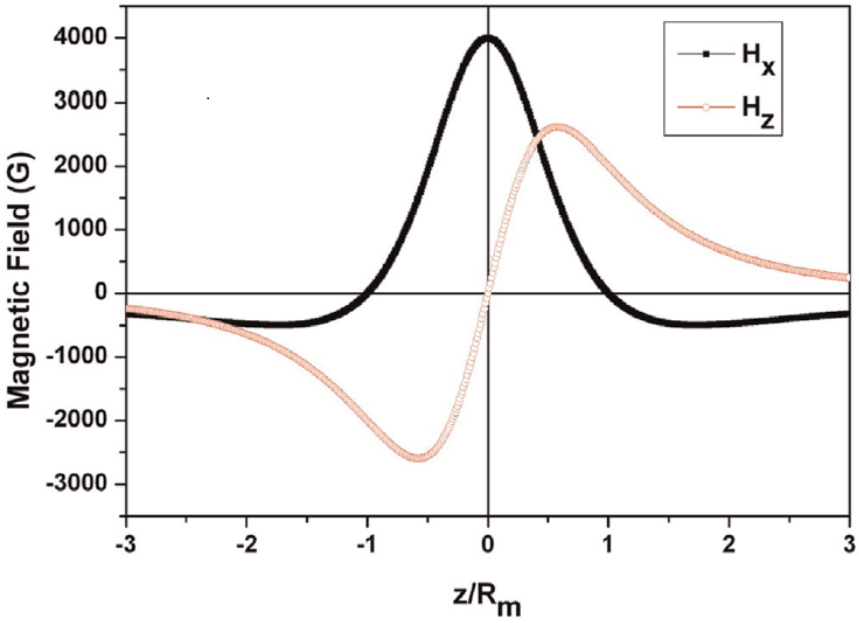

(a) Simulated result taken directly from Sharma *et al.* [23].

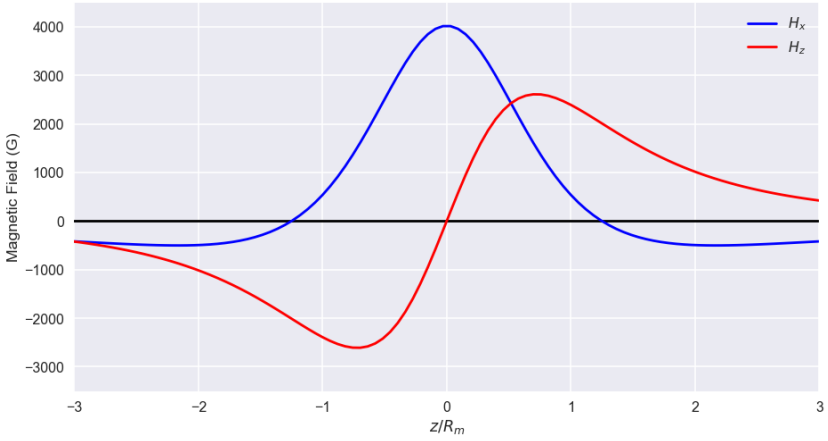

(b) Calculated values of components of **H**, with respect to z/R_m.

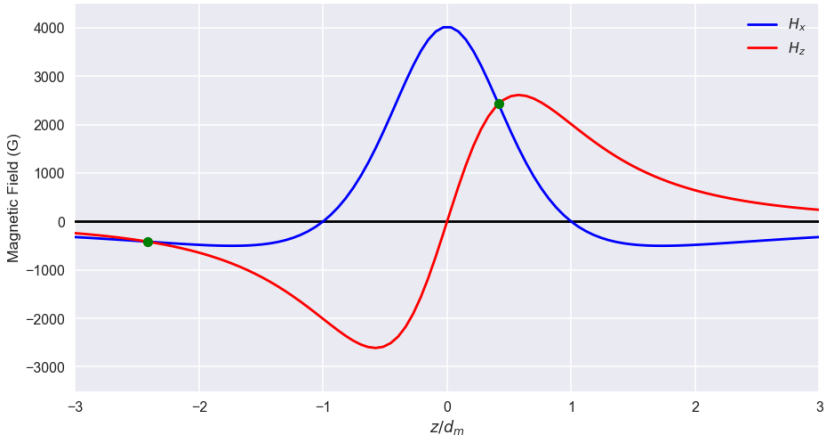

(c) Calculated values of components of **H**, with respect to z/d_m.

Figure 4.2: Vertical (H_x) and horizontal (H_z) components of magnetic field.

4.4.2 Generating the components of the magnetic force, $\boldsymbol{F}_m$

The components of $\mathbf{F}_m$ are given by

$$F_{m,x} = \mu_0 V \frac{3\chi}{\chi+3}\left[H_x\frac{\partial H_x}{\partial x} + H_z\frac{\partial H_x}{\partial z}\right] \tag{4.3}$$

$$F_{m,z} = \mu_0 V \frac{3\chi}{\chi+3}\left[H_x\frac{\partial H_z}{\partial x} + H_z\frac{\partial H_z}{\partial z}\right] \tag{4.4}$$

where the partial components of $\mathbf{H}$ are given as

$$\frac{\partial H_x}{\partial x} = -M_s R_m^2 \frac{(x+d_m)[(x+d_m)^2 - 3z^2]}{[(x+d_m)^2+z^2]^3} \tag{4.5}$$

$$\frac{\partial H_z}{\partial x} = M_s R_m^2 \frac{z[z^2 - 3(x+d_m)^2]}{[(x+d_m)^2+z^2]^3} \tag{4.6}$$

$$\frac{\partial H_x}{\partial z} = -M_s R_m^2 \frac{z[3(x+d_m)^2 - z^2]}{[(x+d_m)^2+z^2]^3} \tag{4.7}$$

$$\frac{\partial H_z}{\partial z} = M_s R_m^2 \frac{(x+d_m)[(x+d_m)^2 - 3z^2]}{[(x+d_m)^2+z^2]^3} \tag{4.8}$$

Equations (4.3) and (4.4) reduce to

$$F_{m,x} = -3\mu_0 V M_s^2 R_m^4 \frac{d_m}{2[d_m^2+z^2]^3} \tag{4.9}$$

$$F_{m,z} = -3\mu_0 V M_s^2 R_m^4 \frac{z}{2[d_m^2+z^2]^3} \tag{4.10}$$

where μ_0 is the permeability of vacuum and V is the volume of the particle.
Figure 4.3a cannot be correctly replicated using the given values in Sharma *et al.* (Figure 4.3b). In Figure 4.3c, the x-axis is set to z/d_m instead of z/R_m, which brings Figure 4.3c closer to Figure 4.3a. Once again, this is most likely another typographical/presentational error in Sharma *et al.* where instead of z/d_m, z/R_m is published.

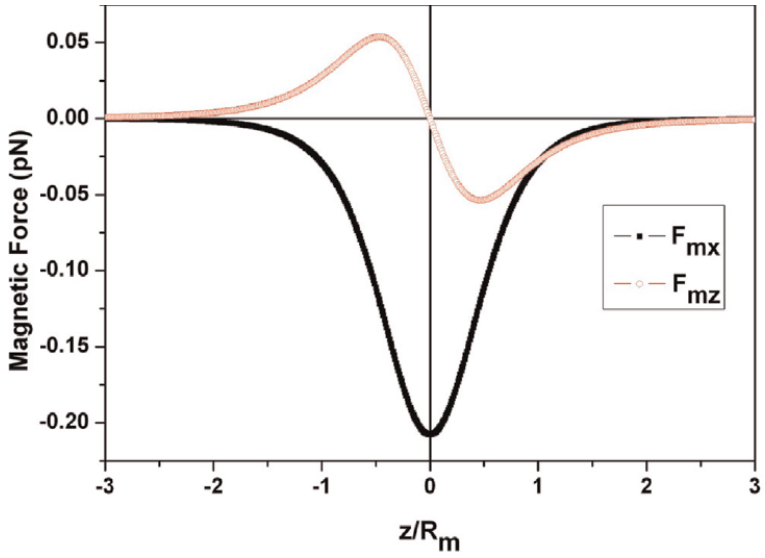

(a) Vertical ($F_{m,x}$) and horizontal ($F_{m,z}$) components of magnetic field taken directly from Sharma *et al.*

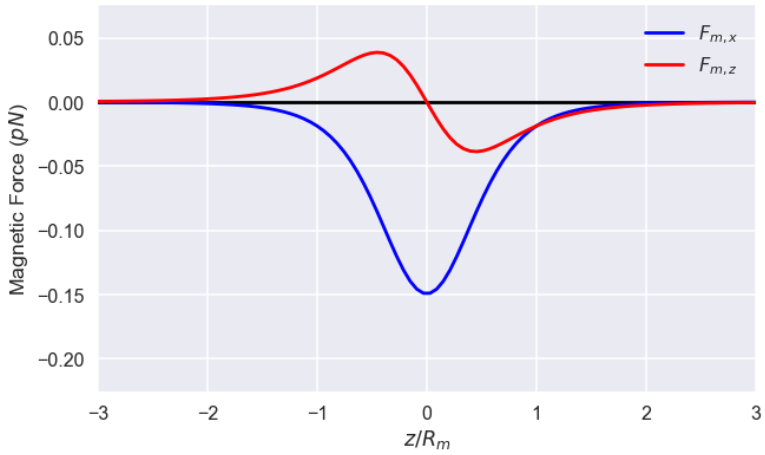

(b) Calculated values of the vertical ($F_{m,x}$) and horizontal ($F_{m,z}$) components of magnetic field with respect to z/R_m.

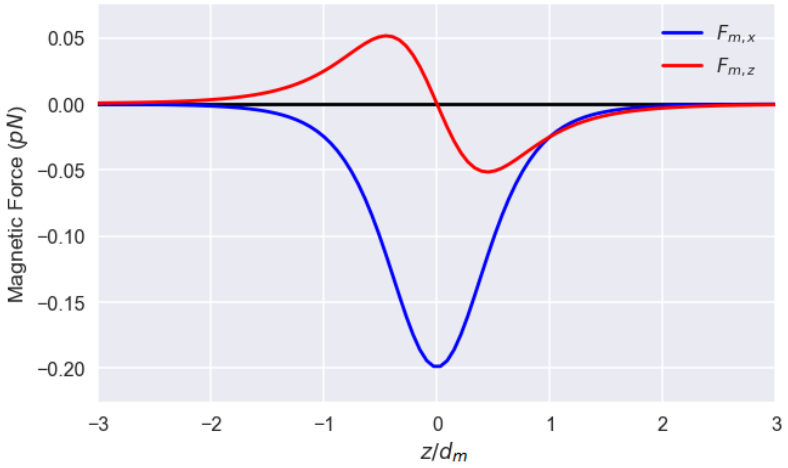

(c) Calculated values of the vertical ($F_{m,x}$) and horizontal ($F_{m,z}$) components of magnetic field with respect to z/d_m.

Figure 4.3: Values of the vertical and horizontal components of magnetic force with respect to z/d_m.

Similar to Figure 4.2, it is to be noted that the horizontal axis of Figure 4.3c is different from Figures 4.3a and 4.3b. This is done in an effort to match the obtained graphs with the published result.

In [23] and as evident from Figures 4.3a to 4.3c, it is observed that the horizontal component of the magnetic force, ($F_{m,z}$), shows similar profile as the horizontal component of magnetic field (H_z) in the opposite direction. Therefore, $F_{m,z}$ oscillates around the central axis of the blood vessel and shows the maximum value towards the edges of magnet, where $z/R_m \pm 1$. Consequently, as the MNP travels horizontally above the magnet from left to right, it accelerates till it reaches the centre of the magnet and then decelerates. As a result, $F_{m,z}$ is responsible for the oscillatory movement of the MNP within the blood vessel. The vertical component of magnetic force ($F_{m,x}$) is strongest at the centre of the magnet, where $z/R_m = 0$ and its strength decreases as towards edges of the magnet, where $z/R_m \pm 1$. At the centre of the magnet, the value of $|F_{m,x}| = 0.20$ pN. This force targets the MNP towards the magnet.

4.4.3 Generating the trajectories of the magnetic nanoparticles

The equations of motion of the MNPs along the x- and z-axes, in parabolic flow, are given by

$$v_{p,x} = \frac{dx}{dt} = \frac{1}{3\eta}\mu_0 R^2 M_s^2 R_m^4 \frac{d_m}{(d_m^2 + z^2)^3} - \frac{2}{9\eta} R^2(\rho_p - \rho_f)g \tag{4.11}$$

$$v_{p,z} = \frac{dz}{dt} = \frac{1}{3\eta}\mu_0 R^2 M_s^2 R_m^4 \frac{z}{(d_m^2 + z^2)^3} + 2\overline{v}_f \left[1 - \left(\frac{x}{R_v}\right)^2\right] \tag{4.12}$$

where η is the blood viscosity, R is the radius of the particle, ρ_p is density of the particle, ρ_f is density of blood and g is acceleration due to gravity. The initial position along the x-axis is varied.
Equations (4.11) and (4.12) are solved using ode45 (adaptive Runge-Kutta method) and odeint (integration method). Figure 4.4 shows the trajectories of the MNPs over time, when $d_m = 2.5$ cm. Figure 4.4a shows the published result of Sharma *et al.* Using all the parameters as given in Sharma *et al.*, Figure 4.4b is obtained. Figures 4.4a and 4.4b are qualitatively and quantitatively different. In Figure 4.4a, the trajectory of the MNP beginning at $x/R_v = 1$, shows a pattern which is expected in a parabolic flow. Keeping all the other parameters constant, Figure 4.4c uses rectangular flow. Figure 4.4c is qualitatively and quantitatively similar to Figure 4.4a. This most likely is a presentational/modelling error in Sharma *et al.*

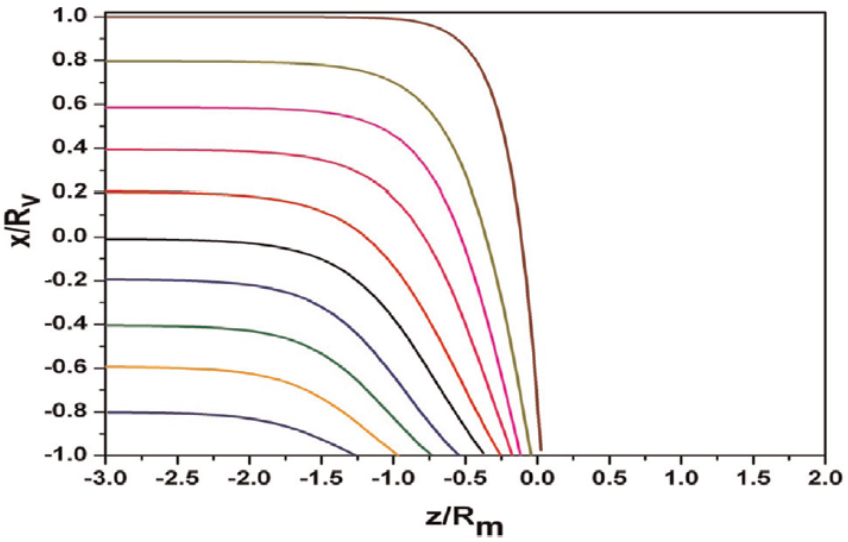

(a) Simulated result taken directly from Sharma *et al.* [23].

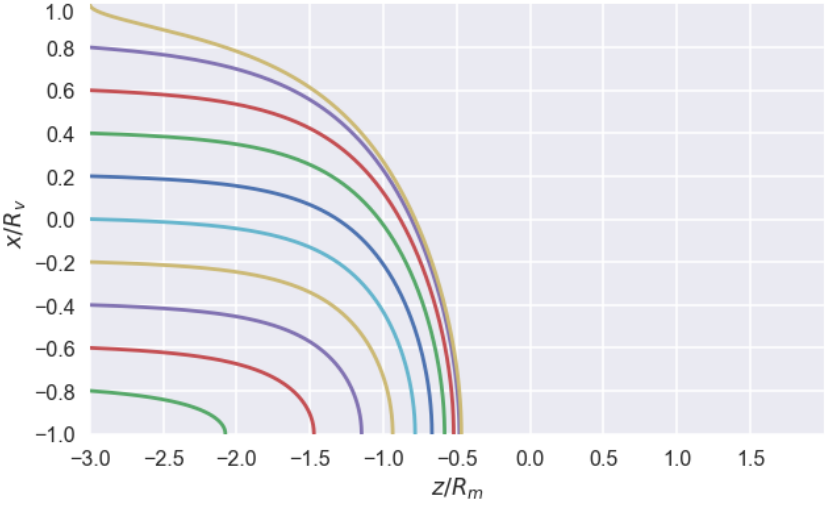

(b) Calculated trajectories at various initial positions along x-axis.

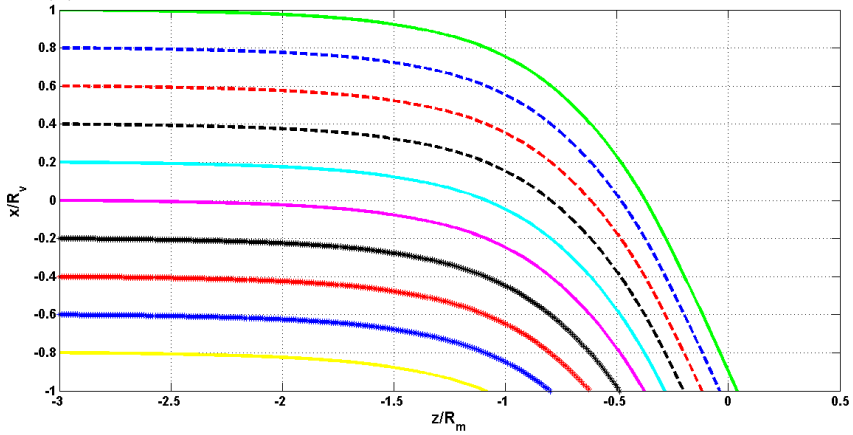

(c) Calculated trajectories at various initial positions along x-axis in a rectangular flow.

Figure 4.4: Calculated trajectories at various initial positions along x-axis when $d_m = 2.5$ cm.

From Figures 4.4a to 4.4c it can be said that the conclusion drawn in Sharma *et al.* that all the MNPs are captured either before or at the centre of the magnet is incorrect, unless the MNPs are in a rectangular flow.

Figure 4.5 shows the effect of d_m on the trajectories of the MNPs starting from a fixed location. Fig-

ure 4.5a shows the published result in Sharma *et al.* and Figure 4.5b shows the calculated result.

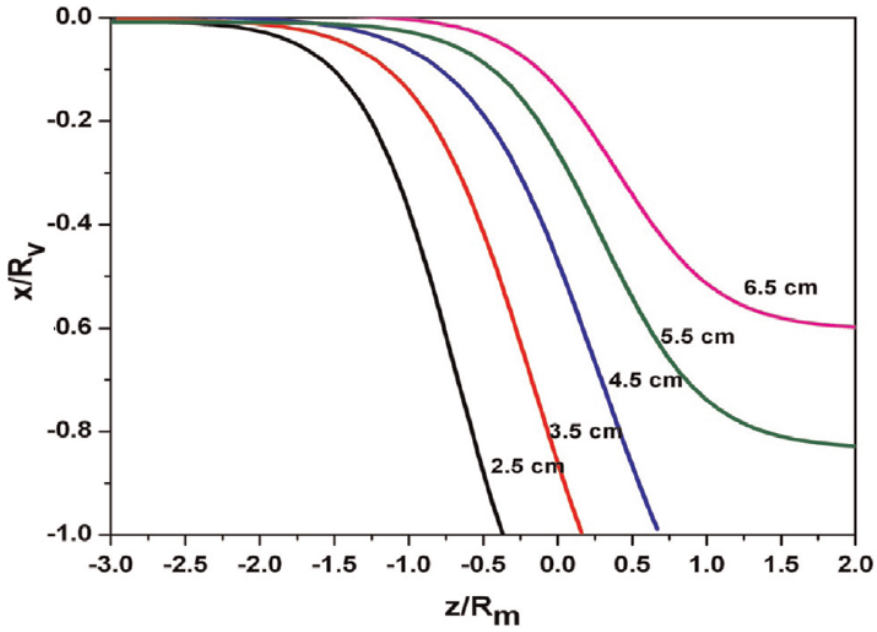

(a) Simulated result taken directly from Sharma *et al.* [23].

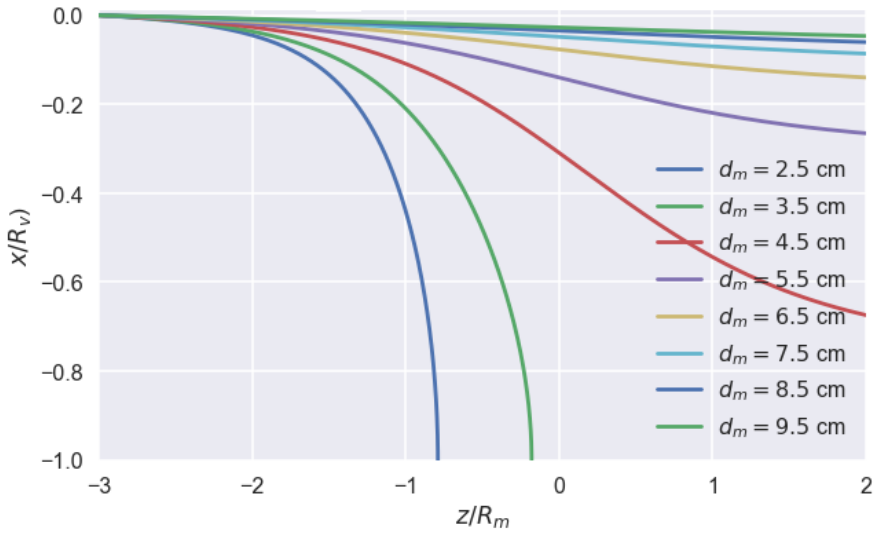

(b) Calculated trajectories at various initial positions along the x-axis.

Figure 4.5: Calculated trajectories at various initial positions along the x-axis for different values of d_m.

In Sharma *et al.*, it was concluded that all the MNPS at the centre of blood vessel are captured by the magnet when the distance between the centres of the blood vessel and the magnet is up to 4.5 cm, as given in Figure 4.5a. However, the replicated calculations, as displayed in Figure 4.5, show that the MNPs are captured by the magnet when the distance between the centres of the blood vessel and the magnet, $d_m \leq 3.5$ cm.

4.5 Conclusion

The numerical model in Sharma *et al.* has been cited over 55 times. Therefore, the model in Sharma *et al.* was implemented in order to develop modelling skills. A number of numerical errors were found and corrected. Several graphs generated show significant deviation from the published results. These

are presented for comparison. In order to trace the source of errors, the references in Sharma *et al.* have been investigated.

Chapter 5

Mathematical modelling of the motion of two microrobots

Mellal et al. analysed the motion of two microrobots in a microfluidic channel. In this chapter, the theoretical formulations of magnetic interactions as given in Mellal et al. are reviewed and ab initio calculations to predict the behaviour of two microrobots have been performed.

5.1 Additional list of symbols

- $R^{(i)}$, radius of the i^{th} MNP ..... m
- $V^{(i)}$, volume of the i^{th} MNP ..... m^3
- $\mathbf{m}^{(i)}$, magnetic moment of the i^{th} MNP ..... $\mathrm{A\,m}^2$
- $\mathbf{p}^{(i)}$, position of the i^{th} MNP ..... m
- $d^{(i,j)} = |\mathbf{p}^{(i)} - \mathbf{p}^{(j)}|$, distance between the centres of the i^{th} and the j^{th} MNP ..... m
- $\hat{\mathbf{d}}^{(i,j)} = \frac{\mathbf{p}^{(i)} - \mathbf{p}^{(j)}}{d^{(i,j)}}$, unit vector along the line of MNP centres from i^{th} to j^{th} ..... dimensionless
- d_R, relative distance in terms of R, ... dimensionless
- $\mathbf{v}^{(i)}$, velocity of the i^{th} microrobot ..... $\mathrm{m\,s}^{-1}$
- $\mathbf{F}_m^{(i)}$, magnetic force experienced by the i^{th} MNP ..... N
- $\mathbf{F}_d^{(i)}$, drag force experienced by the i^{th} MNP ..... N
- $\mathbf{F}_{\mathrm{int}}^{(i)}$, dipolar interaction force experienced by the i^{th} MNP ..... N
- l_r, aspect ratio ..... dimensionless
- $k^{(i)}$, Stokes correction factor of the i^{th} microrobot ..... dimensionless

Table 5.1: List of parameters values for chapter 5.

Parmeter	Description	Value
μ_0	the permeability of free space	$4\pi \times 10^{-7}\ \mathrm{T\,m\,A}^{-1}$
$\mathbf{B}$	magnetic field	$30\,\mathrm{mT}$
M_s	saturation magnetisation	$1.23 \times 10^6 \mathrm{A\,m}^{-1}$
η	fluid viscosity	$4 \times 10^{-3} \mathrm{kg\,m}^{-1}\,\mathrm{s}^{-1}$
$R^{(1)}$	radius of the 1st microrobot	$500\,\mu\mathrm{m}$
$R^{(2)}$	radius of the 2nd microrobot	$250\,\mu\mathrm{m}$
$\frac{\partial B_z}{\partial x}$	magnetic gradient	$0.05\,\mathrm{T\,m}^{-1}$

5.2 Introduction

The magnetic microrobot is a colloidal suspension of superparamagnetic iron oxide (SPIO) particles. Microrobots offer a number of prospective applications such as performing precise tasks inside the human body, for instance providing a mobile viewing platform enhancing a surgeon's view [20]. Mellal *et al.* [19], conducted experiments to investigate the motion of two different sized microrobots in a microfluidic channel. Mellal *et al.* described the theoretical formulations of the magnetic dipolar interaction forces between two microrobots in a microfluidic environment under an uniform magnetic field. The paper showed experimental magnetic interaction forces to be in the order of micronewtons. Using the methods employed in the past by Cregg *et al.* to model the effect of interactions on aggregation of magnetic particles [26, 71–73], this chapter presents an extension of the model of Mellal *et al.* [19] to 3D.

5.3 The mathematical model

5.3.1 The physical geometry

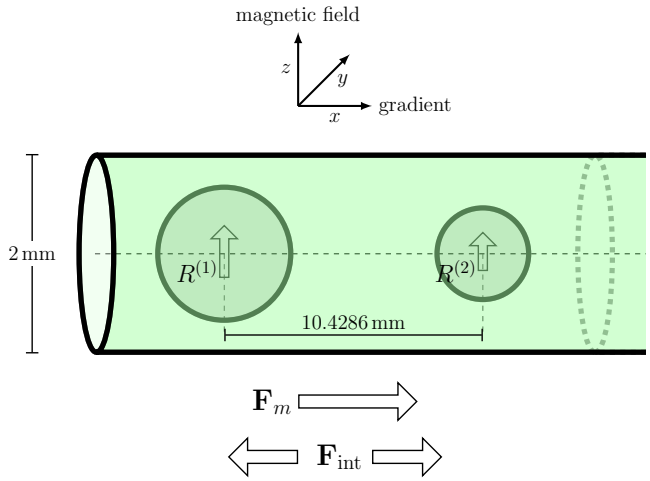

Figure 5.1: Schematic drawing of the experimental setup. The magnetic field, **B**, is directed along the z-axis. The magnetic gradient is along the x-axis.

5.3.2 Model assumptions

1. It is assumed that the two microrobots do not make contact with the tube wall.
2. The background magnetic field, along the z-axis, is strong enough to align both the microrobots in the same direction.
3. The centres of both microrobots are along a line parallel to the x-axis.
4. The magnetic interaction force continues to act along a line parallel to the x-axis till the end of the simulations.
5. The microrobots are spherical and are placed in a cylindrical tube.
6. Throughout the simulation the magnetisation of the microrobots is considered to be saturated.

5.3.3 Magnetic force

Two magnetic microrobots are placed in a microfluidic channel, positioned at $\mathbf{p}^{(i)} = (x^{(i)}, y^{(i)}, z^{(i)})^T$, where microrobot $i \in \{1, 2\}$. The magnetic gradient, perpendicular to the magnetic field $\mathbf{B}$, is along the x-axis. This gradient produces a magnetic force, $\mathbf{F}_m^{(i)}$, on the i^{th} microrobot,

$$\mathbf{F}_m^{(i)} = (\mathbf{m}^{(i)} \cdot \nabla)\mathbf{B} = V^{(i)}(\mathbf{M}_s \cdot \nabla)\mathbf{B} \tag{5.1}$$

where the magnetic moment, $\mathbf{m}^{(i)} = V^{(i)}\mathbf{M}_s$. Here $V^{(i)}$ is the volume of the i^{th} microrobot, $\mathbf{M}_s$ is the saturation magnetisation vector, and $\mathbf{B}$ is the background magnetic field. Here $\mathbf{M}_s = M_s\hat{\mathbf{m}}$, where M_s is the saturation magnetisation value of the material and $\hat{\mathbf{m}} = (m_x, m_y, m_z)$, is the unit vector along $\mathbf{B}$. Equation (5.1) can be re-written as

$$[F_{m,x}^{(i)}, F_{m,y}^{(i)}, F_{m,z}^{(i)}]^T = V^{(i)} M_s \begin{bmatrix} m_x \frac{\partial B_x}{\partial x} + m_y \frac{\partial B_x}{\partial y} + m_z \frac{\partial B_x}{\partial z} \\ m_x \frac{\partial B_y}{\partial x} + m_y \frac{\partial B_y}{\partial y} + m_z \frac{\partial B_y}{\partial z} \\ m_x \frac{\partial B_z}{\partial x} + m_y \frac{\partial B_z}{\partial y} + m_z \frac{\partial B_z}{\partial z} \end{bmatrix} \tag{5.2}$$

Since the magnetic moment is assumed to align with the background field $\mathbf{B}$, along the z-axis, it can be said that $m_x = m_y = 0$ and $m_z = 1$. Thus, equation (5.2) reduces to

$$[F_{m,x}^{(i)}, F_{m,y}^{(i)}, F_{m,z}^{(i)}]^T = V^{(i)} M_s \left[\frac{\partial B_x}{\partial z}, \quad \frac{\partial B_y}{\partial z}, \quad \frac{\partial B_z}{\partial z}\right]^T \tag{5.3}$$

Furthermore, the applied gradient is only along the x-axis, so that equation (5.3) reduces to

$$\mathbf{F}_m^{(i)} = V^{(i)} M_s \left[\frac{\partial B_x}{\partial z}, \quad 0, \quad 0\right]^T \tag{5.4}$$

Following Riegler *et al.* [11] for an ideal linear gradient it can be said that, $\frac{\partial B_x}{\partial z} = \frac{\partial B_z}{\partial x}$, as given in equation (12) in the model of Reigler *et al.* [11].

5.3.4 Stokes drag

The drag force experienced by the microrobots is expressed as [19]

$$\mathbf{F}_d^{(i)} = -6\pi\eta k^{(i)} R^{(i)} \mathbf{v}^{(i)} \tag{5.5}$$

where η is the fluid viscosity. The $k^{(i)}$ denotes the dimensionless Stokes correction factor for spheroids. For spheres $k^{(i)} = 1$. $R^{(i)}$ is the volume equivalent radius and $\mathbf{v}^{(i)}$ is the velocity of the i^{th} microrobot.

5.3.5 Magnetic interaction force

In presence of a magnetic field, the magnetic interaction force is given as [74]

$$\mathbf{F}_{\text{int}}^{(i)} = \frac{3\mu_0}{4\pi d^4}\left(\mathbf{d}_0(\mathbf{m}^{(1)} \cdot \mathbf{m}^{(2)}) + \mathbf{m}^{(1)}(\mathbf{d}_0 \cdot \mathbf{m}^{(2)}) + \mathbf{m}^{(2)}(\mathbf{d}_0 \cdot \mathbf{m}^{(1)}) - 5\mathbf{d}_0(\mathbf{d}_0 \cdot \mathbf{m}^{(2)})(\mathbf{d}_0 \cdot \mathbf{m}^{(1)})\right) \tag{5.6}$$

where $\mathbf{m}^{(1)}$ and $\mathbf{m}^{(2)}$ are the dipole moments of the 1^{st} and 2^{nd} microrobots respectively, $\hat{\mathbf{d}} = \frac{\mathbf{p}^{(2)} - \mathbf{p}^{(1)}}{d}$ is the unit vector and $d = |\mathbf{p}^{(2)} - \mathbf{p}^{(1)}|$ is the distance between the microrobots. The magnetic interaction force, $\mathbf{F}_{\text{int}}^{(i)}$, between any two magnetic particles (here two microrobots) always acts along the same line

in opposite direction, as shown in section 5.6.2.
Balancing the three forces, $\mathbf{F}_{\text{int}}^{(i)}$, $\mathbf{F}_{d}^{(i)}$ and $\mathbf{F}_{m}^{(i)}$, I can write

$$\mathbf{F}_{\text{int}}^{(i)} + \mathbf{F}_{d}^{(i)} + \mathbf{F}_{m}^{(i)} = 0 \tag{5.7}$$

Thus, the velocity vector of the i^{th} microrobot of radius $R^{(i)}$

$$\mathbf{v}^{(i)} = \frac{\mathbf{F}_{\text{int}}^{(i)} + V^{(i)} M_s \frac{\partial B_z}{\partial x} [1,0,0]^T}{6\pi\eta k^{(i)} R^{(i)}} \tag{5.8}$$

where $k^{(i)}$ is the Stokes correction factor. For spheres, $k^{(i)} = 1$. The change in the position of each microrobot, $\mathbf{p}^{(i)}$, can be given by

$$\frac{d}{dt}\mathbf{p}^{(i)} = \mathbf{v}^{(i)} \tag{5.9}$$

5.4 Results

5.4.1 Spherical microrobots

The microrobots begin with positions $\mathbf{p}^{(1)} = (-5, 0, 0)$ mm and $\mathbf{p}^{(2)} = (5.4286, 0, 0)$ mm. Noting the alignment of the magnetic moments of the microrobots, shown in Figure 5.1, the direction of $\mathbf{F}_{\text{int}}^{(i)}$ is repulsive. Both $\mathbf{F}_{d}^{(i)}$ and $\mathbf{F}_{m}^{(i)}$ are dependent on $R^{(i)}$, so the microrobots begin with different velocities determined by their individual sizes. Initially, microrobot 1 is faster than microrobot 2. However, for microrobot 1, $\mathbf{F}_{m}^{(1)}$ and $\mathbf{F}_{\text{int}}^{(1)}$ oppose each other. For microrobot 2, $\mathbf{F}_{m}^{(2)}$ and $\mathbf{F}_{\text{int}}^{(2)}$ act in the same direction. As the distance, d, between the microrobots decreases, $\mathbf{F}_{\text{int}}^{(1)}$ increases, slowing down microrobot 1 and speeding up microrobot 2.
Since the directions of $\mathbf{F}_{\text{int}}^{(1)}$ and $\mathbf{F}_{m}^{(1)}$ are opposite, when the value of $|\mathbf{F}_{\text{int}}^{(i)}|$ is equal to the $|\mathbf{F}_{m}^{(2)} - \mathbf{F}_{m}^{(1)}|$, the distance between the microrobots reaches a constant value.

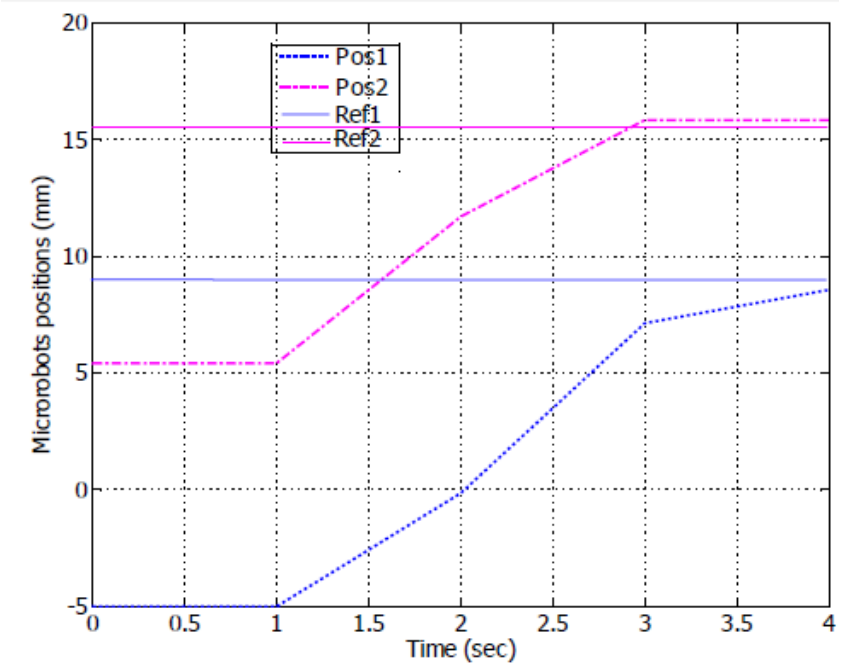

(a) Experimental observation taken directly from Mellal *et al.* [19].

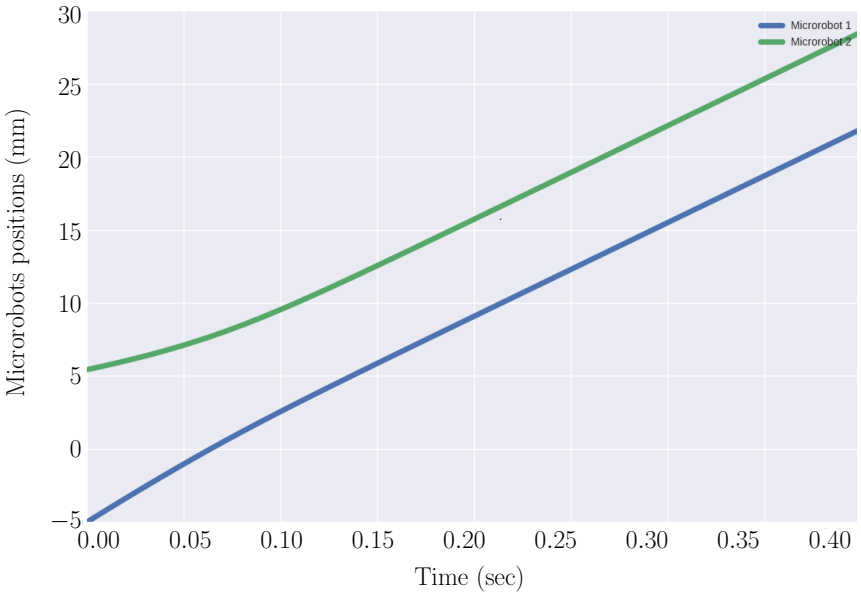

(b) Calculated positions of the microrobots.

Figure 5.2: Trajectories of the microrobots with time.

The initial idleness of the microrobots in the time range 0 s $< t \leq$ 1 s in the experimental data in Figure 5.2a, in [19], is accounted for by the presence of adhesive forces. The model presented in this chapter currently does not include adhesive forces. The relative distancing of the microrobots in the time range 1 s $< t \leq$ 2 s in Figure 5.2a, can be accounted for since the bigger microrobot experiences greater adhesive force, delaying its motion. Once both microrobots start moving, the bigger microrobot attains a greater velocity due to its size and the distance, d, decreases in the time range 2 s $< t \leq$ 3 s. However, aggregation between the microrobots is hindered due to the repulsive nature of the interaction force and both microrobots adjust themselves to a common velocity in the time range 3 s $< t \leq$ 4 s. Figure 5.2b refers to the calculated trajectories of the microrobots. Qualitative agreement is obtained

with Figure 5.2a and both the microrobots adjust to a common velocity.
Equating, equations (5.1) and (5.6), (the simplified form of equation (5.6) is given in equation (5.15)) the minimum distance between the microrobots, at which the $|\mathbf{F}_m^{(1)}|$ is equal to $|\mathbf{F}_{\text{int}}^{(i)}|$ can be written as

$$d_{\min} = \sqrt[4]{\frac{6\mu_0|\mathbf{m}_1||\mathbf{m}_2|}{4\pi|\mathbf{F}_{m,\max}|}} \tag{5.10}$$

where $|\mathbf{F}_{m,\max}| = |\mathbf{F}_m^{(1)}|$ is the magnitude of maximum magnetic force generated by the external gradient (since $\mathbf{F}_m^{(1)} > \mathbf{F}_m^{(2)}$). The expression of $d_{\min}$ given in Mellal *et al.* with a possible typographical error is,

$$d_{\min} = \frac{6\mu_0|\mathbf{m}_1||\mathbf{m}_2|}{4\pi|\mathbf{F}_{m,\max}|} \tag{5.11}$$

In Figure 5.3, the value of $d_{\min}$, being inversely proportional to $|\mathbf{F}_{m,\max}|$, decreases with increasing gradient. The red line shows the value of $d_{\min}$ obtained using the expression of Mellal *et al.* and the green line shows the value obtained using equation (5.10) when $\frac{\partial B_z}{\partial x} = 0.5\ \text{T m}^{-1}$.

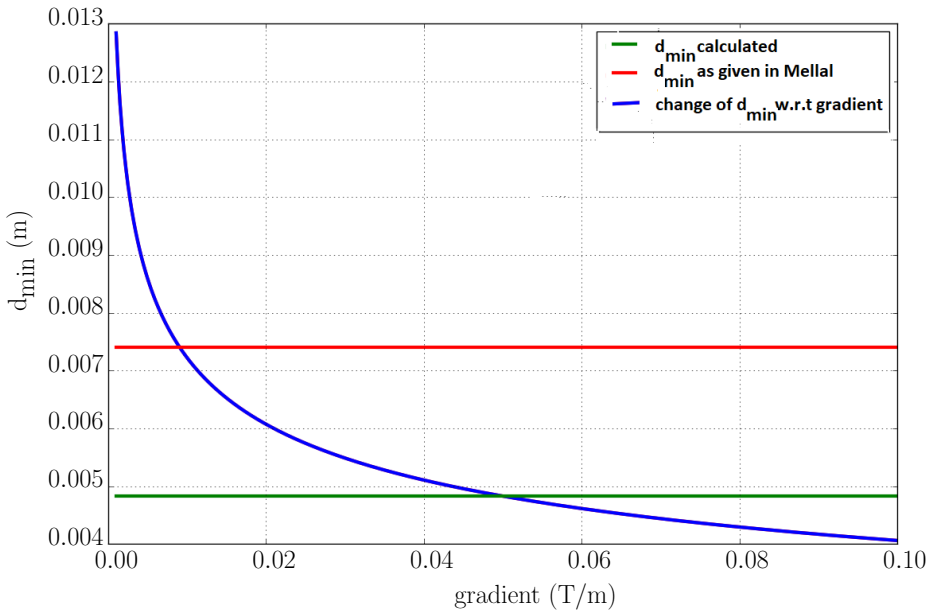

Figure 5.3: Calculation of $d_{\min}$ as given in equations (5.10) and (5.11) when the external gradient is 0.5 T m^{-1} and the change of $d_{\min}$ w.r.t. the external gradient experienced, $\frac{\partial B_z}{\partial x}$.

Figure 5.3 shows that as the magnetic force due to the external gardient increases, even though the microrobots experience repulsive interaction force, the separation distance decreases. This is caused only when the overall interaction force is less that the maximum magnitude of magnetic gradient, $|\mathbf{F}_{int}| < |\mathbf{F}_{m,\max}|$.

5.4.2 Non-spherical microrobots

Microrobots are a colloidal suspension of MNPs and their shapes appear to be spheroidal as given in the experimental diagram of Mellal *et al.* (Figure 5.4).

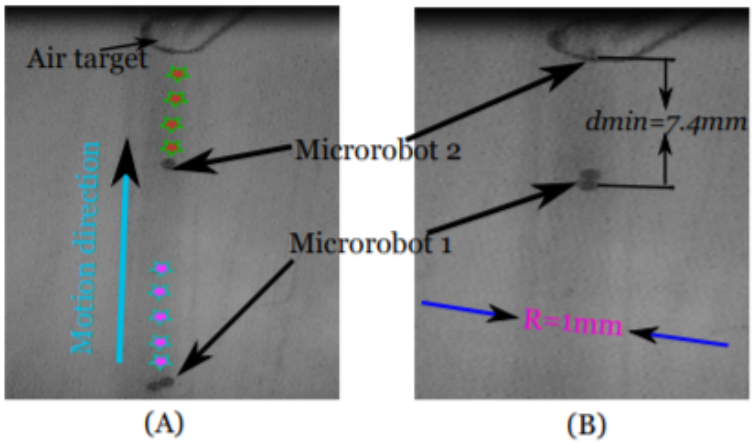

Figure 5.4: Experimental diagram of Mellal *et al.* (A): microbeads at their initial positions, and (B): microbeads at the final positions

The motion of non-spherical microrobots is similar to that of spherical ones. However, the steady state distance value changes according to the Stokes correction factor, $k^{(i)}$, of the microrobots (Figure 5.5a). As given in chapter 3, the Stokes correction factor, $k^{(i)}$, for a spheroid of aspect ratio, l_r, can be defined as the ratio of solid spheroid drag force to solid sphere drag force (where both have the same volume equivalent radius) [66],

$$k^{(i)} = \frac{f_d(l_r, Re \to 0)}{6\pi\eta r \mathbf{v}^{(i)}} \tag{5.12}$$

The value of $k^{(i)} \to 1$ as $l_r \to 1$. As shown in Figure 5.5a, $l_r = \frac{d_{||}}{d_\perp}$, where $d_{||}$ and $d_\perp$ are the parallel and normal diameters of a spheroid. The Stokes drag regime is when the value of Reynolds number, $Re \ll 1$. In the presence of an external gradient, the distance, d, between the microrobots decreases and then reaches a constant value when the magnitude of repulsive dipolar interaction force is equal to the difference in the magnetic force experienced by the microrobots $\left(|\mathbf{F}_m^{(2)} - \mathbf{F}_m^{(1)}|\right)$. Figure 5.5b shows that the time taken by the microrobots to reach a constant d changes with the value of l_r.

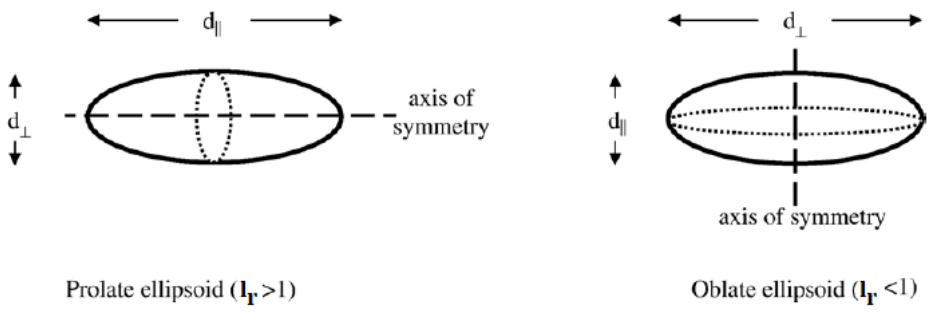

(a) Prolate and Oblate microrobots.

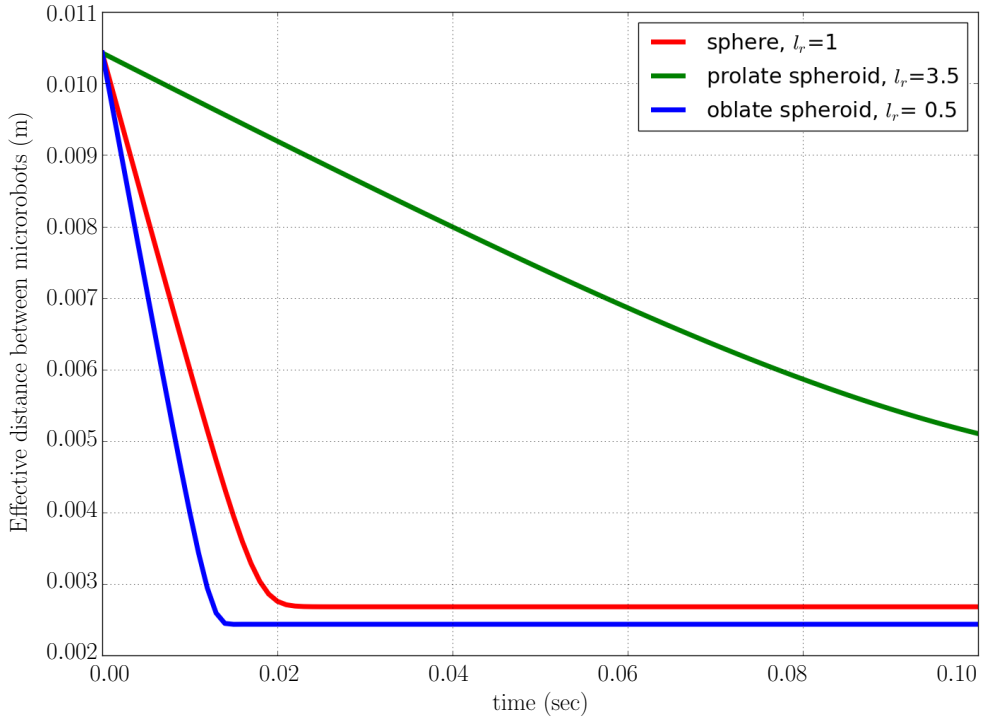

(b) Change of the distance between the microrobots, d, with time in different values Stokes correction factor.

Figure 5.5: Change of the distance between the microrobots with Stokes correction factor.

Figure 5.5b shows that when the microrobots are prolate spheroids the magnetic interaction force is the highest and it takes longer for the microrobots to reach a constant value of d. On the other hand when the microrobots are oblate spheroids, magnetic interaction force is the lowest and a constant value of d is attained much sooner.

5.5 Conclusion

Mellal *et al.* presented a model of two interacting MNPs, with experimental results. Therefore, this paper was selected to model in order to learn about magnetic interactions and validate the results. The numerical and typographical errors found in [19] are corrected.

Microrobots are a colloidal suspension of MNPs and their shapes appear to be spheroidal from the experimental pictures in Mellal *et al.* (Figure 5.4). In their paper Mellal *et al.* model the particles as spheres. In this chapter their model is extended to account for this spheroidal nature noting the appropriate Stokes correction factors. Figures 5.5a and 5.5b accounts for the change in distance between

the microrobots with Stokes correction factor.
This situation of the microrobots adjusting to a common velocity and moving in a straight line is highly unstable and is unlikely to occur in reality. There is a strong probability that the nature of the magnetic interaction force will push either/both of the microrobots from its trajectory and will eventually lead to aggregation. The diameter of the tube (2 mm) is 4 times bigger than the radius of the largest microrobot (500 μm), which may allow the mircrorobots to have enough space to aggregate. Neither the mathematical model nor the experimental results presented in Mellal *et al.* account for this phenomenon.

5.6 Appendix

While deriving equation (5.11), in Mellal *et al.*, it was found that that the scalar form of the dipolar interaction force had typographical/presentational errors. Therefore, two simple proofs of the dipolar interaction force are presented in this section.

5.6.1 Simplification of the expressions for interaction force

The magnetic interaction force can be written in two expressions,

$$\mathbf{F}_{\text{int}} = \frac{3\mu_0}{4\pi d^4}\Big(\mathbf{d}_0(\mathbf{m}^{(1)}\cdot\mathbf{m}^{(2)}) + \mathbf{m}^{(1)}(\mathbf{d}_0\cdot\mathbf{m}^{(2)}) + \mathbf{m}^{(2)}(\mathbf{d}_0\cdot\mathbf{m}^{(1)}) - 5\mathbf{d}_0(\mathbf{d}_0\cdot\mathbf{m}^{(2)})(\mathbf{d}_0\cdot\mathbf{m}^{(1)})\Big) \tag{5.13}$$

and

$$\mathbf{F}_{\text{int}} = \frac{3\mu_0}{4\pi d^4}\Big((\hat{\mathbf{d}}\times\mathbf{m}^{(1)})\times\mathbf{m}^{(2)} + (\hat{\mathbf{d}}\times\mathbf{m}^{(2)})\times\mathbf{m}^{(1)} - 2\hat{\mathbf{d}}(\mathbf{m}^{(1)}\cdot\mathbf{m}^{(2)}) + 5\hat{\mathbf{d}}((\hat{\mathbf{d}}\times\mathbf{m}^{(1)})\cdot(\hat{\mathbf{d}}\times\mathbf{m}^{(2)}))\Big) \tag{5.14}$$

When the magnetic moments of two MNPs are parallel, *i.e.* $\mathbf{m}^{(1)} = |\mathbf{m}^{(1)}|\hat{\mathbf{m}}$ and $\mathbf{m}^{(2)} = |\mathbf{m}^{(2)}|\hat{\mathbf{m}}$, equations (5.13) and (5.14) can be written as,

$$\mathbf{F}_{\text{int}} = \frac{3\mu_0|\mathbf{m}^{(1)}||\mathbf{m}^{(2)}|}{4\pi d^4}\Big(\hat{\mathbf{d}}(1-5(\hat{\mathbf{d}}\cdot\hat{\mathbf{m}})^2) + 2\hat{\mathbf{m}}(\hat{\mathbf{d}}\cdot\hat{\mathbf{m}})\Big) \tag{5.15}$$

and

$$\mathbf{F}_{\text{int}} = \frac{3\mu_0|\mathbf{m}^{(1)}||\mathbf{m}^{(2)}|}{4\pi d^4}\Big(2((\hat{\mathbf{d}}\times\hat{\mathbf{m}})\times\hat{\mathbf{m}}) - \hat{\mathbf{d}}(2-5(\hat{\mathbf{d}}\times\hat{\mathbf{m}})^2)\Big) \tag{5.16}$$

Using the rules of triple product of vectors, equation (5.16) can be simplified in

$$\mathbf{F}_{\text{int}} = \frac{3\mu_0|\mathbf{m}^{(1)}||\mathbf{m}^{(2)}|}{4\pi d^4}\Big(2(-\hat{\mathbf{d}}+\hat{\mathbf{m}}(\hat{\mathbf{d}}\cdot\hat{\mathbf{m}})) - \hat{\mathbf{d}}(2-5(\hat{\mathbf{d}}^2\hat{\mathbf{m}}^2-(\hat{\mathbf{d}}\cdot\hat{\mathbf{m}})^2)\Big) \tag{5.17}$$

$$= \frac{3\mu_0|\mathbf{m}^{(1)}||\mathbf{m}^{(2)}|}{4\pi d^4}\Big(-4\hat{\mathbf{d}} + 2\hat{\mathbf{m}}(\hat{\mathbf{d}}\cdot\hat{\mathbf{m}}) + 5\hat{\mathbf{d}}(1-(\hat{\mathbf{d}}\cdot\hat{\mathbf{m}})^2)\Big) \tag{5.18}$$

$$= \frac{3\mu_0|\mathbf{m}^{(1)}||\mathbf{m}^{(2)}|}{4\pi d^4}\Big(2\hat{\mathbf{m}}(\hat{\mathbf{d}}\cdot\hat{\mathbf{m}}) + \hat{\mathbf{d}}(1-5(\hat{\mathbf{d}}\cdot\hat{\mathbf{m}})^2)\Big) \tag{5.19}$$

Thus, equation (5.15) is equivalent to equation (5.19). This confirms that when the magnetic moments of any two MNPS are parallel to each other, the two expressions of dipolar interaction force as given

in equations (5.13) and (5.14) are the same.

5.6.2 Direction of the interaction force

If $\hat{\mathbf{m}}^{(2)} = -\hat{\mathbf{m}}^{(1)}$, and from the rules of dot product, $\hat{\mathbf{m}}^{(1)} \cdot (-\hat{\mathbf{m}}^{(1)}) = -1$, then equation (5.13), can be written as

$$\mathbf{F}_{\text{int}} = \frac{3\mu_0|\mathbf{m}^{(1)}||\mathbf{m}^{(2)}|}{4\pi d^4}\left(\hat{\mathbf{d}}(-1) + \hat{\mathbf{m}}^{(1)}(\hat{\mathbf{d}} \cdot (-\hat{\mathbf{m}}^{(1)})) + (-\hat{\mathbf{m}}^{(1)})(\hat{\mathbf{d}} \cdot \hat{\mathbf{m}}^{(1)}) + 5\hat{\mathbf{d}}(\hat{\mathbf{d}}) \cdot \hat{\mathbf{m}}^{(1)})^2\right) \tag{5.20}$$

$$= -\frac{3\mu_0|\mathbf{m}^{(1)}||\mathbf{m}^{(2)}|}{4\pi d^4}\left(2\hat{\mathbf{m}}^{(1)}(\hat{\mathbf{d}} \cdot \hat{\mathbf{m}}^{(1)}) + \hat{\mathbf{d}}(1 - 5(\hat{\mathbf{d}} \cdot \hat{\mathbf{m}}^{(1)})^2)\right) \tag{5.21}$$

If $\hat{\mathbf{m}}^{(2)} = \hat{\mathbf{m}}^{(1)}$, then equation (5.13), can be written as,

$$\mathbf{F}_{\text{int}} = \frac{3\mu_0|\mathbf{m}^{(1)}||\mathbf{m}^{(2)}|}{4\pi d^4}\left(\hat{\mathbf{d}}(1) + \hat{\mathbf{m}}^{(1)}(\hat{\mathbf{d}} \cdot (\hat{\mathbf{m}}^{(1)})) + (\hat{\mathbf{m}}^{(1)})(\hat{\mathbf{d}} \cdot \hat{\mathbf{m}}^{(1)}) - 5\hat{\mathbf{d}}(\hat{\mathbf{d}}) \cdot \hat{\mathbf{m}}^{(1)})^2\right) \tag{5.22}$$

$$= \frac{3\mu_0|\mathbf{m}^{(1)}||\mathbf{m}^{(2)}|}{4\pi d^4}\left(2\hat{\mathbf{m}}^{(1)}(\hat{\mathbf{d}} \cdot \hat{\mathbf{m}}^{(1)}) + \hat{\mathbf{d}}(1 - 5(\hat{\mathbf{d}} \cdot \hat{\mathbf{m}}^{(1)})^2)\right) \tag{5.23}$$

Thus, equation (5.21) is equivalent with the negative of equation (5.23). This confirms that $\mathbf{F}_{\text{int}}$ between any two magnetic particles is always oppositely directed with respect to each other.

Chapter 6

Dipolar Interactions in MNPs in parabolic flow

A mathematical model is presented to study the role of the dipolar interaction force in the aggregation of MNPs in rectangular and parabolic flow. Starting with two MNPs, the model accounts for a uniform random distribution of multiple MNPs along the x-axis of the vessel and predicts the size and nature of aggregation that occurs in different values of fluid velocity. It was found that in parabolic flow, at a specific fluid velocity, there exists a critical distance range along the x-axis within which if the MNPs begin, aggregation occurs.

6.1 Additional list of symbols

- R, initial average radius of the MNPs ..... m
- $R^{(i)}$, radius of the i^{th} MNP ..... m
- $V^{(i)}$, volume of the i^{th} MNP ..... m^3
- $\hat{\mathbf{m}}$, unit vector in direction of $\mathbf{B}$[1] ..... dimensionless
- $\mathbf{m}$, the common magnetic moment ..... $A\,m^2$
- $\mathbf{m}^{(i)}$, magnetic moment of the i^{th} MNP ..... $A\,m^2$
- $\mathbf{p}^{(i)}$, position of the i^{th} MNP ..... m
- $d^{(i,j)} = ||\mathbf{p}^{(i)} - \mathbf{p}^{(j)}||$, distance between the centres of the i^{th} and the j^{th} MNP ..... m
- $\hat{\mathbf{d}}^{(i,j)} = \frac{\mathbf{p}^{(i)} - \mathbf{p}^{(j)}}{d^{(i,j)}}$, unit vector along the line of MNP centres from i^{th} to j^{th} MNPs dimensionless
- d_R, distance relative to R ..... dimensionless
- r, distance between the MNPs along the x-axis ..... m
- r_{crit}, simulated value of the distance between the MNPs along the x-axis ..... m
- r_{low}, analytic lower limit of the distance between the MNPs along the x-axis ..... m
- r_{high}, analytic upper limit of the distance between the MNPs along the x-axis ..... m
- r_{emp}, empirical approximation of r_{crit} ..... m
- θ, angle between the line joining the centres of the MNPs and the common magnetic moment . radians
- $\mathbf{F}_m^{(i)}$, magnetic force experienced by the i^{th} MNP ..... N

[1] In the list of common symbols, $\mathbf{B}$ is defined as the magnetic field.

- $\mathbf{F}_d^{(i)}$, drag force experienced by the i^{th} MNP ..... N
- $\mathbf{F}_{\text{int}}^{(i)}$, dipolar interaction force experienced by the i^{th} MNP ..... N

Table 6.1: List of parameters values for chapter 6.

Parmeter	Description	Value
R	initial average radius of the MNPs	500×10^{-9} m
M_s	saturation magnetisation	$1.23 \times 10^{6}\,\text{A}\,\text{m}^{-1}$
η	fluid viscosity	$1.6 \times 10^{-3}\,\text{kg}\,\text{m}^{-1}\,\text{s}^{-1}$
$\overline{v}_f$	average fluid velocity	$10^{-3}\,\text{m}\,\text{s}^{-1}$

6.2 Introduction

In this chapter, a mathematical model is presented to study the trajectories of multiple MNPs in parabolic flow, which includes dipolar interaction and drag force. Initially the MNPs are either positioned manually or they are considered to have an uniform random distribution along the diameter of the vessel. Following the model of Riegler *et al.* [11], the magnetic moments of the MNPs are assumed to be aligned along the length of the vessel, throughout the simulation. According to the positions of the MNPs along the diameter of the vessel, the differential drag experienced by the MNPs varies, leading the MNPs to have different velocities. The differential drag refers to the difference in drag experienced at points in a parabolic flow or other non-rectangular flow.
As the positions of the MNPs change, the strength and direction of dipolar interaction forces between the MNPs change. When the distance between any two MNPs is equal to the sum of their radii, they are assumed to be touching. Here, the model pauses, assumes the MNPs to be aggregated in the form of a sphere with volume equivalent to the total volume of the aggregated MNPs and resumes the calculations. The simulations run until a specific time or until all the MNPs aggregate. The effects of the following parameters on the aggregation of MNPs are assessed:

- the average fluid velocity.
- initial positions of the MNPs along the x-axis.
- the initial angle, θ, between the line joining the centres of the MNPs and the common magnetic moment.

Aggregations occurring in 2 to 50 MNPs are studied in detail. This work was motivated by the results of Riegler *et al.* [11, 12, 14], where the discrepancies between the theoretical and experimental results were entirely attributed to the aggregation of the MNPs. I find that in rectangular/no flow all the MNPs aggregate with time. However, in parabolic flow, for a specific value of fluid velocity, there exists a critical distance, r_{crit}, along the diameter of the vessel within which if the MNPs begin, aggregation occurs over time. This value of r_{crit} obtained in the model is investigated when the only forces present in the model are the dipolar interaction force and the fluid force. Equating the two forces, analytic upper and lower limits for the value r_{crit} is obtained. The numerical results are shown to be within these limits.

6.3 The physical setup

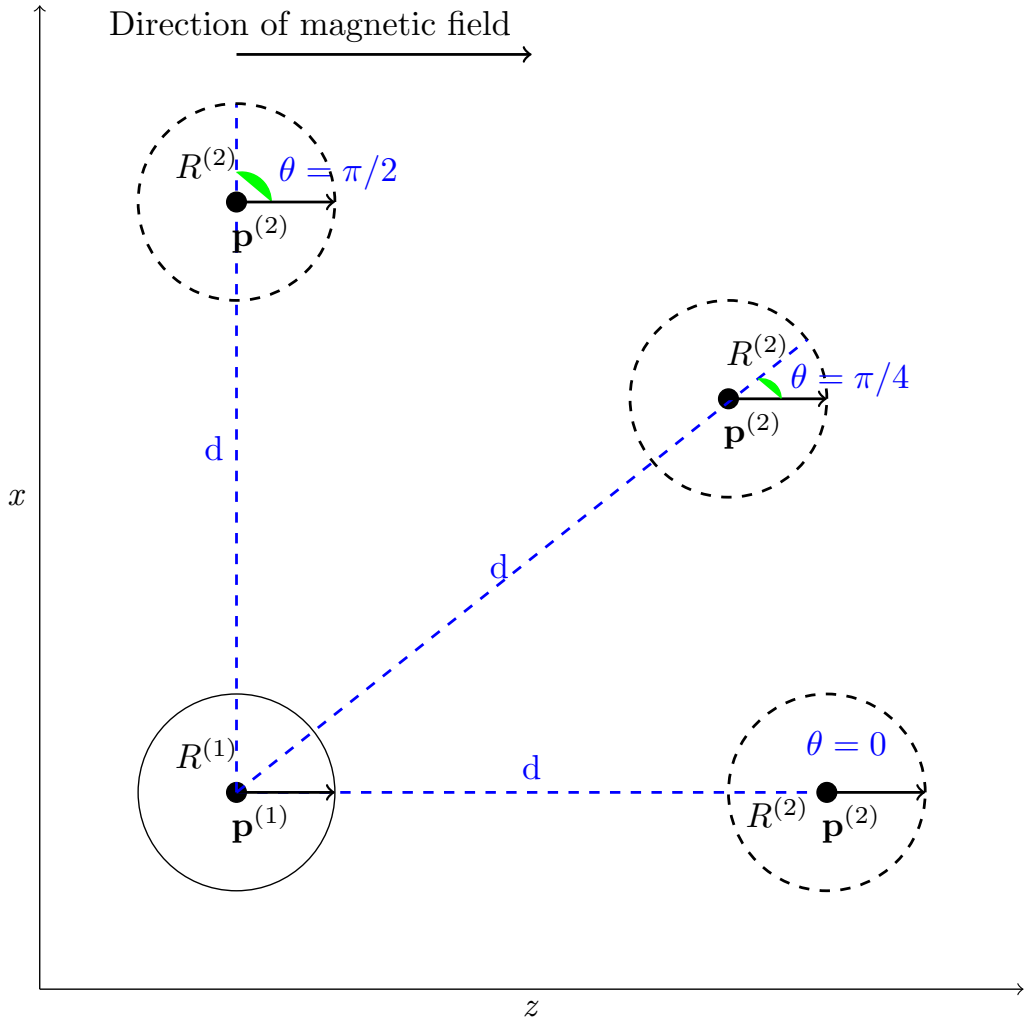

Figure 6.1: Diagram of θ w.r.t. fixed $\mathbf{p}^{(1)}$ and varying $\mathbf{p}^{(2)}$, where θ is the angle between the line joining the centres of the MNPs and the common magnetic moment, $\mathbf{m}$, of the MNPs.

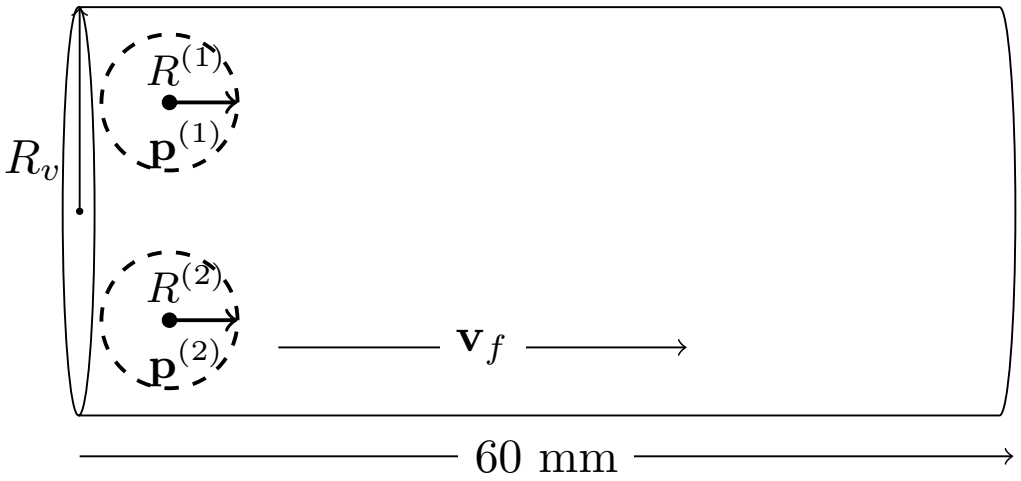

Figure 6.2: The simulated setup[2].

6.4 Magnetic force

In this model a uniform magnetic field is assumed, which can be produced by Helmholtz, Merritt or Ruben coil systems [75]. The force experienced by the i^{th} MNP, due to an external gradient is termed as the magnetic force, $\mathbf{F}_m^{(i)}$. This model is capable of including an external gradient, however in the current calculations this is taken to be zero.

6.5 Magnetic interaction force

The magnetic interaction force on the i^{th} particle due to the j^{th} particle is given as

$$\mathbf{F}_{\text{int}}^{(i,j)} = \frac{3\mu_0}{4\pi(d^{(i,j)})^4}\Big(\hat{\mathbf{d}}^{(i,j)}(\mathbf{m}^{(i)}\cdot\mathbf{m}^{(j)}) + \mathbf{m}^{(i)}(\hat{\mathbf{d}}^{(i,j)}\cdot\mathbf{m}^{(j)}) + \mathbf{m}^{(j)}(\hat{\mathbf{d}}^{(i,j)}\cdot\mathbf{m}^{(i)}) - 5\hat{\mathbf{d}}^{(i,j)}(\hat{\mathbf{d}}^{(i,j)}\cdot\mathbf{m}^{(i)})(\hat{\mathbf{d}}^{(i,j)}\cdot\mathbf{m}^{(j)})\Big) \tag{6.1}$$

where $\mathbf{m}^{(i)}$, $\mathbf{m}^{(j)}$ are the dipole moments and $\mathbf{p}^{(i)}$, $\mathbf{p}^{(j)}$ are the locations of the i^{th} and j^{th} MNPs respectively, $\hat{\mathbf{d}}^{(i,j)} = \frac{\mathbf{p}^{(j)}-\mathbf{p}^{(i)}}{\left\|\mathbf{p}^{(j)}-\mathbf{p}^{(i)}\right\|}$ is the unit vector and $d^{(i,j)} = \left\|\mathbf{p}^{(j)}-\mathbf{p}^{(i)}\right\|$ is the distance between the centres of the i^{th} and j^{th} MNPs. The total magnetic interaction force experienced by the i^{th} MNP, $\mathbf{F}_{\text{int}}^{(i)}$, due to the remaining $n-1$ MNPs is

$$\mathbf{F}_{\text{int}}^{(i)} = \sum_{j=1,j\neq i}^{n} \mathbf{F}_{\text{int}}^{(i,j)} \tag{6.2}$$

where the n denotes the total number of MNPs [3]. The magnetic interaction force between any two MNPs always acts in opposite direction w.r.t. each other.

When $\mathbf{m}^{(i)} = \mathbf{m}^{(j)} = \mathbf{m} = |\mathbf{m}|\hat{\mathbf{m}}$, a simplified expression of equation (6.1) is

$$\mathbf{F}_{\text{int}} = \frac{3\mu_0|\mathbf{m}|^2}{4\pi d^4}\left[\hat{\mathbf{d}}(1-5\cos^2\theta) + 2\hat{\mathbf{m}}\cos\theta\right] \tag{6.3}$$

where θ is the angle between the line joining the centres of the MNPs and the common magnetic moment, $\mathbf{m}$. When $\theta = 63.43°$, the value of $|\mathbf{F}_{\text{int}}|$ is at a minimum.
The scalar product of $\mathbf{F}_{\text{int}}$ and $\hat{\mathbf{d}}$ is

$$\mathbf{F}_{\text{int}}\cdot\hat{\mathbf{d}} = \frac{3\mu_0|\mathbf{m}|^2}{4\pi d^4}\left[\hat{\mathbf{d}}(1-5\cos^2\theta) + 2\hat{\mathbf{m}}\cos\theta\right]\cdot\hat{\mathbf{d}} \tag{6.4}$$

$$= \frac{3\mu_0|\mathbf{m}|^2}{4\pi d^4}\left[\left(1-5\cos^2\theta\right) + 2\cos^2\theta\right] \tag{6.5}$$

$$= \frac{3\mu_0|\mathbf{m}|^2}{4\pi d^4}\left[1-3\cos^2\theta\right] \tag{6.6}$$

When $\theta = 54.77° = \theta_c$, equation (6.6) is zero. At θ_c, the sign of the component of $\mathbf{F}_{\text{int}}$ along the line joining the centres of the MNPs, changes from being positive to negative (Figure 6.3).

[2] Not drawn to relative scale.

[3] Only in chapter 2, the number of MNPs is denoted by N. In the remaining chapters including this chapter, the number of MNPs is denoted by n.

Equation (6.6) can be expressed in terms of the second Legendre polynomial given by

$$P_2(x) = \frac{1}{2}(3x^2 - 1) \tag{6.7}$$

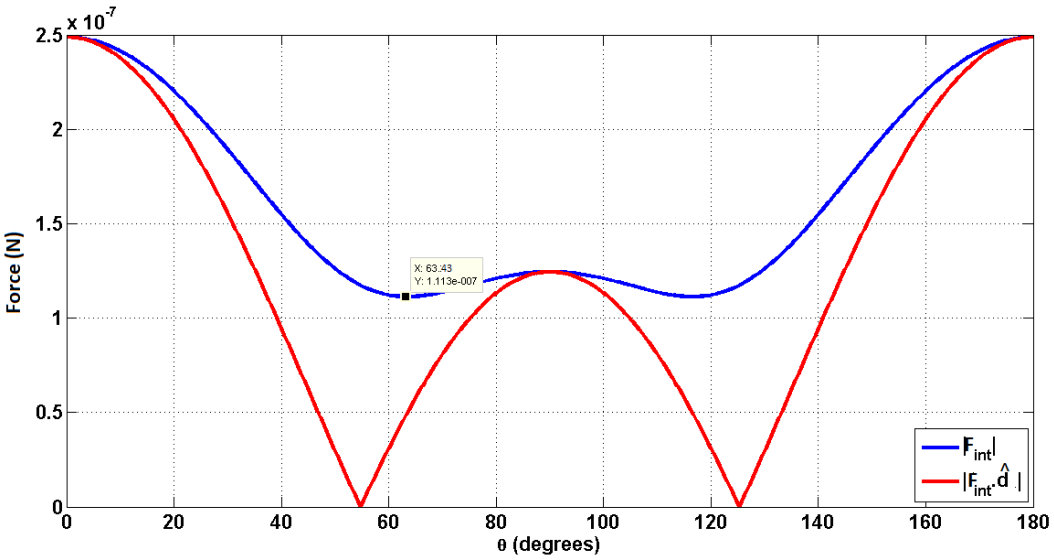

Figure 6.3: Plot of $|\mathbf{F}_{\text{int}}|$ and $|\mathbf{F}_{\text{int}} \cdot \hat{\mathbf{d}}|$ w.r.t. θ.

6.6 Fluid force

The Stokes' drag is given as

$$\mathbf{F}_d = -6\pi\eta R^{(i)}(\mathbf{v}^{(i)} - \mathbf{v}_f) \tag{6.8}$$

where η is the fluid viscosity, $\mathbf{v}_f$ is the fluid velocity and $\mathbf{v}^{(i)}$ is the velocity of the i^{th} MNP.
In the fluid velocity, $\mathbf{v}_f$, the velocity component in the direction normal to the flow is zero and non-slip boundary conditions are applied at the tube surface of contact. The parabolic fluid velocity, $\mathbf{v}_f$, is given as

$$\mathbf{v}_f = \left[0, 0, 2\overline{v}_f \left(1 - \left(\frac{x}{R_v}\right)^2\right)\right] \tag{6.9}$$

where $\overline{v}_f$ is the average fluid velocity. Balancing the three forces, $\mathbf{F}_{\text{int}}^{(i)}$, $\mathbf{F}_d^{(i)}$ and $\mathbf{F}_m^{(i)}$, I can write

$$\mathbf{F}_{\text{int}}^{(i)} + \mathbf{F}_d^{(i)} + \mathbf{F}_m^{(i)} = 0 \tag{6.10}$$

The velocity of the i^{th} MNP is given by

$$\mathbf{v}^{(i)} = \frac{\mathbf{F}_{\text{int}}^{(i)} + \mathbf{F}_m^{(i)}}{6\pi\eta R^{(i)}} + \mathbf{v}_f \tag{6.11}$$

In our model, because of the absence of an external gradient, $\mathbf{F}_m^{(i)} = 0$.
The position of each MNP is calculated by solving equation (6.12),

$$\frac{d\mathbf{p}^{(i)}}{dt} = \mathbf{v}^{(i)} \tag{6.12}$$

6.7 Algorithm to calculate the aggregation

The following algorithm is applied to calculate the aggregation of n MNPs, where $n \in \mathbb{N}$.

1. The initial positions of the MNPs can either be fixed manually or generated randomly. In either case, the MNPs are positioned along the x-axis. More details on the random distribution are included in section 6.10.2.1.

2. With the input arguments consisting of the initial values of positions and the starting time, the ode solver is called to solve equation (6.12). The R.H.S. of equation (6.12), is calculated from equation (6.11).

3. The ode solver is called in a loop until the maximum time is reached or until any p MNPs aggregate, where $p \in \mathbb{N}, p \geq 2$ and $p \leq n$.

4. The positions of the aggregated MNPs and the time instance of aggregation are recorded. In the list of aggregated MNPs, the lowest numbered MNP is retained and the rest of the MNPs are deleted.

5. In order to conserve the volume, from the total volume of the aggregated MNPs, the equivalent radius of a sphere is calculated. The radius of the retained MNP is updated to the equivalent radius. The calculations are then re-run from the recorded time instance until a certain value of time.

6.8 Dipolar interactions in uniform flow

In Figure 6.4, the trajectories of both MNPs relative to $\mathbf{p}^{(1)}$ are plotted. The starting positions of the MNPs are, $\mathbf{p}^{(1)} = (0, 0, 0)$ and $\mathbf{p}^{(2)} = d_R R(\sin\theta, 0, \cos\theta)$ where, $d_R = 20$, $0 < \theta \leq \pi/2$ and R is the initial average radius of the MNPs.
The initial distance relative to radius, d_R, is expressed as

$$d_R = \frac{d^{(i,j)}}{R} \tag{6.13}$$

In uniform flow, the effects of the dipolar interaction force can be summarised as follows:

- In Figure 6.4, when $\theta < \theta_c$, the MNPs attract each other. Here, $\theta_c \approx 54.77°$, is the critical angle, at which the sign of the component of the dipolar interaction force along the line joining the centres of the MNPs, changes from positive to negative.

- When $\theta > \theta_c$, the MNPs initially repel each other which changes the value of θ. As the value of θ approaches θ_c, the sign of the component of the dipolar interaction force along the line joining

the centres of the MNPs, changes from negative to positive. Figure 6.4 represents the closed curve nature of the magnetic field.

- When the initial distance between the centres of the MNPs is less than 50 radius ($d^{(i,j)} < 50R$), aggregation occurs in every value of θ, except when $\theta = \pi/2$.

Rectangular flow is comparable to no flow. Therefore, the above points are valid in the case of rectangular flow as well.

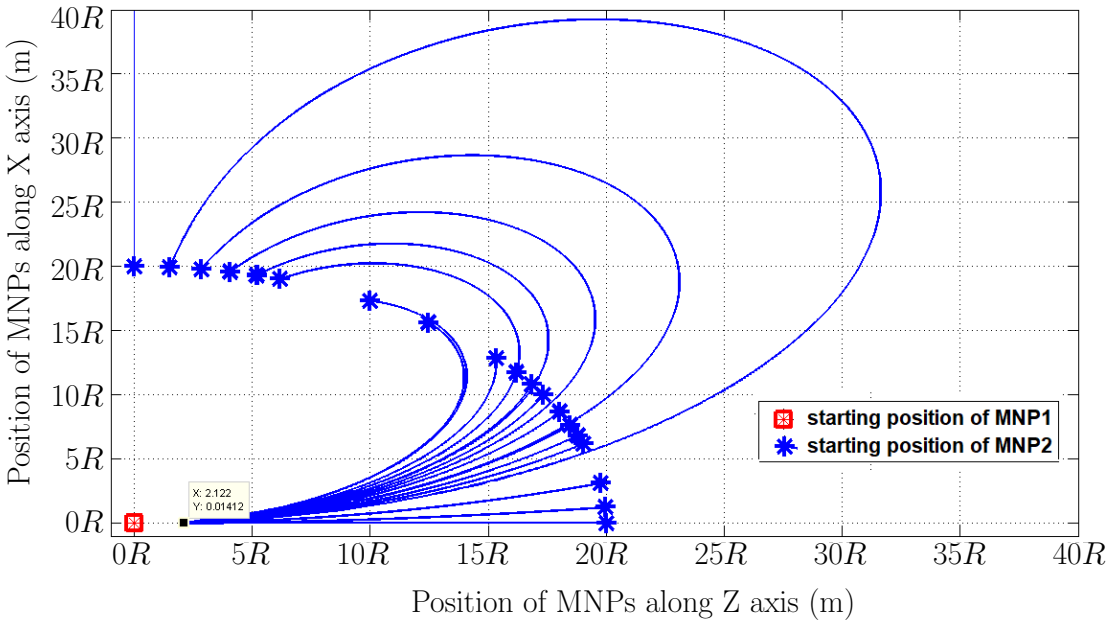

Figure 6.4: Relative trajectories of the MNPs w.r.t. MNP 1, when the initial value of $\mathbf{p}^{(1)}$ is fixed at the origin and the initial values of $\mathbf{p}^{(2)}$ change with θ, where $0 < \theta \leq \pi/2$.

6.9 Dipolar interactions in parabolic flow

In parabolic flow, the aggregation of the MNPs depends on the following factors.

6.9.1 The average fluid velocity, $\overline{v}_f$

1. In low $\overline{v}_f$, *i.e* $\overline{v}_f < 10^{-5}$ m s^{-1}, $\mathbf{F}_{\text{int}}^{(i)}$ dominates and the behaviour of the MNPs resembles that of no flow. The probability of aggregation of most/all of the MNPs, is very high.

2. In high $\overline{v}_f$, *i.e* $\overline{v}_f > 10^{-2}$ m s^{-1}, $\mathbf{F}_{d}^{(i)}$ dominates and depending on the positions of the MNPs along the x-axis, one MNP attains a higher velocity due to the differential drag. Due to the difference in the velocities, the distance, $d^{(i,j)}$, between the MNPs increases, which reduces the effective $\mathbf{F}_{\text{int}}^{(i)}$. Therefore, the probability of aggregation is low.

3. In the intermediate range, *i.e.* $10^{-5} < \overline{v}_f < 10^{-2}$ m s^{-1}, the values of $\mathbf{F}_{\text{int}}^{(i)}$ and $\mathbf{F}_{d}^{(i)}$ are comparable. The likelihood of aggregation in this range, is investigated in this chapter.

6.9.2 The capture range of aggregation

The differential drag in parabolic flow depends on the positions of the MNPs along the x-axis. For a particular value of $\overline{v}_f$, the capture range of aggregation, r_{crit}, can be defined as the largest initial distance between the MNPs along the x-axis, within which if the MNPs begin, aggregation occurs over time. The value of r_{crit}, at different values of $\overline{v}_f$ is calculated according to the following algorithm and represented in Figure 6.5 in terms of radius apart *i.e* d_R.

- The starting position of $\mathbf{p}^{(1)}$ is kept fixed at the origin.
- The initial z coordinate of the $\mathbf{p}^{(2)}$ is kept fixed while its initial x coordinate is varied using the bisection method, to locate the particular point, r_{crit}, beyond which if $\mathbf{p}^{(2)}$ begins, there is no aggregation.
- Once a value of r_{crit} is obtained, the initial z coordinate is increased to ensure consistency.
- As $\overline{v}_f$ increases, the value of r_{crit} decreases. This corresponds with the fact that in high values of $\overline{v}_f$ aggregation decreases.
  Analytic limits of the capture range are obtained and plotted alongside r_{crit} w.r.t. $\overline{v}_f$. (Figure 6.5)

Analytic limits of the relationship between r_{crit} and $\overline{v}_f$ can be obtained by equating the dipolar interaction force and the differential Stokes' drag. The analytic lower and upper limits, r_{low} and r_{high} respectively, are defined in equations (6.23) and (6.24).

6.9.2.1 Analytic derivation of r_{low} and r_{high} when $\Delta F_d = F_{int}$

When $\Delta F_d = F_{\text{int}}$, analytic lower and upper limits, r_{low} and r_{high} respectively, for the numerical data, r_{crit}, can be obtained. The fluid velocity at any point along the x-axis is given by the parabolic profile

$$v_f(x) = 2\overline{v}_f \left[1 - \left(\frac{x}{R_v}\right)^2\right] \tag{6.14}$$

Considering two MNPs located at points x_1 and x_2 along the x-axis, separated by a distance r, the change in the drag, ΔF_d, experienced by the MNPs is

$$\Delta F_d = \frac{2\overline{v}_f 6\pi\eta R}{R_v^2}\left[x_2^2 - x_1^2\right] \tag{6.15}$$

$$= k_d \overline{v}_f[(x_1 + r)^2 - x_1^2] \tag{6.16}$$

$$\text{where } k_d = \frac{12\pi\eta R}{R_v^2} \tag{6.17}$$

$$\Delta F_d = k_d \overline{v}_f[2x_1 r + r^2] \tag{6.18}$$

where $x_2 = x_1 + r$. Depending on the distance, r, between the two MNPs along the x-axis, equation (6.18) can be simplified in two ways.

1. When the MNPs are closely located along the x-axis, *i.e.* $r \ll x_1$, equation (6.18) can be written as

$$\Delta F_d = 2k_d \overline{v}_f x_1 r \tag{6.19}$$

2. When the MNPs are equally spaced along the x-axis *i.e.* $r = x_1$, equation (6.18) can be written as

$$\Delta F_d = 3k_d \overline{v}_f r^2 \tag{6.20}$$

When $\mathbf{m}^{(i)} = \mathbf{m}^{(j)} = |\mathbf{m}|\hat{\mathbf{m}}$, equation (6.1), can be written as

$$\mathbf{F}_{\text{int}} = \frac{3\mu_0|\mathbf{m}|^2}{4\pi d^4}\left(\hat{\mathbf{d}}(\hat{\mathbf{m}}\cdot\hat{\mathbf{m}}) + \hat{\mathbf{m}}(\hat{\mathbf{d}}\cdot\hat{\mathbf{m}}) + \hat{\mathbf{m}}(\hat{\mathbf{d}}\cdot\hat{\mathbf{m}}) - 5\hat{\mathbf{d}}(\hat{\mathbf{d}}\cdot\hat{\mathbf{m}})(\hat{\mathbf{d}}\cdot\hat{\mathbf{m}})\right) \tag{6.21}$$

If both $\hat{\mathbf{d}}$ and $\hat{\mathbf{m}}$ are in the same direction and along the x-axis, $r = d$, equation (6.21) reduces to

$$F_{\text{int}} = \frac{3\mu_0}{2\pi r^4}(VM_s)^2 = \frac{k_i}{r^4} \tag{6.22}$$

where $k_i = \frac{3\mu_0}{2\pi}\left(\frac{4\pi R^3 M_s}{3}\right)^2$.
Considering $\Delta F_d = F_{\text{int}}$,

- When the MNPs are very close to each other and equating equation (6.19) and equation (6.22), the lower limit of the capture range can be given as

$$r_{low} = \left(\frac{k_i}{k_d}\frac{1}{2\overline{v}_f x_1}\right)^{1/5} \tag{6.23}$$

- When the first MNP is equally spaced from the origin and the second MNP, equating equations equations (6.20) and (6.22), the upper limit of the capture range can be given as

$$r_{high} = \left(\frac{k_i}{k_d}\frac{1}{3\overline{v}_f}\right)^{1/6} \tag{6.24}$$

The limits r_{low} and r_{high} are obtained in two extreme cases. Equations (6.23) and (6.24) reveal a $1/5^{th}$ and $1/6^{th}$ power dependence of $\overline{v}_f$ with the lower and upper limits, respectively.
As given in equation (6.23), the lower limit, r_{low}, is obtained when the distance between the MNPs along the x-axis is very small, *i.e.* when $|x_2 - x_1| = r \ll 800R$, where $800R$ is the radius of the vessel. The limit, r_{low}, is valid for $x_1 > 0$, because at $x_1 = 0$ there is no linear variation in the parabolic differential drag and I get infinite critical distance as the lower limit. For r_{low}, the extreme lower bound can be obtained when, $x_1 = 800R$. However, close agreement with the numerical results has been observed with $x_1 = 200R$ in the same equation.
As given in equation (6.24), the upper limit, r_{high}, is obtained when the first MNP is equally spaced from the origin and the second MNP, along the x-axis. Unlike in r_{low}, here there is no explicit requirement of the locations of the MNPs and equation (6.24), is valid as long as $x_2 = 2x_1$.
As shown in Figure 6.5, the capture range, r_{crit}, obtained in the numerical calculations is within the lower limit, r_{low}, and the upper limit r_{high}. Improved numerical agreement is also observed with an empirical fit (equation (6.25)) valid throughout the range and accurate with a maximum error of less

than 2%. This formula is proposed by one of my supervisors, Dr PJ Cregg.

$$r_{emp} = 1.4\left(\frac{k_i}{3\overline{v}_f k_d}\right)^{0.1705} \tag{6.25}$$

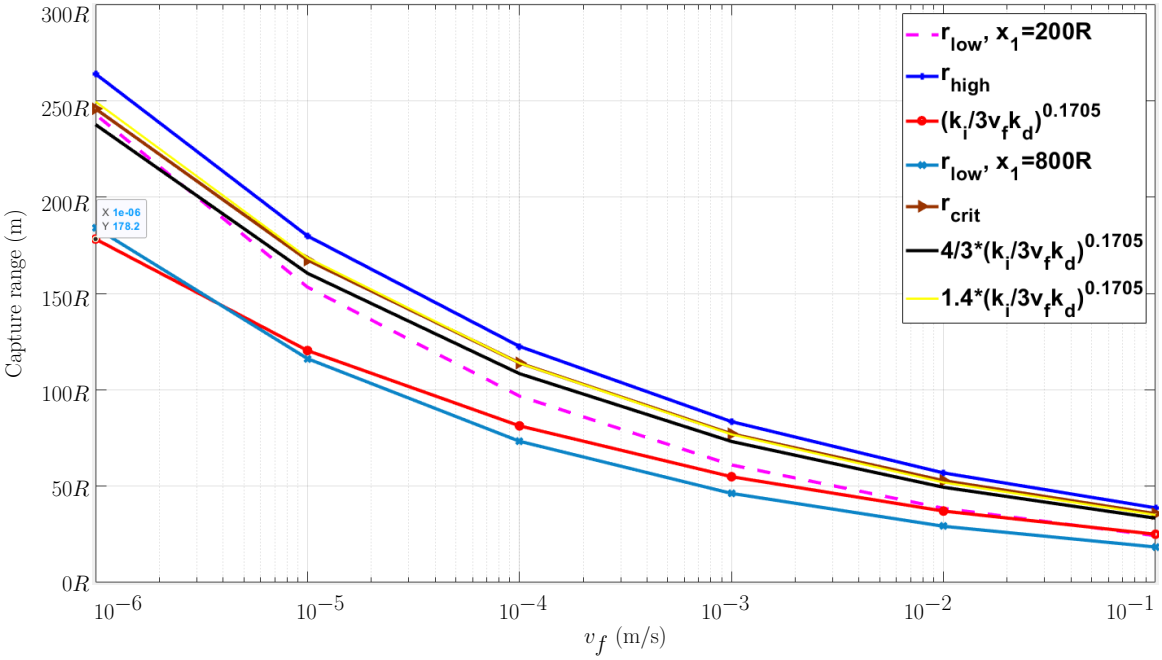

Figure 6.5: Plot of r_{crit}, r_{low} (from equation (6.23)), r_{high} (from equation (6.24)) and r_{emp} (from equation (6.25)), vs $\overline{v}_f$

6.9.3 The angle, θ, between the line joining the centres of the MNPs with the common magnetic moment.

1. From Figures 6.6 to 6.9, it can be concluded that when the initial positions of the MNPs are directly above each other *i.e.* ($\theta = \pi/2$), they do not aggregate for the given fluid velocities.

2. In Figures 6.6 to 6.9, the MNPs come closer in the x-axis but they get further apart in the z-axis.

3. Figures 6.6 to 6.9, are calculated till a particular distance, $d = 400000R$, along the z-axis, is travelled by the MNPs. All the figures show the same underlying pattern *i.e.* after a certain time, the difference in the positions of the MNPs, $d^{(i,j)}$, increases linearly with time.

4. As shown in Figure 6.10, when the configuration of the MNPs is slightly altered, *i.e.* $\theta \neq \pi/2$, the MNPs may aggregate.

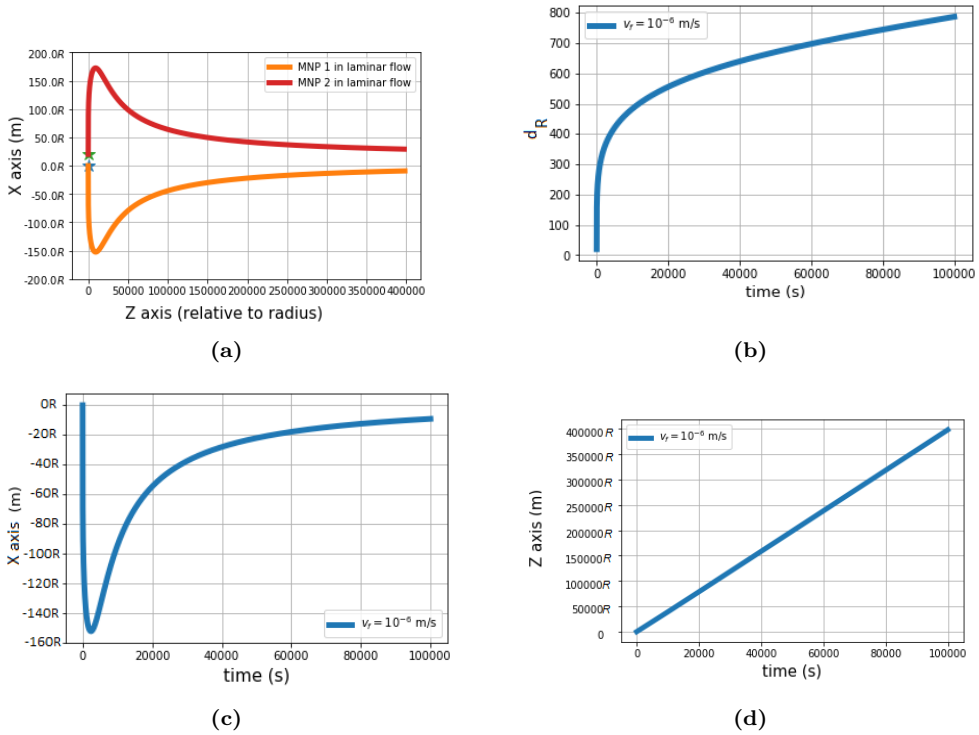

Figure 6.6: When $\overline{v}_f = 10^{-6}\ \mathrm{m\,s^{-1}}$ and $\theta = \pi/2$, (a): Plot of positions of MNPs. (b): Plot of distance between the MNPs, d_R, w.r.t. time, (c): Movement of MNP 1 along x-axis w.r.t. time, (d): Movement of MNP 1 along z-axis w.r.t. time.

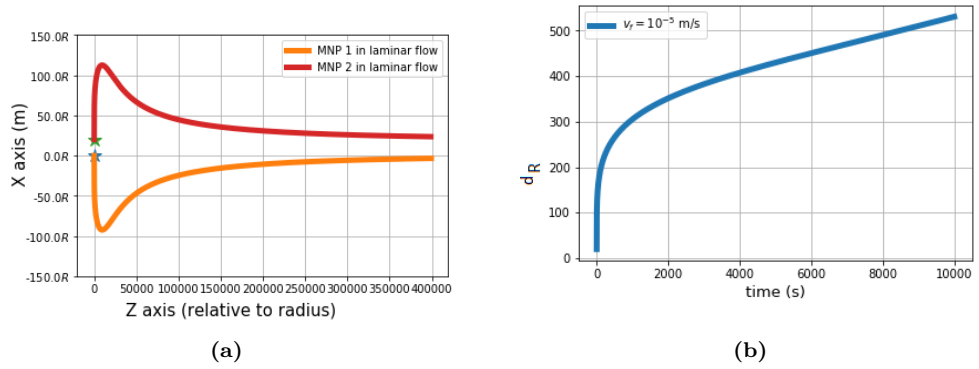

Figure 6.7: When $\overline{v}_f = 10^{-5}\ \mathrm{m\,s^{-1}}$ and $\theta = \pi/2$, (a): Plot of positions of MNPs. (b): Plot of d_R, w.r.t. time.

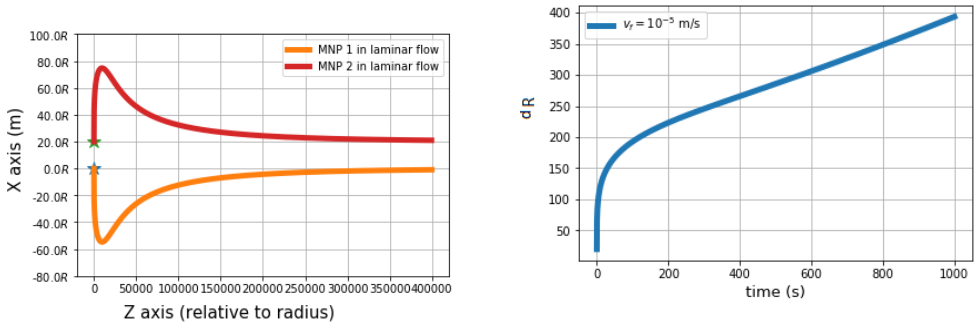

(a) **(b)**

Figure 6.8: When $\overline{v}_f = 10^{-4}\ \mathrm{m\,s^{-1}}$ and $\theta = \pi/2$, (a): Plot of positions of MNPs. (b): Plot of d_R, w.r.t. time.

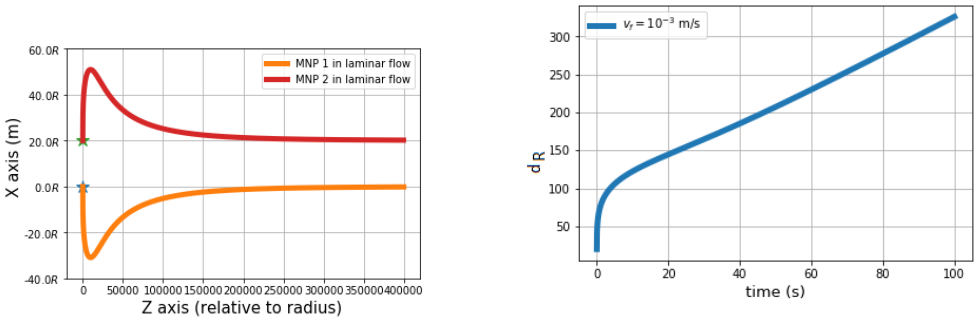

(a) **(b)**

Figure 6.9: When $\overline{v}_f = 10^{-3}\ \mathrm{m\,s^{-1}}$ and $\theta = \pi/2$, (a): Plot of positions of MNPs.(b): Plot of d_R, w.r.t. time.

Keeping all the physical conditions fixed as in Figure 6.9, if the position of the second MNP is slightly shifted so that the MNPs are not directly above each other *i.e.* when $\mathbf{p}^{(2)} = [20R, 0, R]$, the MNPs aggregate.

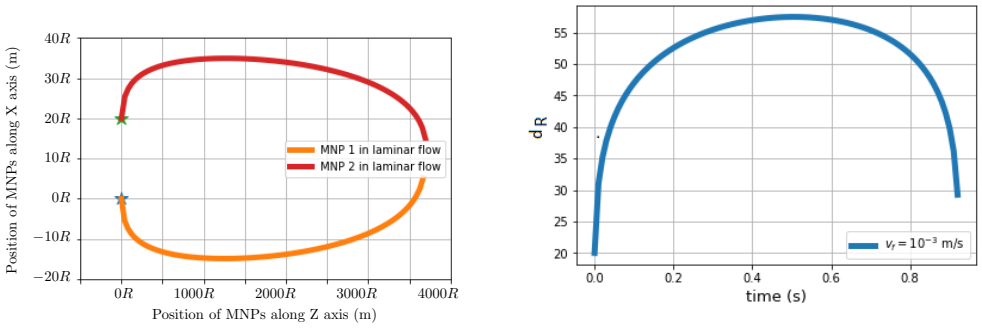

(a) **(b)**

Figure 6.10: When $\overline{v}_f = 10^{-3}\ \mathrm{m\,s^{-1}}$ and $\mathbf{p}^{(2)} = [20R, 0, R]$, (a): Plot of positions of MNPs. (b): Plot of d_R, w.r.t. time.

6.10 Multiple particles

6.10.1 Multiple MNPs with fixed initial positions

6.10.1.1 3 MNPs

1. When the MNPs are far apart *i.e.* $r \geq 100R$, there is no interaction between them. All three move with the fluid velocity.

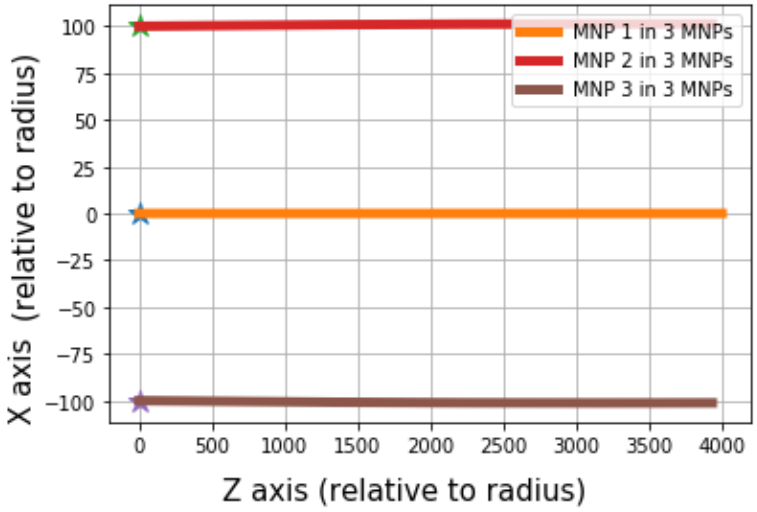

Figure 6.11: Trajectories of 3 MNPs when $r = 100R$.

2. In Figure 6.12a, when two of the MNPs are closer and the 3rd one is far apart along the x-axis, the behaviour of the two interacting MNPs in the 3 particle model is identical to the 2 particle model.
   In Figure 6.12b, when the starting distance between 1st and 3rd MNP is $100R$, initially the 3rd MNP does not interact. Due to the interaction between the 1st two MNPs, the 1st MNP moves towards to the 3rd MNP ($d < 100R$), causing the 3rd MNP to interact, which in turn pushes the 1st MNP. As a result of the differential drag, the direction of the interaction forces change and the 1st and 2nd MNP aggregates in time.

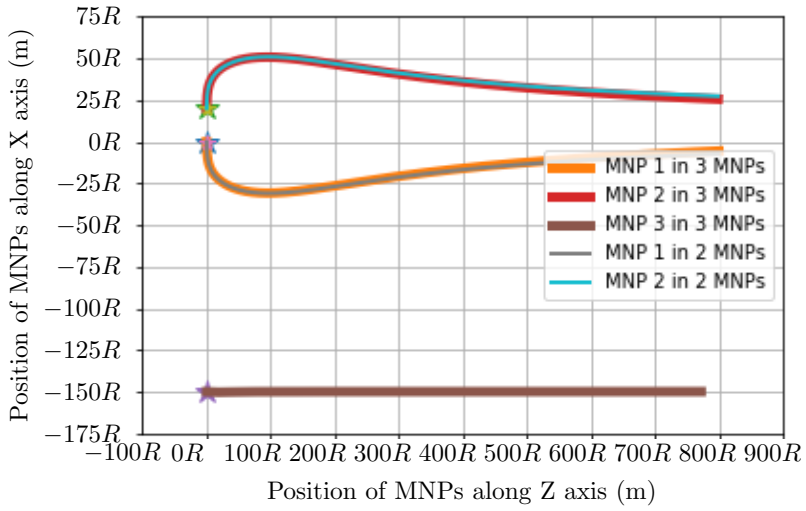

(a)

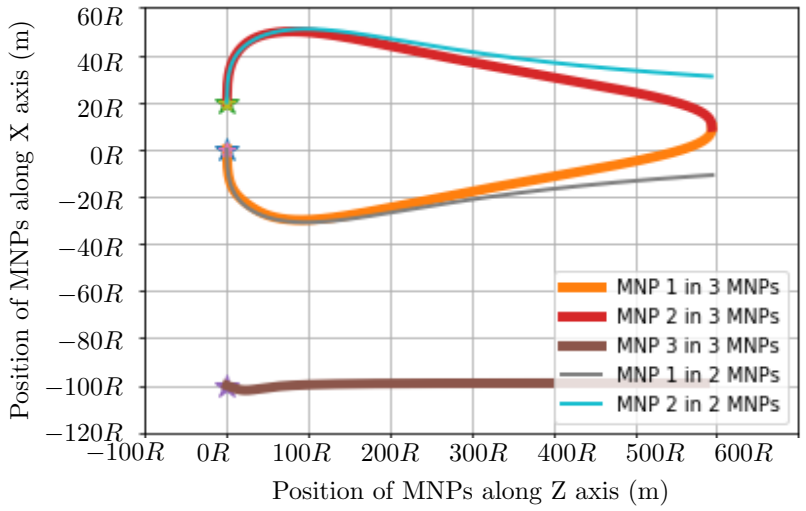

(b)

Figure 6.12: Trajectories of 3 MNPs when 2 MNPs are closer along x-axis than the third.

3. In Figure 6.13, the MNP at origin is equally spaced from the other two MNPs and $r = 20R$. Initially $\mathbf{p}^{(1)} = (0, 0, 0)$, $\mathbf{p}^{(2)} = (20R, 0, 0)$ and $\mathbf{p}^{(3)} = (-20R, 0, 0)$. For the 1st MNP with the maximum velocity, the net interaction force due to the other two MNPs cancels out in the x-axis but adds up in the z-axis. The other two MNPs are initially repelled by the 1st MNP. As 1st MNP moves ahead due to the differential drag, the other two MNPs experience equal attractive force from the 1st MNP and as a consequence all three MNPs aggregate in time.

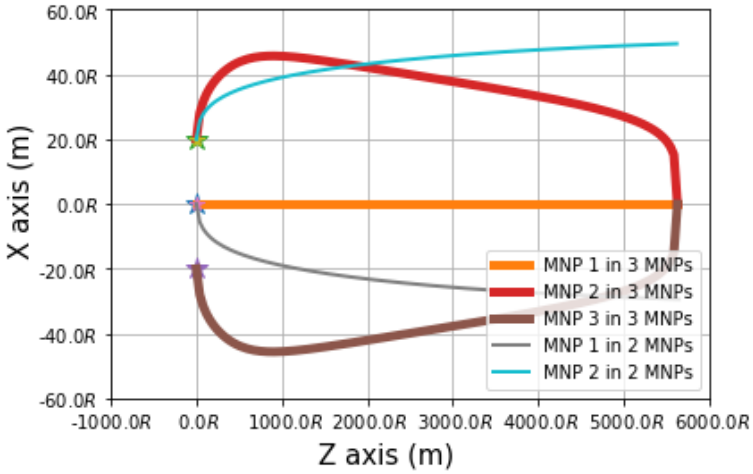

Figure 6.13: Trajectories of 3 MNPs when $r = 20R$.

4. In Figure 6.14, the MNP located at $20R$ along the x-axis is equally spaced from the other two MNPs and $r = 20R$. The MNPs are initially positioned in the top half of the vessel. Initially $\mathbf{p}^{(1)} = (20R, 0, 0)$, $\mathbf{p}^{(2)} = (40R, 0, 0)$ and $\mathbf{p}^{(3)} = (0, 0, 0)$. Initially all the three MNPs repel. As a result of the differential drag, the interaction angle between the MNPs changes. The third MNP initially experiences the highest fluid velocity, moves ahead faster than the other two MNPs, while the other two MNPs aggregate.

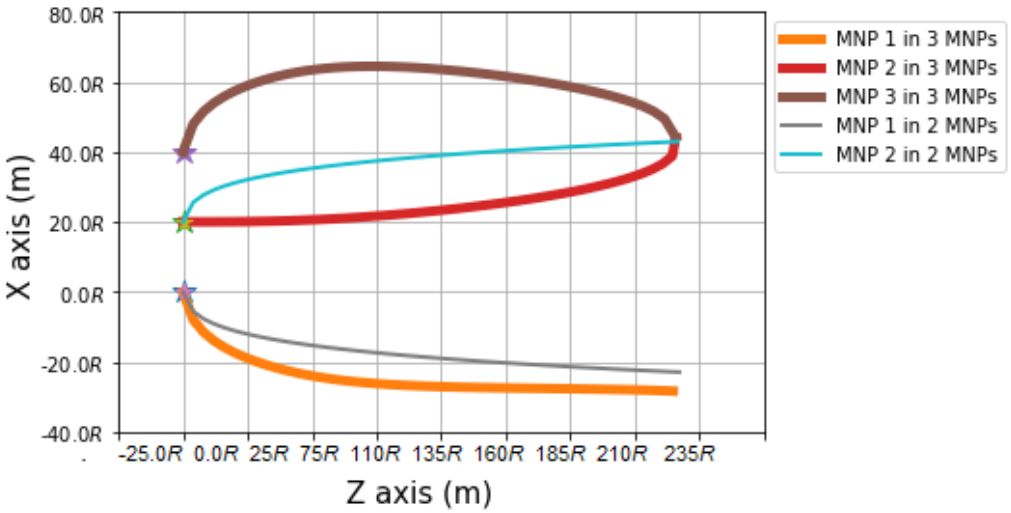

Figure 6.14: Trajectories of 3 MNPs, when positioned in the top half of the vessel.

6.10.1.2 9 MNPs

As the number of MNPs increases, the number of collisions per particle increase and thus the probability of aggregation increases. As described in section 6.7, once any two or more MNPs aggregate, the model pauses and treats the aggregation as a sphere with radius equivalent to the conserved volume of the aggregated MNPs. The model then restarts and calculates the trajectories of the new number of MNPs until a time limit is reached or till all the MNPs aggregate. Figure 6.15a plots the trajectories of MNPs until all the MNPs aggregate. The 'stars' in the Figure 6.15a indicate the positions of the

MNPs before each run of the ode solver. Figure 6.15b plots the ratio between the total number of MNPs after each aggregation instance and the initial number of MNPs. As time increases the ratio decreases, *i.e.* the total number of MNPs decreases. Each aggregation instance can be defined as a separate run of the ode solver. Figure 6.15b shows that by $t = 0.3$ s, all the MNPs aggregate.

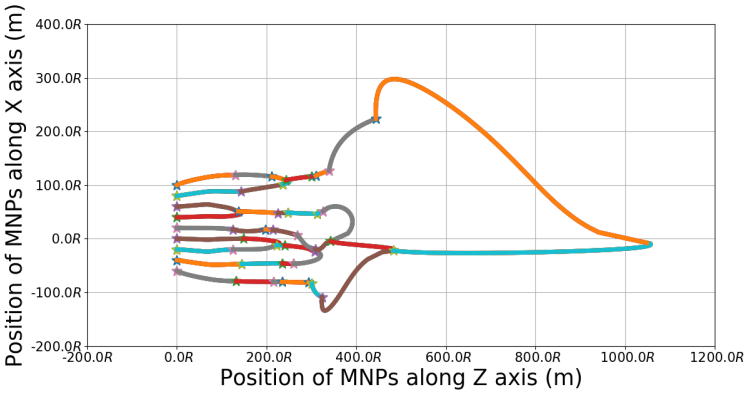

(a)

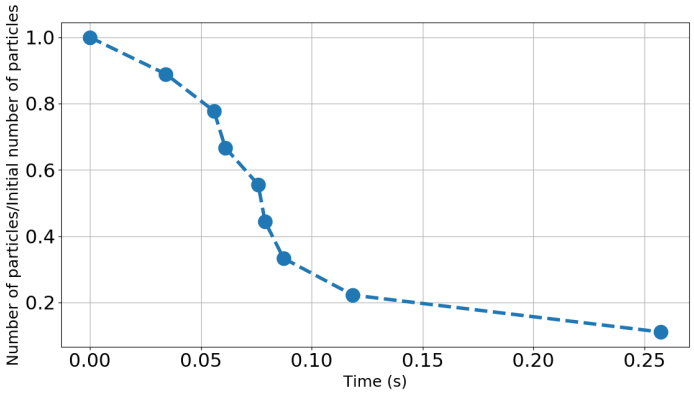

(b)

Figure 6.15: (a): Trajectories of 9 MNPs over time. (b): Aggregation of 9 MNPs w.r.t. time.

6.10.2 Multiple MNPs with random initial positions

6.10.2.1 Initial configuration of multiple MNPs in random distribution

1. Inverse Transform sampling: In this method, random points, (z, x), are generated on a circle. To generate a uniform random distribution of MNPs, along the x-axis of the tube, the generated x values are then used as the initial x locations of the MNPs.

2. Rejection sampling: In this method, random points, (z, x), are generated uniformly on the square of side, s, where $-R_v \leq s \leq R_v$. The points outside the circle of radius R_v are filtered out. The generated x values are then used as the initial x locations of the MNPs.

3. Projection of MNPs: It is assumed that the MNPs are randomly distributed over the cylindrical tube cross-section. It can be projected on a plane as

$$W(x) = R_v \sin\left(\cos^{-1}\frac{x}{R_v}\right) \tag{6.26}$$

where x indicates the random points generated along the x-axis.

Although all the above mentioned types of distribution patterns are investigated, the distribution obtained by projection of MNPs more closely relates to a realistic experiment than the rest. Therefore the following results are generated where the initial distribution of the MNPs is given by equation (6.26). Figure 6.16 plots the trajectory of 30 MNPs, running for a time period of 5 seconds. Keeping all the constants same as in Figure 6.16, Figure 6.17 plots the trajectory of 30 MNPs, running for a time period of 0.1 s, *i.e.* Figure 6.17 depicts a zoomed version of Figure 6.16.

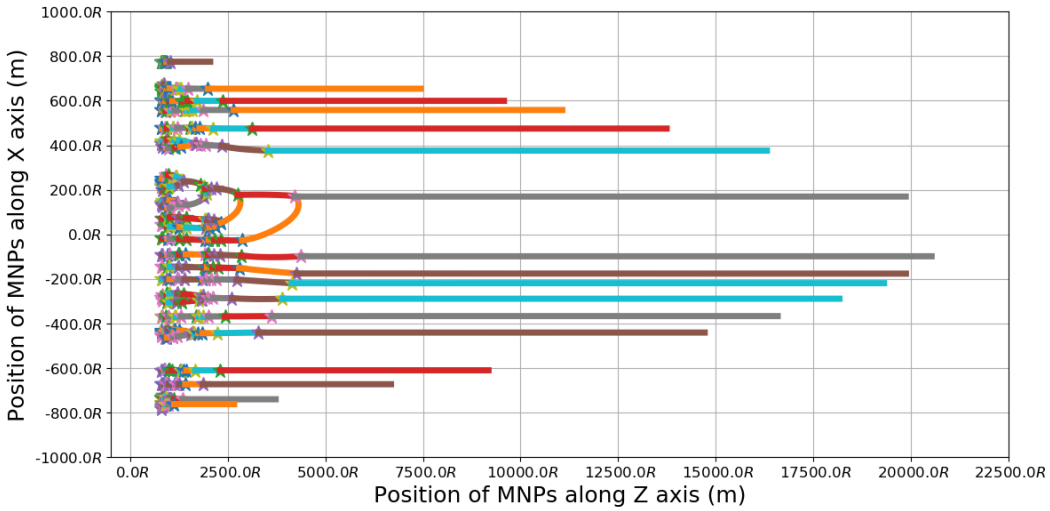

Figure 6.16: Plot of the number of aggregated MNPs when $\overline{v}_f = 10^{-3}\ \mathrm{m\,s^{-1}}$.

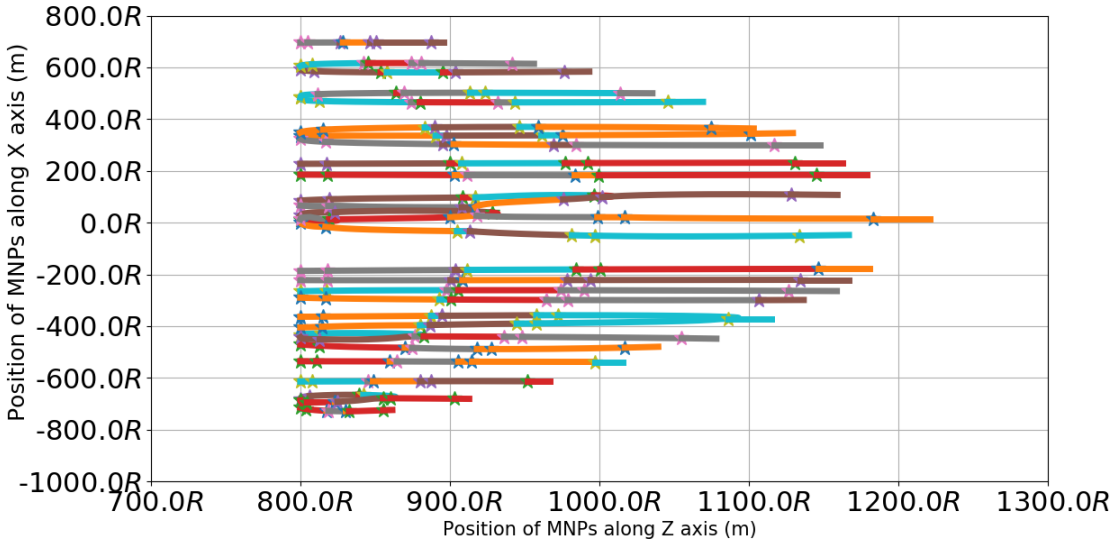

Figure 6.17: Plot of 30 MNPs for a time period of 0.1 s.

6.11 Conclusion

A detailed description of aggregation of MNPs in parabolic flow in the presence of dipolar interaction force and Stokes' drag is presented. The average fluid velocity was found to be an important factor in aggregation. At a specific value of the average fluid velocity, there exists a critical distance along the x-axis within which if the MNPs begin, aggregation occurs over time. Analytic limits of the critical distance are obtained and plotted with the numerical results and an empirical formula (agreement is obtained with 2% error). The empirical formula is proposed by one of my supervisors, Dr PJ Cregg. In the case of multiple MNPs starting with random positions along the x-axis, as the average fluid velocity increases, the aggregation decreases.

Chapter 7

Conclusion

This chapter summarises the work done in each of the chapters presented in the thesis and provides possible scenarios for future work in chapters 2 and 6.

7.1 Chapter 1

Chapter 1 details the general information regarding the the role of MNPs in biomedicine, especially in the applications magnetic hyperthermia, magnetic cell imaging and delivery, magnetic drug targeting and the development of magnetic microrobots. This is followed by a section on the magnetic fundamentals relevant to the work carried out in chapters 2-6 of the thesis.

7.2 Chapter 2

Chapter 2 reviews the existing models of magnetic hyperthermia and the numerical techniques to solve the LLG equation. The computational difficulties in solving the LLG equation in the lower range of frequencies are discussed. In the single particle model, the energy has the low and high frequency asymptotes, $4\mu_0 M_s H$ and $\mu_0 \pi M_s H \frac{\alpha_N}{\omega}$ respectively. An empirical formula for energy has been developed which is based on the form of a first order low pass filter frequency response where choosing a cut-off frequency given by $\omega_c = \frac{\alpha_N \pi}{4}$ aligned the formula well with the data.
This is followed by the development of a mathematical model of magnetic hyperthermia which includes interparticle interactions. It is noted that as the dipole-dipole interactions scale with $\mathbf{r}^3$, the overall behaviour described by the model effectively scales with particle radius. Finally, empirical approximations are presented to determine the optimum heating for a chain of MNPs. For multiple particles, the transverse chain arrangement is found to be the most favourable observed. In practice, this tranverse chain arrangement could be achieved by aligning the MNPs with a static magnetic field prior to the application of the perpendicular alternating magnetic field.
When the alternating magnetic field is perpendicular to the magnetic moment of the MNPs and the MNPs are aligned head to tail, it is observed that interparticle interactions aid the heating, given the interparticle distance, $d_0 \leq \sqrt[3]{\frac{M_s}{H}}$. In all other cases the interparticle interactions hinder the heating mechanism. Therefore, it can be concluded that as a result of dipole-dipole interactions, the M_s/H ratio plays a significant role in the heating of MNPs. Equations (2.30) and (2.32), could be used to predict the coating thickness required for optimum heating in the manufacturing of MNPs in MHT. It is noted that anisotropy is likely to enhance the inhibition of the applied field response. Therefore, the inclusion of anisotropy can be expected to inhibit the MNPs delivering this enhanced heating. The empirical approximates as given in section 2.8, should allow designers to determine the limit on the coating thickness which might still allow enhanced heating.
The maximum additional heating in multiple MNPs almost reaches saturation when $N \geq 8$. This indicates that increasing the number of MNPs does not necessarily increase the generated heating. The available computational power set a limit of $N = 12$ in this simulation. Future work might investigate the effect of further increasing the value of N.

In this work, the MNPs are considered to be spherical. The amount of heating is expected to change if the shapes of the MNPs are altered. Future work might investigate the effect of the shapes of the MNPs on the overall heating.

7.3 Chapter 3

Magnetic Cell Delivery (MCD) is the delivery of healthy cells to diseased targets using MNPs as carriers guided by magnetic fields. Existing theoretical models differ significantly from experimental results, which according to researchers, specifically Riegler *et al.*, is most likely due to neglect of magnetic interactions. Riegler *et al.* have mentioned the importance of magnetic interaction multiple times and attributed their experimental and theoretical discrepancies to the neglect of magnetic interaction in their model. The models of Riegler *et al.* [11, 12] have been referred to by multiple authors, resulting in over 150 citations. Therefore, it was assumed to be a good starting point to build modelling skills in order to model multi-particle interactions as presented in chapter 6.
To model interparticle interactions in parabolic flow later in the thesis, chapter 3 reviewed, replicated and verified two papers and a thesis of Riegler *et al.*, during which different modelling errors were found and corrected. In order to identify the source of errors, a literature review of the derivation of form factors for various shapes is presented. It is found that along with the fluid velocity, the shape of MNPs plays a vital role in determining the targeting efficiency.

7.4 Chapter 4

Sharma *et al.* presented a mathematical model for a cluster of MNPs inside a blood vessel under the influence of an external permanent magnet. Buoyancy was included in their model but it was not explored. The numerical model in Sharma *et al.* has been cited over 55 times. Therefore, in this chapter the numerical model in Sharma *et al.* was implemented and investigated in order to develop modelling skills. Our results show that the effect of buoyancy can be neglected. A number of numerical errors were found and corrected. Several graphs generated show significant deviation from the published results. These are presented for comparison.

7.5 Chapter 5

Magnetic microrobots offer a number of prospective applications in biomedicine. In this chapter, the theoretical formulations of magnetic interactions as given in Mellal *et al.* are reviewed and *ab initio* calculations to predict the behaviour of two microrobots were performed. A number of numerical errors have been found and corrected. Mellal *et al.* presented a model of two interacting MNPs, with experimental results. Therefore, this paper was selected to model in order to learn about magnetic interactions and validate the results. The numerical and typographical errors found in [19] are corrected. Microrobots are a colloidal suspension of MNPs and their shapes appear to be spheroidal from the experimental pictures in Mellal *et al.* (Figure 5.4). In their paper Mellal *et al.* model the particles as spheres. In this chapter their model is extended to account for this spheroidal nature noting the appropriate Stokes correction factors. Figures 5.5a and 5.5b account for the change in distance between the microrobots with Stokes correction factor.

This situation of the microrobots adjusting to a common velocity and moving in a straight line is highly unstable and is unlikely to occur in reality. There is a strong probability that the nature of the magnetic interaction force will push either/both of the microrobots from its trajectory and will eventually lead to aggregation. The diameter of the tube (2 mm) is 4 times bigger than the radius of the largest microrobot (500 μm), which may allow the mircrorobots to have enough space to aggregate. Neither the mathematical model nor the experimental results presented in Mellal *et al.* account for this phenomenon.

7.6 Chapter 6

Chapter 6 presents a mathematical model to study the role of the dipolar interaction force in the aggregation of MNPs in rectangular and parabolic flow. Starting with two MNPs, the model accounts for a uniform random distribution of multiple MNPs along the x-axis of the vessel and predicts the size and nature of aggregation that occurs in different values of fluid velocity. A detailed description of aggregation of MNPs in parabolic flow in the presence of dipolar interaction force and Stokes drag is presented. The average fluid velocity was found to be an important factor in aggregation. Here MNPs are considered whose initial positions are always above or below each other along the vertical axis of the vessel. A critical distance is then found between the MNPs within the vessel. If the MNPs begin their motion within this critical distance, then over time aggregation occurs. This critical distance is found to depend upon the initial position along the diameter of the vessel and also the fluid velocity. Analytic limits of the critical distance are obtained and plotted with the numerical results and an empirical formula (agreement is obtained with 2% error).
In the case of multiple MNPs starting with random positions along the x-axis, as the average fluid velocity increases, the aggregation decreases. Future work might investigate the size of aggregation with respect to the fluid velocity.

Bibliography

[1] Quentin A Pankhurst et al. "Applications of magnetic nanoparticles in biomedicine". In: *Journal of physics D: Applied physics* 36.13 (2003), p. 167. DOI: https://doi.org/10.1088/0022-3727/36/13/201.

[2] B. Mehdaoui et al. "Influence of a transverse static magnetic field on the magnetic hyperthermia properties and high-frequency hysteresis loops of ferromagnetic nanoparticles". In: *Applied Physics Letters* 100.5 (2012), p. 052403. DOI: http://dx.doi.org/10.1063/1.3681361.

[3] J. Carrey, B. Mehdaoui, and M. Respaud. "Simple models for dynamic hysteresis loop calculations of magnetic single-domain nanoparticles: Application to magnetic hyperthermia optimization". In: *Journal of Applied Physics* 109.8 (2011), p. 083921. DOI: http://dx.doi.org/10.1063/1.3551582.

[4] C. Blanco-Andujar et al. "High performance multi-core iron oxide nanoparticles for magnetic hyperthermia: microwave synthesis, and the role of core-to-core interactions". In: *Nanoscale* 7.5 (2015), p. 1768. DOI: 10.1039/c4nr06239f.

[5] Luis C. Branquinho et al. "Effect of magnetic dipolar interactions on nanoparticle heating efficiency: Implications for cancer hyperthermia". In: *Scientific Reports* 3 (2015), p. 2887. DOI: 10.1038/srep02887.

[6] S Ruta, R Chantrell, and O Hovorka. "Unified model of hyperthermia via hysteresis heating in systems of interacting magnetic nanoparticles". In: *Scientific Reports* 5 (2015), p. 9090. DOI: https://doi.org/10.1038/srep09090.

[7] T. Wu et al. "Synergistic Effects of Nanoparticle Heating and Amoxicillin on H. Pylori Inhibition". In: *Journal of Magnetism and Magnetic Materials* (2019), p. 95. DOI: https://doi.org/10.1016/j.jmmm.2019.04.076.

[8] OM Lemine. "Magnetic hyperthermia therapy using hybrid magnetic nanostructures". In: *Hybrid Nanostructures for Cancer Theranostics*. Elsevier, 2019, pp. 125–138. DOI: https://doi.org/10.1016/B978-0-12-813906-6.00007-X.

[9] Xiaoli Liu et al. "Comprehensive understanding of magnetic hyperthermia for improving antitumor therapeutic efficacy". In: *Theranostics* 10.8 (2020), p. 3793. DOI: https://doi.org/10.7150/thno.40805.

[10] Catherine Berry. "Progress in functionalization of magnetic nanoparticles for applications in biomedicine". In: *Journal of Physics D: Applied Physics* 42 (Nov. 2009), p. 224003. DOI: 10.1088/0022-3727/42/22/224003.

[11] J. Riegler et al. "Targeted magnetic delivery and tracking of cells using a magnetic resonance imaging system". In: *Biomaterials* 31.20 (2010), p. 5366. DOI: http://doi.org/10.1016/j.biomaterials.2010.03.032.

[12] J. Riegler et al. "Magnetically assisted delivery of cells using a magnetic resonance imaging system". In: *Journal of Physics D: Applied Physics* 44.5 (2011), p. 055001. DOI: https://doi.org/10.1088/0022-3727/44/5/055001.

[13] J. Gonzalez-Molina et al. “Rapid magnetic cell delivery for large tubular bioengineered constructs”. In: *Journal of The Royal Society Interface* 9.76 (2012), p. 3008. DOI: https://doi.org/10.1098/rsif.2012.0316.

[14] J. Riegler et al. “Magnetic cell delivery for peripheral arterial disease: A theoretical framework”. In: *Medical physics* 38.7 (2011), p. 3932. DOI: https://doi.org/10.1118/1.3593363.

[15] Stavros N Moysidis et al. “Magnetic field-guided cell delivery with nanoparticle-loaded human corneal endothelial cells”. In: *Nanomedicine: Nanotechnology, Biology and Medicine* 11.3 (2015), p. 499. DOI: https://doi.org/10.1016/j.nano.2014.12.002.

[16] J. Riegler et al. “Superparamagnetic iron oxide nanoparticle targeting of MSCs in vascular injury”. In: *Biomaterials* 34.8 (2013), p. 1987. DOI: https://doi.org/10.1016/j.biomaterials.2012.11.040.

[17] Laura Sanz-Ortega et al. “T cells loaded with magnetic nanoparticles are retained in peripheral lymph nodes by the application of a magnetic field”. In: *Journal of nanobiotechnology* 17.1 (2019), pp. 1–20. DOI: https://doi.org/10.1186/s12951-019-0440-z.

[18] Yuanzhao Wu et al. “Magnetic nanoparticle for biomedicine applications”. In: *Journal of Nanotechnology: Nanomedicine & Nanobiotechnology* 2.003 (2015), pp. 1–7. DOI: https://doi.org/10.24966/NTMB-2044/100003.

[19] L. Mellal et al. “Motion control analysis of two magnetic microrobots using the combination of magnetic gradient and oscillatory magnetic field”. In: *Proceedings - International Conference on Manipulation, Automation and Robotics at Small Scales (MARSS)* (July 2017), p. 1. DOI: 10.1109/MARSS.2017.8001917.

[20] Sergio Martínez-Aranda, Francisco J Galindo-Rosales, and Laura Camp-Deaño. “Complex flow dynamics around 3D microbot prototypes”. In: *Soft matter* 12.8 (2016), p. 2334. DOI: https://doi.org/10.1039/C5SM02422F.

[21] C Haase and U. Nowak. “Role of dipole-dipole interactions for hyperthermia heating of magnetic nanoparticle ensembles”. In: *Physical Review B* 85 (4 2012), p. 045435. DOI: 10.1103/PhysRevB.85.045435.

[22] Lucía Gutiérrez et al. “Aggregation effects on the magnetic properties of iron oxide colloids”. In: *Nanotechnology* 30.11 (2019), p. 112001. DOI: https://doi.org/10.1088/1361-6528/aafbff.

[23] Shashi Sharma, VK Katiyar, and Uaday Singh. “Mathematical modelling for trajectories of magnetic nanoparticles in a blood vessel under magnetic field”. In: *Journal of Magnetism and Magnetic Materials* 379 (2015), p. 102. DOI: https://doi.org/10.1016/j.jmmm.2014.12.012.

[24] W. T. Coffey, PJ Cregg, and Yu. P. Kalmykov. “On the Theory of Debye and Néel Relaxation of Single Domain Ferromagnetic Particles”. In: *Advances in Chemical Physics* (1992), p. 263. DOI: https://doi.org/10.1002/9780470141410.ch5.

[25] W T Coffey, Yu P Kalmykov, and J T Waldron. “The Langevin Equation”. In: *World Scientific Series in Contemporary Chemical Physics* 14 (2004), p. 704. DOI: https://doi.org/10.1016/j.crhy.2017.10.001.

[26] PJ Cregg, Kieran Murphy, and Adil Mardinoglu. “Inclusion of interactions in mathematical modelling of implant assisted magnetic drug targeting”. In: *Applied Mathematical Modelling* 36 (2012), p. 1. DOI: https://doi.org/10.1016/j.apm.2011.05.036.

[27] P. F. de Châtel et al. “Magnetic particle hyperthermia: Néel relaxation in magnetic nanoparticles under circularly polarized field”. In: *Journal of Physics.: Condensed Matter* 21 (2009), p. 124202. DOI: doi:10.1088/0953-8984/21/12/124202.

[28] *Wikipedia Vacuum permeability*. https://en.wikipedia.org/wiki/Vacuum_permeability. Accessed: 2019-04-30.

[29] J Frenkel and J Dorfman. “Spontaneous and induced magnetisation in ferromagnetic bodies”. In: *Nature* 126 (1930), p. 274. DOI: https://doi.org/10.1038/126274a0.

[30] CP Bean and J D Livingston. “Superparamagnetism”. In: *Journal of Applied Physics* 30.4 (1959), p. 120. DOI: https://doi.org/10.1063/1.2185850.

[31] Satoshi Ota and Yasushi Takemura. “Characterization of Néel and Brownian relaxations isolated from complex dynamics influenced by dipole interactions in magnetic nanoparticles”. In: *The Journal of Physical Chemistry C* 123.47 (2019), pp. 28859–28866. DOI: https://doi.org/10.1021/acs.jpcc.9b06790.

[32] Ronald E Rosensweig. “Heating magnetic fluid with alternating magnetic field”. In: *Journal of magnetism and magnetic materials* 252 (2002), pp. 370–374. DOI: https://doi.org/10.1016/S0304-8853(02)00706-0.

[33] *Wikipedia Magnetic resonance imaging*. https://en.wikipedia.org/wiki/Magnetic_resonance_imaging. Accessed: 2019-04-30.

[34] Betty YS Kim, James T Rutka, and Warren CW Chan. “New England Journal of Medicine”. In: *New England Journal of Medicine* 363.25 (2010), p. 2434. DOI: 10.1056/NEJMra0912273.

[35] Mahyar Ebrahimi. “On the temperature control in self-controlling hyperthermia therapy”. In: *Journal of Magnetism and Magnetic Materials* 416 (2016), p. 134. DOI: http://dx.doi.org/10.1016/j.jmmm.2016.04.095.

[36] C. L. Dennis et al. “Internal Magnetic Structure of Nanoparticles Dominates Time-Dependent Relaxation Processes in a Magnetic Field”. In: *Advanced Functional Materials* 25.27 (2015), p. 4300. DOI: 10.1002/adfm.201500405.

[37] Alberto López-Ortega et al. “Applications of exchange coupled bi-magnetic hard/soft and soft/hard magnetic core/shell nanoparticles”. In: *Physics Reports* 553 (2015), p. 1. DOI: https://doi.org/10.1016/j.physrep.2014.09.007.

[38] Rudolf Hergt et al. “Magnetic particle hyperthermia: nanoparticle magnetism and materials development for cancer therapy”. In: *Journal of Physics: Condensed Matter* 18.38 (2006), p. 2919. DOI: https://doi.org/10.1088/0953-8984/18/38/S26.

[39] D. Soto-Aquino and C. Rinaldi. “Nonlinear energy dissipation of magnetic nanoparticles in oscillating magnetic fields”. In: *Journal of Magnetism and Magnetic Materials* 393 (2015), p. 46. DOI: http://dx.doi.org/10.1016/j.jmmm.2015.05.009.

[40] M. Osaci and M. Cacciola. “Theoretical studies to elucidate the influence of magnetic dipolar interactions occurring in the magnetic nanoparticle systems, for biomedical applications”. In: *IOP Conference Series: Materials Science and Engineering* 106 (2016), p. 012004. DOI: doi:10.1088/1757-899X/106/1/012004.

[41] Fernando Fabris et al. “Adjusting the Néel relaxation time of Fe3O4/Zn x Co1- x Fe2O4 core/shell nanoparticles for optimal heat generation in magnetic hyperthermia”. In: *Nanotechnology* 32.6 (2020), p. 065703. DOI: https://doi.org/10.1088/1361-6528/abc386.

[42] Alison E Deatsch and Benjamin A Evans. “Heating efficiency in magnetic nanoparticle hyperthermia”. In: *Journal of Magnetism and Magnetic Materials* 354 (2014), pp. 163–172. DOI: https://doi.org/10.1016/j.jmmm.2013.11.006.

[43] Balachandran Jeyadevan. “Present status and prospects of magnetite nanoparticles-based hyperthermia”. In: *Journal of the Ceramic Society of Japan* 118.1378 (2010), pp. 391–401. DOI: https://doi.org/10.2109/jcersj2.118.391.

[44] Rudolf Hergt, Silvio Dutz, and Matthias Zeisberger. “Validity limits of the Néel relaxation model of magnetic nanoparticles for hyperthermia”. In: *Nanotechnology* 21.1 (2009), p. 015706. DOI: https://doi.org/10.1088/0957-4484/21/1/015706.

[45] E. A. Périgo et al. “Fundamentals and advances in magnetic hyperthermia”. In: *Applied Physics Reviews* 2.4 (2015), p. 041302. DOI: http://dx.doi.org/10.1063/1.4935688.

[46] Thomas L Gilbert. “A Lagrangian formulation of the gyromagnetic equation of the magnetization field”. In: *Phys. Rev.* 100 (1955), p. 1243. DOI: https://ci.nii.ac.jp/naid/10013560509.

[47] L’ubomír Baňas. “Numerical Methods for the Landau-Lifshitz-Gilbert Equation”. In: *Numerical Analysis and Its Applications*. Springer Berlin Heidelberg, 2005, p. 158. ISBN: 978-3-540-31852-1. DOI: 10.1007/978-3-540-31852-1_17.

[48] L’ubomír Baňas, Sören Bartels, and Andreas Prohl. “A Convergent Implicit Finite Element Discretization of the Maxwell-Landau-Lifshitz-Gilbert Equation”. In: *SIAM Journal on Numerical Analysis* 46.3 (2008), p. 1399. DOI: 10.1137/070683064.

[49] Ivan Cimrák and Marián Slodička. “An iterative approximation scheme for the Landau-Lifshitz-Gilbert equation”. In: *Journal of Computational and Applied Mathematics* 169.1 (2004), p. 17. DOI: http://dx.doi.org/10.1016/j.cam.2003.10.022.

[50] Massimiliano d’Aquino, Claudio Serpico, and Giovanni Miano. “Geometrical integration of Landau-Lifshitz-Gilbert equation based on the mid-point rule”. In: *Journal of Computational Physics* 209.2 (2005), p. 730. DOI: http://dx.doi.org/10.1016/j.jcp.2005.04.001.

[51] B. Van de Wiele, F. Olyslager, and L. Dupre. “Fast Semianalytical Time Integration Schemes for the Landau-Lifshitz Equation”. In: *IEEE Transactions on Magnetics* 43.6 (2007), p. 2917. DOI: 10.1109/TMAG.2007.892534.

[52] José Luis García-Palacios and Francisco J Lázaro. “Langevin-dynamics study of the dynamical properties of small magnetic particles”. In: *Physical Review B* 58.22 (1998), p. 14937. DOI: https://doi.org/10.1103/PhysRevB.58.14937.

[53] AF AbuBakr and A Yu Zubarev. “Towards a theory of magnetic hyperthermia: effect of immobilized chain-like aggregates”. In: *The European Physical Journal Special Topics* 229.19 (2020), pp. 2991–3007. DOI: https://doi.org/10.1140/epjst/e2020-000054-1.

[54] Emine U Saritas et al. “Magnetic particle imaging (MPI) for NMR and MRI researchers”. In: *Journal of Magnetic Resonance* 229 (2013), pp. 116–126. DOI: https://doi.org/10.1016/j.jmr.2012.11.029.

[55] Byung-Kwan Lim, Elyse C. Tighe, and Seong Deok Kong. "The use of magnetic targeting for drug delivery into cardiac myocytes". In: *Journal of Magnetism and Magnetic Materials* 473 (2019), p. 21. DOI: https://doi.org/10.1016/j.jmmm.2018.09.118.

[56] Dong Luo et al. "Magnetically targetable microcapsules display subtle changes in permeability and drug release in response to a biologically compatible low frequency alternating magnetic field". In: *Materials Science and Engineering: C* 94 (2019), p. 647. DOI: https://doi.org/10.1016/j.msec.2018.10.031.

[57] P.J. Kempen et al. "Theranostic mesoporous silica nanoparticles biodegrade after pro-survival drug delivery and ultrasound/magnetic resonance imaging of stem cells". In: *Theranostics* 5.6 (2015), p. 631. DOI: 10.7150/thno.11389'.

[58] Moataz Dowaidar et al. "Magnetic nanoparticle assisted self-assembly of cell penetrating peptides-oligonucleotides complexes for gene delivery". In: *Scientific reports* 7.1 (2017), p. 9159. DOI: https://doi.org/10.1038/s41598-017-09803-z.

[59] Beata Chertok, Allan E David, and Victor C Yang. "Polyethyleneimine-modified iron oxide nanoparticles for brain tumor drug delivery using magnetic targeting and intra-carotid administration". In: *Biomaterials* 31.24 (2010), p. 6317. DOI: https://doi.org/10.1016/j.biomaterials.2010.04.043.

[60] J. Chomoucka et al. "Magnetic nanoparticles and targeted drug delivering". In: *Pharmacological research* 62.2 (2010), p. 144. DOI: https://doi.org/10.1016/j.phrs.2010.01.014.

[61] G. Wang et al. "Development of multifunctional cobalt ferrite/graphene oxide nanocomposites for magnetic resonance imaging and controlled drug delivery". In: *Chemical Engineering Journal* 289 (2016), p. 150. DOI: https://doi.org/10.1016/j.cej.2015.12.072.

[62] J. Riegler. "Targeted delivery and MRI tracking of magnetically labelled cells". Accessed: 2017-04-12. PhD thesis. University College London.

[63] M Laniado and A Chachuat. "The endorem tolerance profile". In: *Der Radiologe* 35.11 Suppl 2 (1995), S266–70. DOI: 10.1016/0720-048x(91)90049-2.

[64] M Duroux. "Overview of MRI contrast media. The case of endorem". In: *Der Radiologe* 35.11 Suppl 2 (1995), S247–S248. DOI: doi:10.2214/ajr.168.1.8976963.

[65] *Bangs Laboratories: BioMag particles.* https://www.bangslabs.com/products/magnetic-microspheres-particles/biomag-biomag-plus-binding-proteins. Accessed 23 July 2021.

[66] E. Loth. "Drag of non-spherical solid particles of regular and irregular shape". In: *Powder Technology* 182.3 (2008), p. 342. DOI: https://doi.org/10.1016/j.powtec.2007.06.001.

[67] David Leith. "Drag on nonspherical objects". In: *Aerosol science and technology* 6.2 (1987), p. 153. DOI: https://doi.org/10.1080/02786828708959128.

[68] G Kasper, T Niida, and M Yang. "Measurements of viscous drag on cylinders and chains of spheres with aspect ratios between 2 and 50". In: *Journal of aerosol science* 16.6 (1985), p. 535. DOI: https://doi.org/10.1016/0021-8502(85)90006-0.

[69] Z.Y. Zhou et al. "Discrete particle simulation of gas fluidization of ellipsoidal particles". In: *Chemical engineering science* 66.23 (2011), p. 6128. DOI: https://doi.org/10.1016/j.ces.2011.08.041.

[70] Jinrong Chen et al. “Non-spherical particles for targeted drug delivery”. In: *Chemical engineering science* 125 (2015), pp. 20–24. DOI: https://doi.org/10.1016/j.ces.2014.10.022.

[71] PJ Cregg, Kieran Murphy, and Adil Mardinoglu. “Inclusion of magnetic dipole–dipole and hydrodynamic interactions in implant-assisted magnetic drug targeting”. In: *Journal of Magnetism and Magnetic Materials* 321.23 (2009), p. 3893. DOI: https://doi.org/10.1016/j.jmmm.2009.07.056.

[72] Adil Mardinoglu et al. “Theoretical modelling of physiologically stretched vessel in magnetisable stent assisted magnetic drug targeting application”. In: *Journal of Magnetism and Magnetic Materials* 323.3 (2011), p. 324. DOI: https://doi.org/10.1016/j.jmmm.2010.09.028.

[73] PJ Cregg et al. “Many particle magnetic dipole–dipole and hydrodynamic interactions in magnetizable stent assisted magnetic drug targeting”. In: *Journal of Magnetism and Magnetic Materials* 322.15 (2010), p. 2087. DOI: https://doi.org/10.1016/j.jmmm.2010.01.038.

[74] Kar W Yung, Peter B Landecker, and Daniel D Villani. “An analytic solution for the force between two magnetic dipoles”. In: *Physical Separation in Science and Engineering* 9.1 (1998), p. 39. DOI: https://doi.org/10.1155/1998/79537.

[75] S Magdaleno-Adame et al. “Coil systems to generate uniform magnetic field volumes”. In: *Excerpt from the proceedings of the COMSOL conference*. Vol. 13. COSMOL, Inc, Lindsay Paterson. 2010, p. 401.